Capabilities of the Investment Casting Process for producing meso/micro metal castings using Rapid Prototyping manufacturing routes

A thesis

submitted to

Cardiff University

for the degree of

Doctor of Philosophy

by

Jean-François CHARMEUX

Manufacturing Engineering Centre

Cardiff University

United Kingdom

November 2007

ProQuest LLC
789 East Eisenhower Parkway
P.O. Box 1346
Ann Arbor, MI 48106-1346

Summary

This thesis examines the capabilities of different Rapid Prototyping (RP) manufacturing processes for producing sound metallic parts incorporating features in the micrometre range using the Investment Casting (IC) process. RP has been growing in the past twenty years and is nowadays widely employed in the area of precision investment casting since the technology offers the possibility of manufacturing wax patterns which can be directly implemented into investment casting. Owing to the steady improvements of the technology, some of the recently developed RP building machines offer the possibility of manufacturing small parts incorporating micro-features.

In this work, a detailed description of the accuracy and capabilities of the IC process regarding its potential for producing sound meso/micro components is given using two types of conventional RP machines. The results of this analysis are then compared through a benchmarking study with a recently developed RP process suitable for the direct manufacture of ceramic moulds. The different technological chains are compared regarding their overall accuracy, surface finish, the amount of structural defects present in the castings and their relative production costs and lead-time.

Finally, the potential of the investment casting process for manufacturing sound micro-castings with high aspect ratio is approached from a structural point of view. Through a metallographic analysis study, the research investigates the size-scale effect of cast micro-components upon their microstructure and the subsequent changes in their mechanical properties.

Acknowledgements

First of all, I would like to thank my supervisors, Professor D. T. Pham, director of the Manufacturing Engineering Centre and Professor S. Dimov, director of operations for giving me the opportunity to study in the micro manufacturing department and also for their support and guidance both in the technical and written aspects of my research.

I also would like to express deep gratitude to Dr. R. Minev with whom I closely worked throughout my stay at the MEC. His continuous support and wise advice regarding the different aspects of my research taught me a lot and considerably contributed to my progress.

Many thanks to all the MEC staff for their assistance and for providing a friendly working environment.

I am very grateful to my friends, Nolita, Kostas, Elena, Yanis, Samuel, Emmanuel and Katjo for making my stay in Cardiff extremely pleasant. I also would like to thank Miss J. Daw for her precious help and patience regarding the correction of my thesis.

Finally, my deepest gratitude goes to my family who have given me constant support and encouragement.

Table of contents

CHAPTER 3: Technological capabilities of layer based manufacturing processes for producing investment micro-castings

CHAPTER 4: Benchmarking of the Lost Wax Process (LWP) using two RP technologies with the Fcubic-direct shell process for producing micro-castings

CHAPTER 5: Modelling the evolution of the Dendrite Cell Size of cast micro-features as a function of their Thickness and Aspect Ratio using LM25

CHAPTER 6: Conclusions

List of figures

List of Tables

List of Abbreviations

AR: Aspect Ratio

CAD: Computed Assisted Design

CI: Confidence Interval

CIC: Centrifugal Investment Casting

DAS: Dendrite Arm Spacing

DCI: Dendrite Cell interval

DCS: Dendrite Cell Size

DMLF: Direct Metal Laser Fabrication

DSP: Direct Shell Process

EDM: Electro Discharge Machining

EDS: Energy Dispersive X-ray Spectrometry

ES: Edge Straigthness

FCP: Freeze Cast Process

FDM: Fused Deposition Modeling

FIB: Focused Ion Beam

HV: Hardness Vickers

IC: Investment Casting

IT: Information Technology

LD: Linear Dimension

LWP: Lost Wax Process

MEMS: Micro Electro Mechanical Systems

MHV: Micro Hardness Vickers

PM: PatterMaster

QV: Quick Vision

RAD: Relative Angular Deviation

RFP: Rapid Freeze Prototyping

RM: Rapid Manufacturing

RP: Rapid Prototyping

RT: Rapid Tooling

SEM: Scanning Electron Microscope

SD: Standard Deviation

SDAS: Secondary Dendrite Arm Spacing

SLA: Stereolithography

SLM: Selective Laser Melting

SLS: Selective Laser Sintering

Sv: Surface to volume ratio

ThJ: ThermoJet

T_M: Mould pouring temperature

UTS: Ultimate Tensile Strength

VIC: Vacuum Investment Casting

YS: Yield Strength

3D: Three Dimensional

μ-EDM: Micro Electro Discharge Machining

μ-MIM: Micro Metal Injection Moulding

CHAPTER 1: Introduction

1.1. Background and motivation

The transition from the 20th to the 21st century is characterised by a revolutionary change in the way of life of mankind in terms of health care, communication and transportation. This transition started with the appearance of "modern" computers in the mid-20th century which transformed our approach towards engineering and consequently technology itself. Modern engineering relies entirely on our ability to predict and control our manufacturing processes via computers. Although engineering challenges have remained unchanged for centuries, that is, building faster, better, safer and within always tighter tolerances, one can distinguish two major trends in the current manufacturing world: building bigger and building smaller.

These apparently opposite trends are nonetheless interlinked since it is our ability of simultaneously controlling a multitude of different parameters using micro-devices (micro-sensors, micro-actuators) integrated into a bigger system which allows us to build and control efficiently megastructures evolving in continuously more challenging environments (high pressure, corrosion, radiations, extreme temperatures...). The need for micro-products has resulted in the incredibly fast growth of the market for micro-technologies in a very broad range of industries (information and telecommunications, transport, instrumentation, medical...). Therefore, there is an increasing demand to extend the range of available materials for the manufacture of small components incorporating features in the sub-millimetre dimensional range.

Micro-casting combining RP models and IC is a technology which could have good potential for answering some of the current industrial needs. This hypothesis arises from the fact that the use of sacrificial join-less moulds together with the high versatility and increasing accuracy of today's RP machines, offer the possibility of producing small three dimensional parts with complex shapes of a few hundred micrometres thick and high aspect ratios (AR) which could simply not be produced using other manufacturing routes.

However, when considering casting of small parts incorporating meso/micro features, there is a knowledge gap regarding the process limitations due to the size-scale effect of the manufactured part. From a general stand-point, these limitations involve the complete filling of micro-cavities with high AR, casting accuracy and consistency, surface finish and castings' mechanical properties. The reader should remember that from an engineering point of view, assessing the quality of a casting does not only refer to its overall geometrical accuracy but should also consider the degree of its internal soundness, better soundness and consequently higher mechanical properties being obtained in defect-free castings exhibiting an homogenous microstructure.

It is well known that the solidification conditions of a casting are primarily function of its geometry, mould material thermo-physical properties and processing parameters. Since the quantity of defects and the size of the as-cast microstructure are mostly determined by the solidification conditions occurring during casting, the drastic increase in terms of surface to volume ratio of cast micro-features with high AR compared to that of conventional casting size could have a profound effect on the solidification conditions of such features and need to be studied.

Therefore, the aim of this research is to address those issues by assessing the potential of IC for producing accurate and sound meso/micro metal castings in regard to the process/materials interaction and the capabilities of the RP technology considered.

1.2. Objectives

The main purpose of this research consists in investigating the capabilities of the micro-casting process using RP manufacturing routes for producing meso/micro components incorporating functional features with a high aspect ratio in the micrometre range. The objectives of this research are:

- To assess and compare the micro-replication capabilities of commercially available RP machines producing wax models implemented in investment casting in terms of geometrical accuracy using conventional casting alloys;
- To investigate what is the maximum AR which can be consistently produced with a wall thickness of 250μm using gravity casting apparatus;
- To perform a benchmarking study between the results obtained with the conventional RP machines producing wax models and those obtained using RP technology being currently developed and suitable for the direct manufacture of ceramic shells;
- To analyse and compare with conventional size castings the size-scale effect of cast micro-features on their resulting microstructure as a function of the features' thickness, AR and processing parameters for an aluminium casting alloy;
- To analyse the relationship between the microstructure of cast micro-features with high aspect ratio and the corresponding changes in their mechanical properties.

1.3. Outline of the thesis

Although the experimental setting and evaluation procedure were kept identical between the three investigated technologies, the author decided to treat them in two different chapters, namely Chapters 3 and 4, distinguishing commercially available technologies from the one still being in early development stages.

Chapter 2, "Literature background", presents the knowledge background in the field of IC and RP and discusses quality issues when using RP manufacturing routes for producing metal castings. It also introduces the recent research done in the field of micro-casting and places it among other research areas suitable for the manufacture of micro-metallic parts. Finally, it describes the different aspects of the relationship between solidification conditions and resulting microstructure of the family of Al-Si-Mg casting alloys.

Chapter 3 "Technological capabilities of layer-based manufacturing processes for producing investment micro-castings" focuses on assessing the IC process' limitations in terms of overall accuracy, consistency and maximum AR achievable when using sacrificial patterns incorporating micro-features produced using two types of well established and commercially available RP thermal phase ink-jet machines. This study is carried out using different test parts and three casting alloys, Aluminium, Zinc and Stainless Steel.

Chapter 4 "Benchmarking of the Lost Wax Process (LWP) using two RP technologies with the Fcubic direct shell process for producing micro-castings". This study compares the soundness, overall accuracy, surface finish and the relative production costs and labour of castings produced via these three manufacturing routes using the same experimental design introduced in Chapter 3. It also includes a metallography analysis aiming at comparing the amount of porosity present in the vicinity of the mould/metal interface and in the core of the castings produced using the LWP and the Fcubic direct shell process.

Chapter 5 "Modelling the evolution of the Dendrite Cell Size (DCS) of cast micro-features as a function of their AR and processing parameters using LM25", is the final chapter of this thesis. It highlights the important changes in solidification conditions between conventional casting size and cast micro-features. Through a metallography analysis, it describes the structural refinements occurring on cast micro-features and proposes a model describing this behaviour as a function of their AR and processing parameters for an Al-Si-Mg casting alloy. Additionally, it proposes a relationship between the structural refinements described by our model and the changes in the mechanical properties of our micro-castings.

Chapter 6 "Conclusions", summarises the conclusions reached in this thesis and shows the main lines for further research.

CHAPTER 2: Literature background

This chapter presents the knowledge background in the field of IC and RP. It provides the reader with the foundations required for a good understanding of the work presented in this thesis. This chapter deals with the following:

- Offering generalities on the combination of RP and IC;
- Presenting different ways of combining RP and IC;
- Discussing quality issues when using RP manufacturing routes for producing metal castings;
- Presenting the current industrial needs in the field of micro-manufacturing;
- Presenting the work done so far on micro-casting and comparing it with other manufacturing techniques suitable for the production of metallic micro-components;
- Summarising the relationship between solidification conditions, microstructure and resulting mechanical properties of the family of Al-Si-Mg casting alloys.

2.1. Generalities on investment casting

2.1.1. Origin and definition

IC, also known as the Lost Wax Process (LWP), is a manufacturing process which has been traced back to 5000BC, making it one of the most ancient metal forming techniques (Taylor 1983). In this multi-step process (Groover 2005), sacrificial patterns are converted into metallic parts using a join-less mould made out of liquid refractory slurries. The process allows the manufacture of high quality near-net-shape metallic components with the key benefits of accuracy, repeatability and integrity (Beeley 1972).

The manufacture of the mould can be done either by alternate dip coating of a sacrificial pattern into refractory slurry or by casting the slurry into a flask containing the pattern, leading to the production of a shell and block moulds respectively (Dickens et al. 1995) (Figure 2.1). The process is also extremely versatile since castings of virtually any shape, incorporating fine and intricate features, can be produced in almost any kind of alloy (Twarog 1993; Beeley 1972).

2.1.2. Manufacturing routes for investment casting

The classification of the manufacturing methods used for the production of sacrificial patterns generally falls in two categories: the direct and indirect approaches.

2.1.2.1. Direct approach

The direct approach uses Rapid Prototyping (RP) systems to manufacture the pattern. RP refers to a group of manufacturing processes capable of creating solid 3D objects (Kruth 1991), which sometimes cannot be produced by other techniques (Hopkinson and Dickens 2003), directly from the CAD data (Hopkinson and Dickens 2001; Pham and Dimov 2001). Depending on the technology used, the fabricated part can then be directly implemented as a sacrificial pattern in the IC process. This approach, also known as Rapid Manufacturing (RM) (Hopkinson and Dickens 2001; Pham and Dimov 2003), is usually considered for the low-volume production (Cheah et al. 2005) of small parts with high geometric complexity (Hopkinson and Dickens 2001; Kochan et al. 1999).

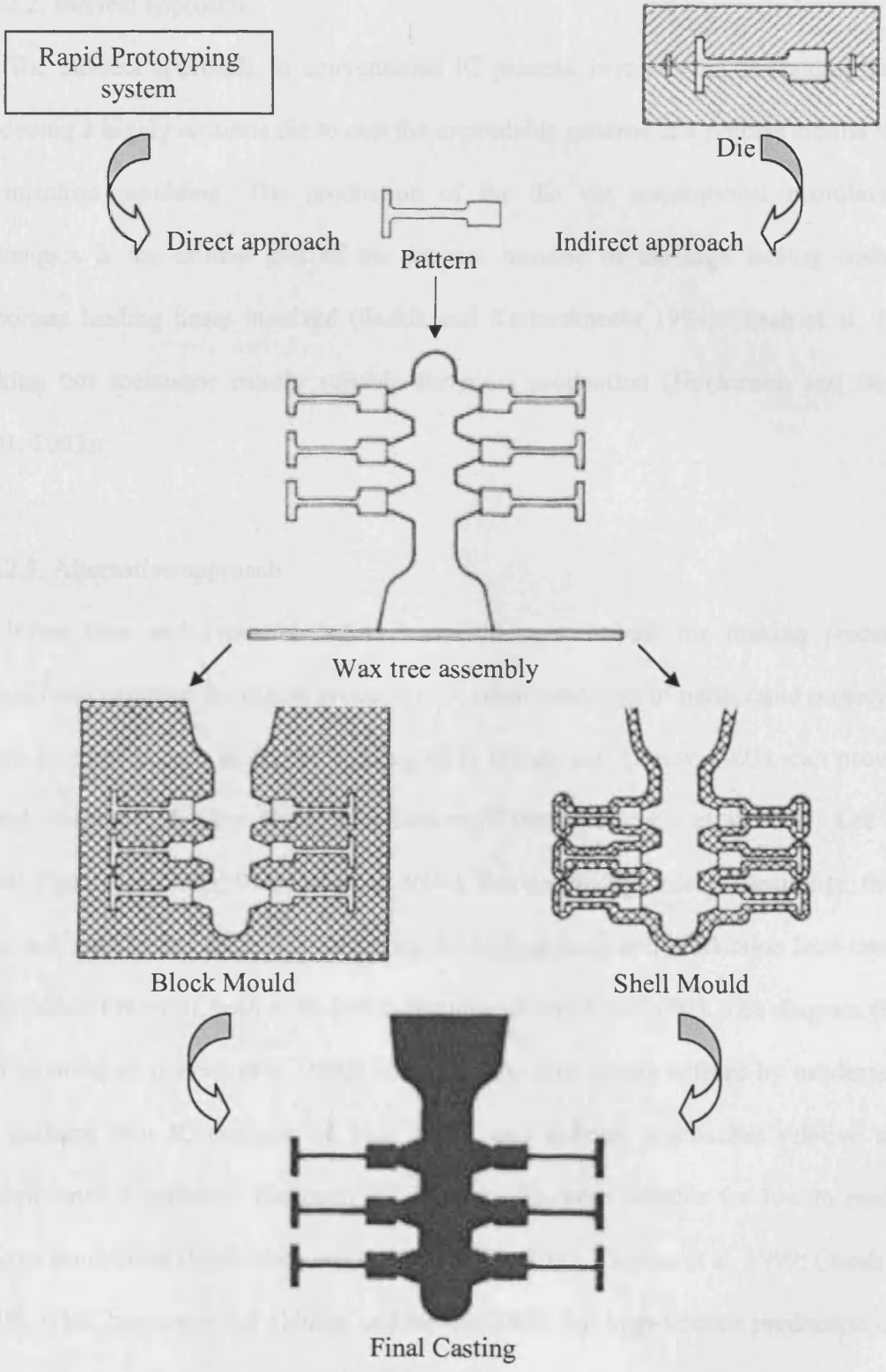

Figure 2.1. The IC casting process seen through both a direct and indirect approach.

2.1.2.2. Indirect approach:

The indirect approach, or conventional IC process, involves the demanding task of producing a highly accurate die to cast the expendable patterns in a process similar to that of injection moulding. The production of the die via conventional manufacturing techniques is the critical part of the process because of the high tooling costs and important leading times involved (Sarkis and Kennerknecht 1994; Cheah et al. 2005), making this technique mostly suitable for mass production (Hopkinson and Dickens 2001, 2003).

2.1.2.3. Alternative approach

When time and financial factors make the conventional die making process an unjustifiable solution for urgent production of small quantities of parts, rapid prototyping-based tooling, known as Rapid Tooling (RT) (Pham and Dimov 2003), can provide a useful alternative for the direct manufacture of dies (Karapatis et al. 1998; Lee et al. 2004; Chua et al. 2005; Rahmati et al. 2007). Besides its high design flexibility, this RT approach has the key benefit of reducing the tooling costs and production lead-times by up to 50% or more (Cheah et al. 2005; Hanumaiah and Ravi 2007). The diagram (figure 2.2) reported by (Cheah et al. 2005) illustrates the time saving offered by implementing RP patterns into IC considering both direct and indirect approaches relative to the conventional IC process. Although RT is generally more suitable for low to medium-volume production (Hopkinson and Dickens 2001, 2003; Kochan et al. 1999; Cheah et al. 2005), it has been reported (Hilton and Jacobs 2000) that high-volume production can in some cases be an economically viable solution.

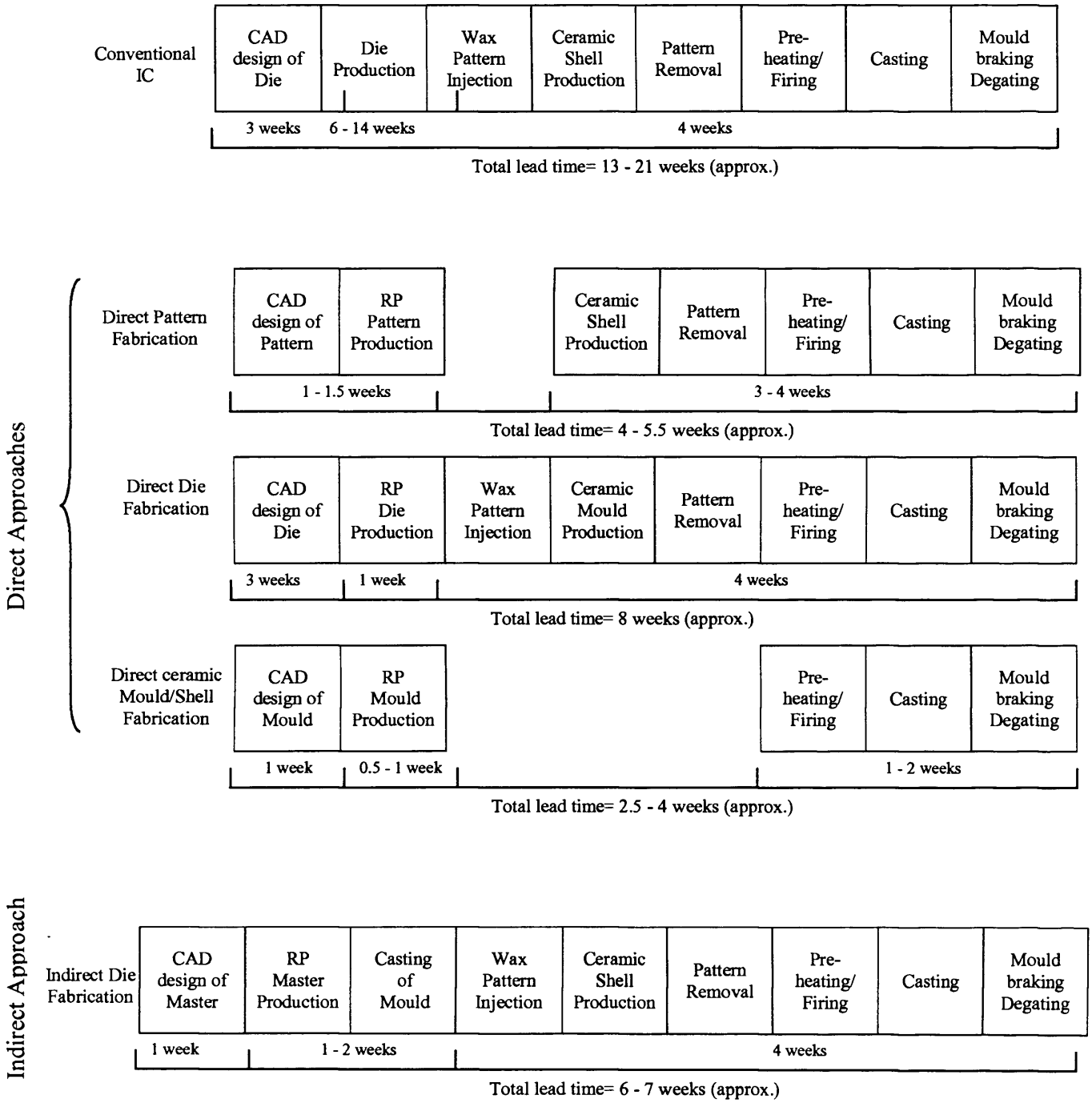

Figure 2.2. Comparison of conventional IC and RP process chains. (Cheah et al. 2005)

2.1.3. Qualities of high grade castings

The particularity of IC compared to the majority of other manufacturing processes is that it is a thermal process involving the solidification of a molten alloy. Therefore, assessing the quality of castings does not only consist of determining their degree of geometrical accuracy but also needs to take into account their overall soundness, surface finish and mechanical properties, the latter being primarily a reflection of alloy chemistry, and solidification conditions (Kaufman and Rooy 2004).

2.2. Rapid prototyping and investment casting

RP systems are considered nowadays as conventional tools in product design and manufacturing (Chua et al. 2003; Pham and Dimov 2003). Among the widespread applications of RP (Pham and Dimov 2003), the introduction of RP parts into the IC process has good potential for the manufacture of functional metallic components.

2.2.1. Sacrificial patterns produced using RP facilities

Since most of the RP systems can produce parts which can be melted or burned-out, researchers extensively studied the feasibility of using them as sacrificial patterns in IC (Childs and Juster 1994; Sarkis and Kennerknecht 1994; Ashley 1995; Dickens et al. 1995; Ippolito et al. 1995; Karapatis et al. 1998; Hague and Dickens 2001; Lee et al. 2004; Zhang et al. 2003; Chua et al. 2005). Their conclusions were that the degree of success varied significantly depending on the technology and material used, wax-like patterns being the most suitable since they could directly be implemented in IC without modifying the process. This might explain why even though numerous RP technologies

are currently available on the market (Kruth 1991; Pham and Gault 1998; Pham and Dimov 2001; Zhang et al. 2003; Cheah et al. 2005), it has been reported by (Mueller 2007) that only four technologies, namely Quickcast™, an SLA build style trademarked by 3d Systems (www.3dsystems.com), SLS (www.3dsystems.com), Thermojet (www.3dsystems.com) and Solidscape Model Maker II (www.solid-scape.com), are responsible for the production of more than 99 percent of sacrificial patterns manufactured by RP facilities each year. More recently developed technologies for producing small patterns with high resolution such as the Perfactory system (www.envisiontec.com) and the ultra-thin layer photopolymer jetting Eden250 from Objet Geometries Ltd (www.2objet.com) are also compatible with the IC process.

More recent developments aiming at improving further the performance of the IC process are currently being developed, such as the Freeze Cast Process (FCP) (Yodice 1991) and Rapid Freeze Prototyping (RFP) process (Liu et al. 2002.a). These technologies producing ice patterns exhibit good potential over conventional RP manufacturing techniques in terms of achievable surface finish, material costs and suppression of problems such as pattern expansion during firing (Liu et al. 2004). However, the manufacture of the shells requires the development of water-free binder solutions and the accuracy of the ice pattern still needs to be improved before matching that of conventional RP technologies (Liu et al. 2004).

2.2.2. Alternative approach: RP for direct shell production

In order to further improve time and cost compressions (Figure 2.2), innovative solutions for the rapid manufacture of moulds to be directly implemented in IC have been

introduced over the last decade. The different approaches can be classified into three RP manufacturing groups, namely; laser fusion, photolithography and 3D printing.

- Laser fusion:

In these processes, the energy laser beam is used to locally fuse the building material. Tang et al. (2003) successfully used SLS technology for the direct sintering of silica sand to build casting moulds.

- Photolithography:

These processes make use of lights (laser beam scanning/UV) to selectively solidify photocurable resins. The company Optoform developed a machine using a paste with a high viscosity and specific rheological behaviour based on the photolithographic technique for manufacturing ceramics parts (Doreau et al. 2000) also suitable for IC (Bernard et al. 2003). In a later paper, Corcione et al. (2006) used a conventional SLA apparatus for producing silica moulds for aluminium casting using both green and sintered moulds.

- Three dimensional printing:

3D printing is a versatile layer additive process suitable for manufacturing ceramic shells and cores to be implemented in IC in a wide range of materials (Sachs et al. 1991). Massachusetts Institute of Technology (MIT) was the pioneer in developing and adapting this direct shelling technology currently commercialized by Soligen (www.soligen.com). According to Soligen, the system is suitable for casting a relatively large range of alloys

such as copper, magnesium, iron, steel, stainless steels and super alloys. Another similar technology called the Zcast Direct Metal Casting process, is commercialized by Z-Corporation (www.zcorp.com). The ZCast powder is a blend of foundry sand, plaster and other additives suitable for casting low temperature metals such as aluminium, zinc and magnesium. Dimitrov et al. (2006) and Bassoli et al. (2007) studied its capabilities and concluded that the technology was suitable for accurately producing complex cavities and cores. However, the two above technologies were developed for producing castings having conventional dimensions and are not known to be suitable for the manufacture of metallic micro-products.

Recently, the Fcubic company (www.fcubic.com) developed high precision ink-jet equipment to manufacture small parts with intricate features out of different materials such as steel, titanium and ceramic parts. Block moulds or shells produced in the later material, i.e. zirconia ceramic, have been shown to offer good potential for producing small castings out of aluminium, zinc and stainless steel (Charmeux et al. 2005,b,c; Charmeux et al. 2006; Charmeux et al. 2007).

2.2.3. Accuracy issues when combining RP and IC

As reported by (Dotchev et al. 2007; Hanumaiah and Ravi 2007), the accuracy of a RP technology is the capital parameter in selecting the appropriate process since the quality of the sacrificial pattern and hence that of the casting is a direct result of the performances exhibited by the RP system. However, as mentioned by Dimitrov et al. (2006), the question of accuracy is generally carefully avoided even in the most relevant case studies, building times and/or cost being the focus of the majority of benchmark

studies undertaken. To the author's knowledge, only a few studies compared and reported in detail the overall quality of IC parts produced out of RP sacrificial patterns. (Dickens et al. 1995) used 6 different RP machines for producing a benchmark test part analyzed and measured before being sent to three different foundries based in Europe, all having different experience in using RP patterns. They concluded that choosing a process in terms of achievable accuracy was delicate since the way the comparison was undertaken played an important role in drawing conclusions. Also, the experience in casting RP models was shown through this investigation, the foundries being the most experienced producing all castings successfully. Another interesting study performed by (Zhang et al. 2003) compared the ability of eight different RP technologies for producing sacrificial patterns to be implemented in IC. Eight parameters characterizing altogether the accuracy of position, accuracy of form and surface finish quality of these different RP technologies were analysed prior to and after casting. They concluded that RP machines producing wax patterns such as the Actua, Thermojet and Sanders offered the best compatibility with the IC process and were the most appropriate technologies for producing small and complex castings. Also, while the Actua and Thermojet technologies exhibited matching performances, the Sander's models showed the best combination of accuracy and repeatability, producing the best surface quality and feature definition among all evaluated RP systems.

Based on these conclusions and since the Thermojet is more widely spread within the industry than the Actua, the author selected the Thermojet and Sanders machines to perform the work carried out in this research. Advanced photolithography processes such as micro-SLA (Thian et al. 2006) suitable for producing small patterns with fine details

were not considered in this work because these technologies were not commercially available at the time of this research and because the implementation of photopolymer models into the traditional IC technology available a the MEC results in poor quality castings due to the presence remaining ashes into the mould after firing.

Comments:

The selection of the benchmark test part in terms of overall dimensions and geometry in all the case studies comparing and investigating the achievable accuracy of different RP manufacturing routes reported in this section was representative of those usually encountered in conventional IC. Therefore, extrapolating their conclusions to small parts incorporating functional features in the micrometre dimensional range would not necessarily hold, due to the size-scale effect of the pattern relative to the manufacturing capabilities of the RP machine. Consequently, more appropriate benchmarking test parts incorporating both macro- and micro-scaled features need to be designed and manufactured through IC in order to investigate and assess the size-scale effect on the final casting accuracy.

2.3. The manufacturing field of metallic micro-products

2.3.1. Micro-product terminology

From a strictly literal point of view, the definition of a micro-product seems to be essentially size-related. Of course a micro-product should be characterized by small dimensions. However, to the author's knowledge, there is no consensus among researchers about where to fix the dimensional boundary between the "macro" and the

"micro" world. This might primarily be due to the fact that the manufacturing capabilities of different processes dictate the lower limit of the dimensional range achievable. In the case of forming processes such as micro-casting, (Alting et al. 2003) stated that the manufacturing challenge started at the sub-millimetre level. Also, as suggested by the same authors, the definition of a micro-product should take into account both the philosophy and the functional characteristics of the product. Therefore, the definition taken under the scope of this thesis will follow the one proposed by (Wechsung et al. 1998):

"Microstructure products have structures in the micron range and have their technical function provided by the shape of the microstructure".

2.3.2. The market for micro-technologies

Over the last 15 years, the field of micro-technology has become a multi-billion market and is still expected to grow (Wechsung et al. 1998; Hesselbach 2004; Mounier 2007), miniaturization and integration of devices being applied in a wide diversity of technological areas such as transport, communication, IT, medical and biomedical, consumer goods, etc. (Alting et al. 2003; Piotter et al. 2004; Wicht and Bouchard 2005; Mounier 2007). However, miniaturization constitutes a real industrial challenge for most of the conventional manufacturing technologies due to the lack of process stability in terms of interaction between process and materials, and the high manufacturing costs generally involved (Alting et al. 2003).

2.3.3. Industrial needs and technologies for producing metallic micro-parts.

Nowadays, numerous technologies have been developed for the manufacture of micro-products (Piotter et al. 1997; Ruprecht et al.1997; Masuzawa 2000; Alting et al. 2003; Hesselbach et al. 2004; Xu et al. 2006). As reported by (Alting et al. 2003; Hesselbach et al. 2004), their development generally follows three different routes:

- Downscaling current technologies from precision engineering;
- Upscaling existing manufacturing processes;
- Developing entirely new processes.

However, while most of the micro-oriented manufacturing technologies developed so far in laboratories exhibit good potential in terms of micro-feature resolution capabilities and accuracy, they generally fail to provide an optimum compromise capable of answering the current main industrial needs such as:

- Need to develop cost-effective production methods suitable for both mass production (Masuzawa 2000; Ehrfeld and Ehrfeld 2001; Alting et al. 2003; Piotter et al. 2004) and small batches of micro-components (Hesselbach et al. 2004).
- Need for manufacturing geometrically complex 3D parts incorporating functional micro-features (Ehrfeld and Ehrfeld 2001).
- Need to extend the range of available materials employed in micro-manufacturing to that of metals (Klocke et al. 1995; Masuzawa 2000; Alting et al. 2003; Pfleging et al. 2003; Piotter et al. 2004;) due to their higher mechanical properties, corrosion

resistance, conductivity and thermal stability (Piotter et al. 2004; Imgrund et al. 2007).

To date, cost-effective micro-manufacturing technologies suitable for mass production are mainly derived from the micro-electronic industry (Alting et al. 2003) and find applications in the field of Micro-Electro-Mechanical Systems (MEMS), e.g. accelerometers and pressure sensors. These highly advanced lithography-based manufacturing techniques, especially LIGA processes, are well suited for producing micrometre and sub-micrometre size metallic structures (Ruprecht et al. 1997; Masuzawa 2000). Their main disadvantages are that they offer a restricted choice of materials and their ability for manufacturing complex shapes is limited (Masuzawa 2000; Jakka and Wilson 2005).

Others, such as micro-injection moulding or hot embossing which are suitable for large-scale production (Piotter et al. 2004), also offer a narrowed range of materials to that of plastics, thus considerably restricting their fields of application.

Owing to the dynamic demand for both geometrically complex and precise metallic micro-components, together with the need to adapt their functionality in constantly more challenging environments, many fields of application strongly require small and micro-metallic parts with features in the range of a few to several hundred micrometres (Alting et al. 2003; Rajurkar et al. 2006; Imgrund et al. 2007; Dimov et al. 2007) (Figure 2.3). As a result, research interests turned in the last decade toward the development of different manufacturing techniques capable of answering these needs (Ruprecht et al. 1997; Masuzawa 2000; Dimov et al. 2007).

2.3.3.1. Mechanical processes based on material removal

- Micro-machining

These emerging technologies have the ability to manufacture 3D shapes out of traditional engineering materials including high strength materials (Ceramics, metals). Owing to the processes' philosophy, there is a physical limit to the minimum feature size achievable due to the materials' elastic deformation (Masuzawa 2000). Micro-machining processes have a lack of mass production capabilities (Kunieda et al. 2005) since they are relatively slow (low rate of material removal), and expensive owing to the high rate of tool wear together with their significant costs. Therefore, these processes are mostly suitable for the production of tools such as electrodes for Electro Discharge Machining (EDM), X-ray masks and moulds for replication techniques (Gandarias 2007).

- Micro Electro Discharge Machining (μ-EDM)

μ-EDM is a thermal process based on material removal by melting and partial evaporation (Masuzawa 2000). It combines high accuracy and smooth surface finish in the sub-micrometer range and allows the manufacture of hard materials such as quenched steel, cemented carbide, and electrically conductive ceramics (Kunieda et al. 2005; Rajurkar et al. 2006). However, the process is slow, thus limiting its applications to the production of micro-tools, electrodes and dies (Masuzawa 2000; Kunieda et al. 2005; Rajurkar et al. 2006).

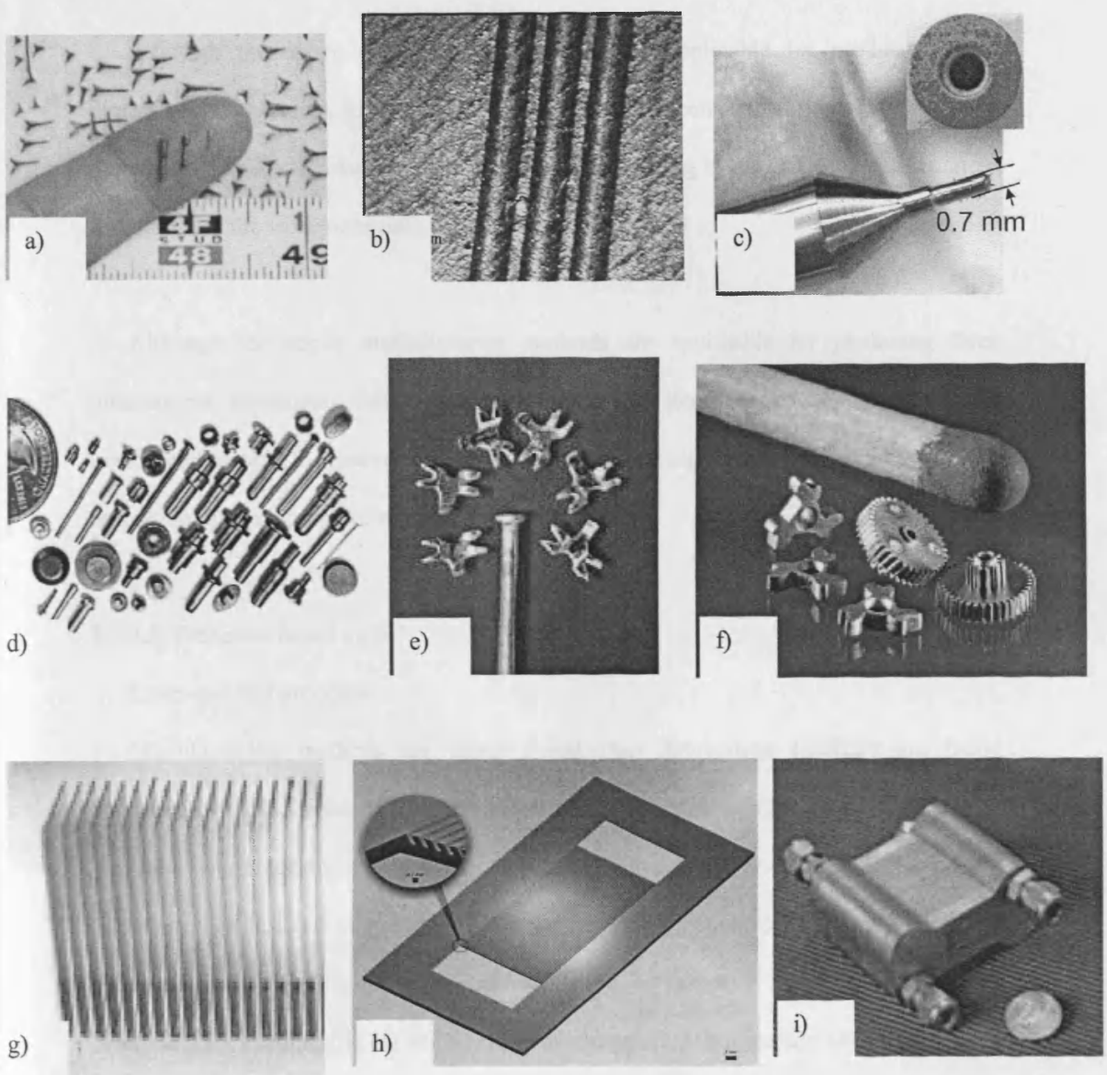

Figure 2.3. Examples of metallic micro-components:
a) Micro-extruded parts (Ehman 2007); b) Hydroforming of micro-channels (Ehman 2007);
c) Micro-punch and die combination (Courtesy of 4M Metals Division); d) Micro-tools and dies for metal forming (Vollertsen et al. 2004); e) Forged mobile handset component (www.precisionmicro.com); f) Micro-parts produced in μ-MIM (www.ifam.fraunhofer.de); g) Extruded aluminium cooling device with 1mm thick fins and AR 20 (www.thermshield.com); h)Micro-channels cooling devices for integrated circuits (http://www.wtb.tue.nl); i) Micro-heat exchanger (www.fzk.de).

Although the above manufacturing methods are applicable for producing three dimensional structures, their philosophy limits the geometrical complexity of the manufactured parts to relatively simple 3D structures owing to the difficulty of accurately repositioning the workpiece onto the machine platform.

Although the above manufacturing methods are applicable for producing three dimensional structures, their philosophy limits the geometrical complexity of the manufactured parts to relatively simple 3D structures owing to the difficulty of accurately repositioning the workpiece onto the machine platform.

2.3.3.2. Processes based on RP

- Laser-assisted processes

Manufacturing methods for direct metal laser fabrication (DMLF) are being extensively studied since they enable the rapid manufacture of functional metallic end-use parts with mechanical properties comparable to that of the raw materials (Lewis and Schlienger 2000; Choi et al. 2001; Khaing et al. 2001; Santos et al. 2006; Ghany and Moustafa 2006). So far, several processes such as selective laser sintering (SLS), selective laser melting (SLM) and 3D laser cladding are commercially available (Ghany and Moustafa 2006). These technologies have the ability to produce very complex 3D shapes in a wide range of materials (Santos et al. 2006; Ghany and Moustafa 2006). Also, it as been reported that they are capable of producing fine detail (Khaing et al. 2001). However, their micro-replication capabilities are still limited because of the difficulty of producing very fine raw metallic materials (Ghany and Moustafa 2006).

- Three dimensional printing

3D printing is an alternative to laser-assisted processes for producing metallic parts. Processes such as the Fcubic direct shell process (www.fcubic.com) introduced in 2.3.2 are capable of producing small and geometrically complex metallic micro-parts out of different materials such as steel and titanium. According to the manufacturer, when considering small parts of a few millimetres high, the speed of the Fcubic process for manufacturing green parts is comparable to that of injection moulding.

2.3.3.3. Processes based on shape replication

As reported by (Masuzawa 2000 and Piotter et al. 2004), these processes are of considerable industrial interest since they combine various technological properties with high economical standards in regard to their suitability for mass production. However they have technical limitations in terms of minimum achievable feature size and sharpness issues due to the limited flowability of the material into the mould or die.

- Micro-forming through plastic deformation

These processes involving plastic deformation can be classified in three sections according to (Vollersten et al. 2004): massive forming, sheet metal forming and profile forming. Besides their suitability for high production rates (Vollersten et al. 2004), they minimize the material loss and produce near-net-shape or even net-shape products with high mechanical properties. Therefore, forging, stamping and extrusion technologies of micro-metallic parts have been increasingly applied in recent years (Zhang et al. 2004). These processes are capable of producing metallic micro-features in the range of tens of

micrometres (Vollersten et al. 2004; Zhang et al. 2004) and find applications in different industrial fields such as the automotive, aerospace, communications, electronics, etc...

- Micro Metal Injection Moulding (μ-MIM)

Similarly to micro-forming processes, μ-MIM is a process allowing the mass production of 3D metallic micro-components in a wide range of materials. As reported by (Liu et al 2002.b), the process allows the production of parts having good mechanical properties and structural details in the order of tens of micrometres. Recent developments with this technology showed that it was suitable for combining non-magnetic and ferromagnetic stainless steel powders, thus widening the process applicability in the field of micro-engineering (Imgrund et al. 2007). This versatile technology finds applications in micro-mechanical systems (gears, impellers, micro-mixers) as well as in the medical field for producing biocompatible micro-bones in titanium. The production of green parts requires the manufacture of a mould, generally by micro-machining or μ-EDM (www.ifam.fraunhofer.de).

The main drawbacks for this technology are that the green parts are fragile and consequently difficult to manipulate and that they undergo a significant linear shrinkage during sintering of approximately 17% depending on the materials used (www.ifam.fraunhofer.de).

- Micro-casting

Micro-casting is a relatively novel manufacturing process which is an adaptation of precision investment casting for components incorporating micro-features (Masuzawa

2000; Baumeister et al. 2002). One of its main advantages is that it allows the fast manufacture of geometrically complex parts from nearly all meltable alloys (Baumeister et al. 2004). Baumeister et al. (2002; 2004a, b) and Rath et al. (2006) demonstrated that when fine investment powders were used, the process was suitable for a direct implementation and accurate replication of sacrificial patterns produced by micro-injection moulding. Since the latter technology is recognized to be suitable for mass production, one might consider micro-casting as a process exhibiting serious potential for the mass production of micro-metallic components. So far, micro-casting has been used for the production of micro-gears, micro-turbine parts and cast metal fibres with a diameter of 100 μm and a maximum aspect ratio (AR) up to 90 using gold and palladium based alloys (Baumeister 2002; Baumeister et al. 2004; Rath et al. 2006) (Figure 2.4). Fabian et al. (2004) reported that investment casting was a good candidate for the manufacture of a miniature gas turbine engine for power generation with a unitary rotor shaft having complex 3D blade features less than 500μm thick.

Baumeister et al (2004) observed a drastic increase in the solidification conditions of cast micro-parts compared to that of conventional castings. This fundamental difference, attributable to the size-scale effect of the castings, considerably refined the microstructure of cast micro-parts and needs to be further studied for a better understanding of the process materials' interactions and their influence on the quality of the as-cast micro-part. Also, Hesselbach et al. (2004) reported that owing to the steady improvement of RP technologies, further research was still required in the field of micro-moulding processes

using RP manufacturing technologies, for the cost-effective production of micro-components.

Recent research in the field of micro-casting led Louisiana Tech University to develop a novel process named NExt AlChemy (Jakka and Wilson 2005). As described by the authors, the process uses a highly exothermic chemical reaction for producing a superheated fluid cast into a reusable micro-machined graphite mould, without a furnace and in a matter of seconds. So far this process has been used for the production of both on- and off-chip cast bronze microstructures with high AR and is presented as promising for casting micro-parts in stainless steel, molybdenum and even uranium.

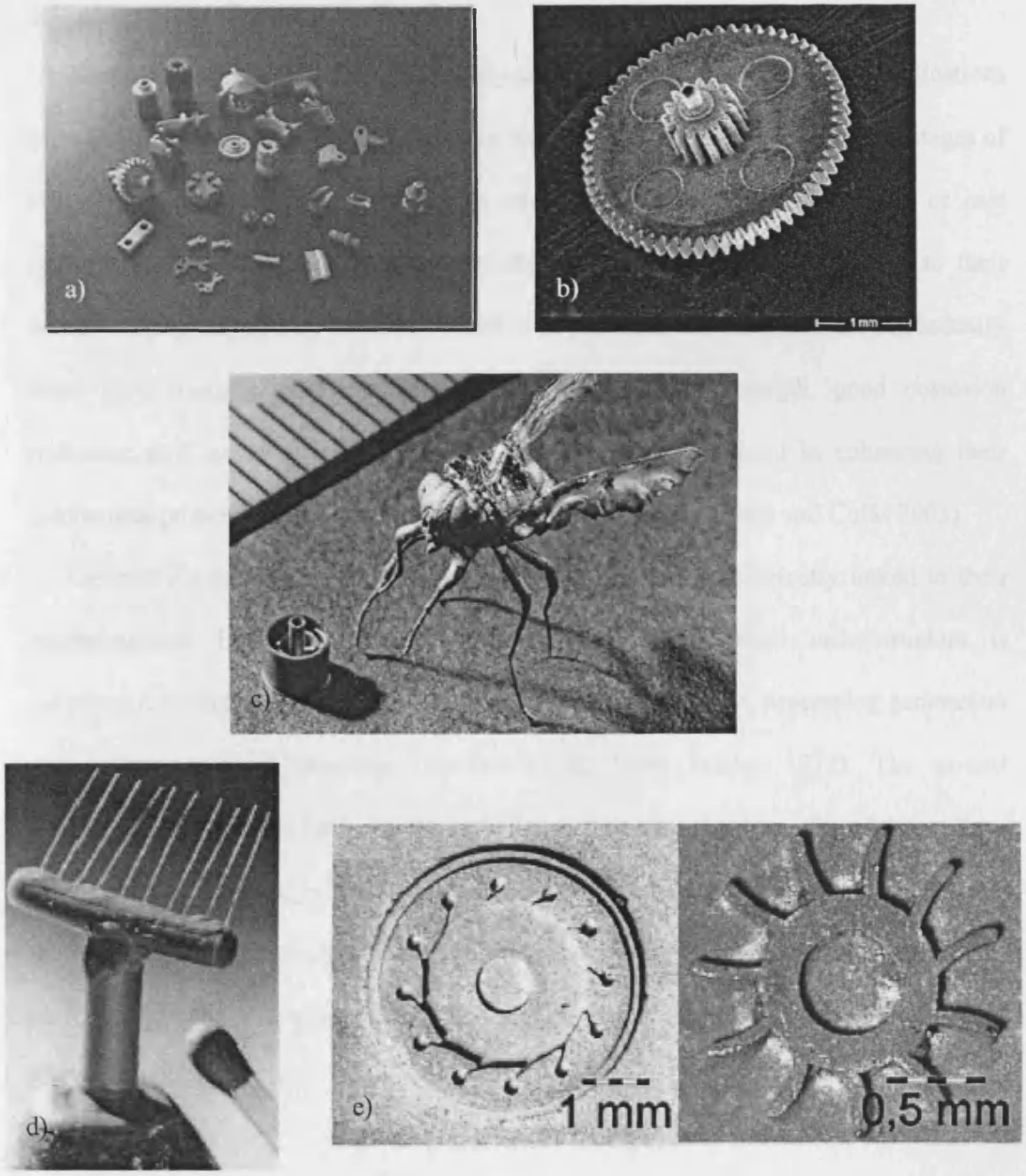

Figure 2.4. Examples of cast meso/micro-parts:
a) meso/micro castings for different type of applications (www.microfond.it); b) Cast micro-gear[1]; c) cast fly in gold based alloy together with a cast micro-turbine[1]; d) cast micro-fibres with high AR[1]; e) Micro-turbine parts[1]. ([1]: www.fzk.de)

2.4. Aluminium alloys and casting

Nowadays, aluminium alloys are widely used in the casting industry with applications in transport, IT, telecommunications, space industry, etc... One of the main advantages of cast aluminium alloys over other alloys such as cast iron, cast carbon steel or cast stainless steel, is that they offer a relatively high tensile strength in relation to their density. The group of cast Al-Si-Mg alloys is of particular interest in the casting industry since they combine excellent castability, high structural strength, good corrosion resistance and are sensitive to heat treatment if one is interested in enhancing their mechanical properties (Flemings 1974; Apelian et al. 1990; Cavazos and Colás 2003).

Generally speaking, the mechanical properties of metals are directly linked to their microstructure. However, when considering cast metals, their microstructure is determined by the alloy chemical composition, casting technique, processing parameters and subsequent heat treatment (Apelian et al. 1990; Beeley 1972). The as-cast microstructure is known for being the main factor governing the properties of these alloys (Beeley 1972). In order to clarify the complex relationship between these variables and their respective influence upon the cast alloy microstructure and consequently the casting performances, the following sections will review part of the extensive research done on Al-Si-Mg casting alloys.

2.4.1. Solidification and microstructure of Al-Si-Mg casting alloys

2.4.1.1. α- and β-phases

Al-Si-Mg alloys are binary types of alloys and crystallise under two distinguished phases: the α-phase and the β-phase. When silicon (Si) is the main alloying element, the

α-phase is a solid solution of Si into Al and the β-phase a solid solution of Al into Si. In the case of hypoeutectic alloys such as LM25, the α-phase solidifies first through the nucleation of small crystals in a proportion relative to the degree of undercooling present in the casting (Beeley 1972). Under favourable thermal conditions (Beeley 1972), these nuclei grow and eventually develop into a dendritic structure, which is the case encountered with most commercial casting alloys forming solid solutions (Beeley 1972; Flemings 1974). The basic principle influencing the growth and coarsening process of dendritic structures during solidification is a surface-driven energy mechanism (Flemings et al. 1991; Mendoza et al. 2003).

2.4.1.2. Eutectic

During dendritic growth, solute is steadily redistributed in the liquid by diffusion at the liquid/solid interface (Beeley 1972; Flemings 1974). In the later stages of the solidification process, the remaining solute-enriched liquid present in interdendritic spaces solidifies to form the eutectic aggregate, a complex simultaneous growth of both α- and β-phases into a fine mechanical dispersion (Brick 1965; Makhlouf and Guthy 2001). Unmodified LM25 eutectic clusters are generally composed of 7-8% of Si particles and intermetallic compounds in volume fraction within the Al matrix (Wang et al. 2001).

The typical eutectic encountered in unmodified alloys solidified under conventional cooling down conditions exhibits a lamellar structure, also called plate-like or flake-like (Steen and Hellawell 1972; Heiberg and Arnberg 2001; Flemings 1974; Makhlouf and Guthy 2001). The same authors reported that this flake-like eutectic morphology shifts to

a fibrous eutectic type when the castings are solidified under rapid freezing rates and steep temperature gradients. Such cooling down conditions are usually encountered with chill or die casting processes of sections thinner than 10mm (Steen and Hellawell 1972).

2.4.1.3. Intermetallic compounds

Intermetallic compounds are structures with different crystallography than that of the material and have the characteristics of distinct chemical species (Brick 1965). The typical intermetallic compounds encountered in Al-Si-Mg alloys are Mg_2Si, the β-phase plates Al_5FeSi and the large π-phase particles Al_8FeMg_3Si. The quantity of Fe-rich phases and the type of phases formed in the castings strongly depend on the Mg content (Wang et al. 1998). During heat treatment certain of these compounds will dissolve and others will not, depending on the level of iron or magnesium. The β- and π-phases are very brittle and considerably lower the mechanical properties of the castings, particularly their ductility (Wang et al. 1998).

2.4.2. Microstructure and Mechanical properties of Al-Si-Mg casting alloys

2.4.2.1. Mechanical properties and dendritic structure

The correlation between the scale of the dendritic structure and the tensile properties of Al-Si-Mg casting alloys has been extensively demonstrated over the years (Spear and Gardner 1963; Oswalt and Misra 1981; Flemings et al. 1991; Cáceres and Wang 1996; Cáceres et al. 2002; Osório et al 2006). It was found that finer dentritic structures led to a significant increase of both the alloy ultimate tensile strength and percentage of elongation. However, the yield strength was not affected by the refinement of the

dendritic structure as reported by (Spear and Gardner 1963). This phenomenon is explained by the fact that local yielding on a microscopic scale is inevitable even at stresses well below the material macroscopic yield stress (Apelian et al. 1990; Wang et al. 2001).

Also as reported by (Oswalt and Misra 1981), finer dendritic structures enhance the material response to thermal treatment. That is, finer microstructure will age-harden to higher tensile properties and higher ductility will also be achieved for a predefined aging time.

2.4.2.2. Mechanical properties' relationship with both Si particles and intermetallic compounds

As demonstrated by (Apelian et al. 1990; Cáceres and Wang 1996; Osório et al 2006), the relationship between microstructure and tensile properties of Al-Si-Mg casting alloys do not only involve the size of their dendritic structure but also the size, distribution and morphology of the Si particles. When Si particles are present as coarse polyhedral and acicular needles (Apelian et al. 1990) such as in the typical Al-Si-Mg eutectic structure, they act as crack initiators (Hafiz and Kobayashi 1994) thus lowering the castings' mechanical properties (Steen and Hellawell 1972). The strain required for crack initiation strongly depends on the aspect ratio and size of both Si particles and intermetallic compounds (Hafiz and Kobayashi 1994; Cáceres and Griffiths 1996; Wang et al. 1998). As demonstrated (Wang et al. 1998), the larger the particles or the more elongated, the higher the probability of cracking. The latter authors also showed that intermetallic

compounds started cracking at low strains (<2%) while eutectic Si particles cracked more massively at larger ones.

2.4.3. Factors influencing the microstructure of cast Al-Si-Mg alloys

2.4.3.1. Alloy chemical composition

The alloy chemical composition primarily dictates the volume fraction of dendrite and eutectic present in the casting (Wang et al. 2001). Also, different alloying elements impact the alloy characteristics both during and after processing. In the Al-Si system, Si enhances the alloy fluidity owing to its high heat of fusion. Alloying elements such as Strontium (Sr) or Sodium (Na) can be added to the melt in small amounts to chemically modify the eutectic's morphology from a flake-like structure to a fibrous one (Apelian et al. 1990; Wang and Cáceres 1998). However, Sr has a negative effect on the amount of porosity and needs therefore to be carefully controlled (Dash and Makhlouf 2001). Other alloying elements such as Mg or Fe influence the material's mechanical properties such as yield strength (YS), ultimate tensile strength (UTS), hardness and elongation (Ravi et al. 1998; Cáceres and Davidson 1999).

2.4.3.2. Processing parameters

Several groups of researchers have studied and reported on the strong correlation between the casting processing parameters and the as-cast metallographic structure of Al-Si-Mg alloys (Spear and Gardner 1963; Berry 1970; Fleming et al. 1991; Ravi et al. 1998; Jie et al 2003; Srinivasan et al. 2006). As demonstrated (Spear and Gardner 1963; Berry 1970; Flemings et al. 1991; Ravi et al. 1998), the solidification rate or cooling rate,

i.e. the rate at which the latent heat of fusion is extracted from the molten alloy and dissipated into the mould, appeared to be the dominant factor influencing the alloy's as-cast microstructure. Their general conclusions were that increasing the solidification rate resulted in a refinement of the alloy's microstructures in terms of Dendrite Cell Size (DCS), size and repartition of the eutectic Si particles, intermetallic compounds and porosity. Also, as reported by (Dash and Makhlouf 2001), the cooling rate plays the biggest role over alloying elements in casting feeding issues.

The solidification rate occurring in a casting is a result of a complex interaction between casting technology, i.e. the process and its materials, and the processing parameters such as mould and molten alloy pouring temperatures (Srinivasan et al. 2006).

Superheat treatment of the melt can also be applied to refine the microstructure (Jie et al. 2003). However, the optimum pouring temperature in terms of as-cast mechanical properties for LM25 was found to be around 720°C, both for metal and sand casting moulds (Ravi et al. 1998; Srinivasan et al. 2006).

2.4.3.3. Heat treatment

Heat treatment of Al-Si-Mg alloys is useful in modifying the mechanical properties of these alloys such as strength, elongation and hardness (Oswalt and Misra 1981; Apelian 1990; Cavazos and Colás 2003). The effects of solution treatment on Al-Si-Mg alloys are:

- Dissolution of equilibrium Mg_2Si particles which appeared during solidification to form a supersaturated solid solution;
- Homogenisation of the casting microstructure;

- Changes of Si particle morphology (reduction of their AR and spheroidization)

The heat treatment process requires the following sequential steps to be performed: solutionization at a temperature close to the eutectic, quenching to retain Mg_2Si in solid solution and aging for a fine precipitation and distribution of Mg_2Si particles (mechanism of precipitation hardening).

2.4.4. Dendritic structure: measurement techniques

In their early paper, (Spear and Gardner 1963) reviewed and defined different possible ways of measuring dendritic refinements:

- Dendrite cell interval (DCI): distance between centre lines of adjacent dendrite cells;
- Dendrite arm spacing (DAS or SDAS): distance between developed secondary arms;
- Dendrite cell size (DCS): width of individual dendritic cells.

These authors mentioned that measuring DCS through individual cell measurements appeared to be the most accurate and satisfying approach for describing dendritic refinement, which was not in agreement with Flemings et al. (1991) who stated that DAS was the preferable method. The latter authors also proposed the surface to volume ratio Sv for assessing dendritic refinement, Sv being obtained by determining the perimeter of a dendrite divided by its enclosed surface area.

The method used in this research for measuring dendritic structures of the castings was that of individual DCS measurements as proposed by (Spear and Gardner 1963).

2.5. Summary

This chapter has reviewed the literature background relevant to the work presented in this thesis. §2.1 provided a brief introduction on the IC process, highlighted the advantages of combining RP and IC, and listed the different requirements that a high-grade casting should meet.

§2.2 showed the versatility of using RP processes for producing either sacrificial patterns or ceramic moulds for IC, together with some studies highlighting the importance of studying and comparing the accuracy of RP parts for producing sound castings.

§2.3 introduced the concept of the micro-product and summarised the current market and industrial needs in terms of production of micro-components. This section also presented the research done so far in the field of micro-casting together with the potential of this technology for answering current industrial needs in comparison with other micro-manufacturing technologies suitable for producing metallic micro-components.

Finally, §2.4 reviewed some of the extensive research studying the complex relationship between process parameters, microstructure and the resulting mechanical properties of the family of Al-Si-Mg casting alloys. This latter section was important for this research since a metallographic analysis investigating the size-scale effect of cast micro-feature upon their microstructure will be performed in the final chapter of this thesis using a conventional Al-Si-Mg casting alloy, widely used in the foundry industry.

CHAPTER 3: Technological capabilities of layer-based manufacturing processes for producing investment micro-castings

By means of different case studies, this chapter describes the technological capabilities of the investment casting process when used for producing meso/micro-scaled castings. The functionality of such castings lies in their combined ability to integrate smaller components as well as to be integrated into a bigger system. Therefore, and since post-processing operations such as machining, grinding and polishing are a delicate and cost-consuming task because of the small size of the component, it is imperative that the accuracy of the as-cast part fulfil the dimensional requirement of the CAD drawing.

3.1. Factors affecting accuracy

Some of the main factors having a considerable influence on the castings' accuracy produced using RP facilities are described below.

3.1.1. STL file parameters

The STL file format, said to be derived from the word "STereoLithography", is commonly used for interfacing CAD and RP systems. It approximates the surface of a 3D model with triangular facets. In every case, the number of triangles representing the model can be defined by the user by changing the chord height and the angle control (Jacobs 1996). However, it is sometimes difficult to avoid facets on curved surfaces since an extremely fine meshing of the CAD model increases the size of the file, consequently making it unmanageable (Figure 3.1). Therefore, a compromise has to be made between the model's resolution and the size of the generated file.

3.1.2. Accuracy of the pattern building machine

The technological capabilities of the manufacturing process chosen for producing the lost pattern also influences the absolute accuracy (flatness, roughness, dimensional accuracy) of the final casting. RP building machines using thermal phase change inkjets (Thermojet, PatternMaster) usually offer a good compromise over other RP manufacturing routes (SLA, SLS, FDM..) when considering models of small dimensions incorporating functional features in the meso/micro dimensional range. However, the model's absolute accuracy is dependent on the discrete nature of the process. The x and y positional accuracy of the system print head and the layer deposition thickness in z affect both the shape and the surface texture of the model. This is often characterized by a stair-step effect on curved surfaces which consequently degrades the part roughness (Figure 3.2). Also, the contraction of the wax during its solidification influences the pattern's geometry. Even though the volumetric shrinkage of the thermoplastic material can accurately be predicted and thus anticipated by the pattern building machine knowing the material's thermophysical properties, the part's geometry also has an impact on the material shrinkage, sometimes leading to undesirable shape distortion of the pattern during cooling.

3.1.3. Materials interactions under thermal constraints

The interaction between the materials involved in the IC process is also a considerable source of inaccuracy since their response to thermal constraints varies significantly (Beeley 1972; Piwonka and Wiest 1998).

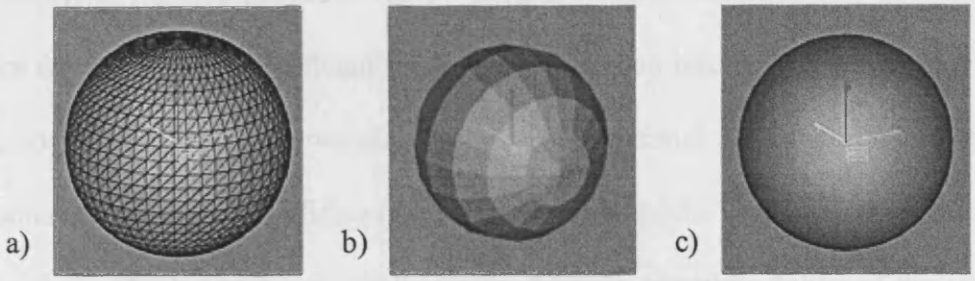

Figure 3.1. STL file: a) Generated file approximated by triangles; b) Faceted model due to coarse meshing tolerance; c) Model with fine meshing tolerance.

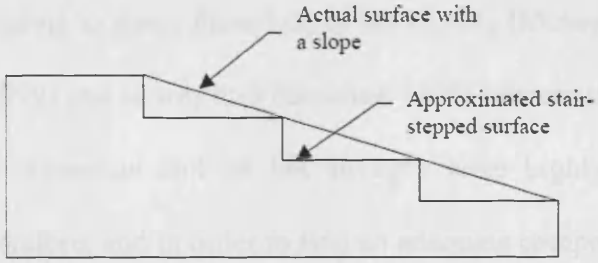

Figure 3.2. Discrete nature of layer-based manufacturing processes.

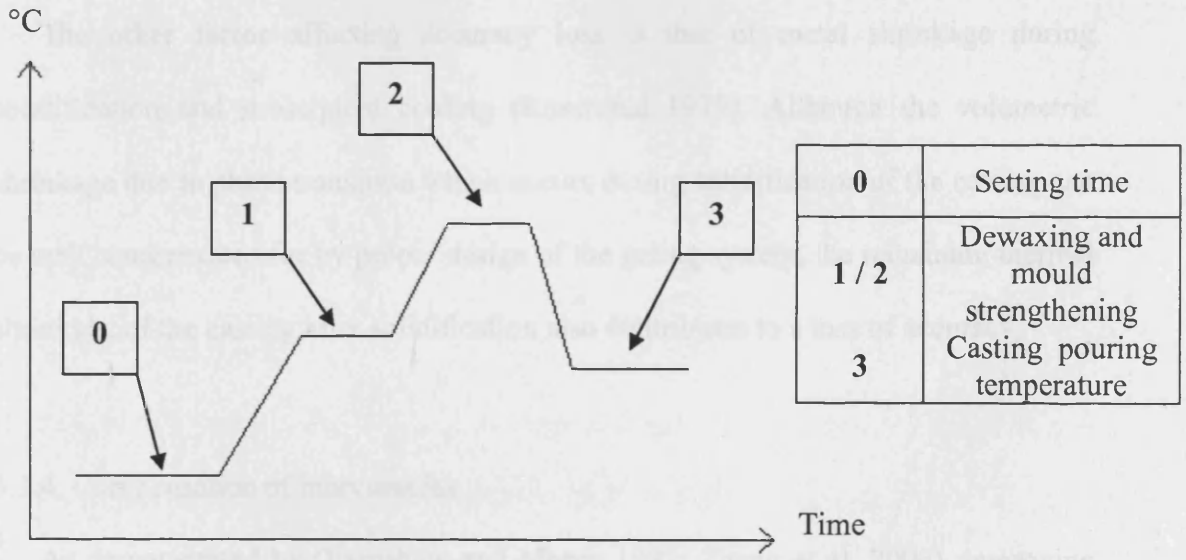

Figure 3.3. Firing cycle of the ceramic mould.

Sacrificial patterns produced out of thermoplastic materials, waxes or resins are known for undergoing significant volume expansion on heating (Diwan et al. 1997). This, together with the investment setting and thermal expansion may lead to investment cracking during firing (Sarkis and Kennerknecht 1994; Yao and Leu 1991; Zhang et al. 2006), which can result in some cases in complete failure of the casting. The investment hot strength is therefore a parameter of considerable interest in preventing the appearance of such phenomenon. However, hot strength can affect casting accuracy by restricting the alloy contraction during cooling (Markley 1953; Rosenthal 1979), thus leading to shape distortion of the casting (Morey and Earnshaw 1995). Low and Mori (1999) and Morey and Earnshaw (1995) demonstrated that both the investment thermal expansion and its hot strength were highly correlated to casting inaccuracies. Therefore, and in order to find an adequate compromise between hot strength and casting accuracy, it is essential to respect the manufacturer's instruction in terms of liquid to powder ratio (L/P), setting expansion time after embedding and thorough firing cycle (Figure 3.3).

The other factor affecting accuracy loss is that of metal shrinkage during solidification and subsequent cooling (Rosenthal 1979). Although the volumetric shrinkage due to phase transition which occurs during solidification of the casting can be well compensated for by proper design of the gating system, the remaining thermal shrinkage of the casting after solidification also contributes to a loss of accuracy.

3.1.4. Compensation of inaccuracies

As demonstrated by (Earnshaw and Morey 1992; Zhang et al. 2006), improving casting accuracy is feasible by using the investments' thermal expansion to offset metal solidification shrinkage. Also, varying the processing parameters such as the

mould pre-heat and metal pouring temperatures can help improve castings' dimensional accuracy, higher temperatures offering a greater compensation for metal solidification contraction (Beeley 1972; Rosenthal 1979). However, because practices for assigning casting allowances are found to vary greatly between investment casters (Okhuysen et al. 1998), the literature is unable to provide any guideline which could be used by designers to optimize the choice of their shrinkage factors relative to the size of the cast features. Therefore, the production of high quality grade castings still relies mainly upon designers' experience-based knowledge (Rosenthal 1979), trial-and-error iterations and through a thorough control of the processing parameters.

Nowadays, the development of mathematical models based on experimentation can help minimize the number of trials required for producing sound castings. Recent studies focusing on predicting the behaviour of materials for IC such as injected waxes (Sabau and Viswanathan 2002, 2003) and aluminium (LM25) casting alloy using shell IC (Sabau 2006), showed that shrinkage factors could be accurately predicted for both restrained and unrestrained dimensions. However, these models are still restricted to a relatively narrow range of materials and casting geometries and need to be further developed in order to extend their field of applicability.

3.2. Experimental settings

3.2.1. RP technologies

The lost patterns were built using two different thermal phase change inkjet systems. The first one, named SPI PatternMaster (PM) from Sanders Prototypes Inc., uses two nozzles, one for the build material, the other for the support material, to build the pattern in a wax-like material. This technology was initially developed for those casting industries working on the production of medium to small size patterns

incorporating intricate features such as jewellery and art design (Chua et al. 2005; www.solid-scape.com). Because it has excellent positional accuracy of the print head and employs a milling cutter surfacing the pattern after the completion of each layer, this RP machine produces patterns exhibiting better accuracy and surface finish over conventional RP machines (FDM, SLS, SLA) (Zhang et al. 2003; Chua et al. 2005) but at the expense of the building time. Additionally, the support material can be easily dissolved using an appropriate solvent, avoiding the need for the operator to deteriorate part accuracy and surface texture by manually removing the support material. The second system named ThermoJet (ThJ) from 3D Systems is more widely used in the RP and investment casting industry. It allows a faster build of bigger patterns than the PM as it features a printing head composed of 352 jets. Contrasting with PM technology, the pattern's supports of the ThJ are produced in the same wax-like material as the part and need to be manually removed before embedding. Technical information on both technologies is available in table 3.1.

3.2.2. Alloys and casting units

Three alloys were used in these experiments. The first two, Aluminium (LM25) and Zinc (ZA12), are widely used non-ferrous alloys in the casting industry as they combine excellent castability and sensitivity to solution heat treatment if one is interested in enhancing their mechanical properties (Apelian et al. 1990). The third one was Stainless Steel (316 S16) and was chosen because of its problematic casting behaviour even using centrifugal casting processes. Their composition is listed in table 3.2. The alloys' pouring temperatures were set at 485°C, 720°C and 1600°C for ZA12, LM25 and 316 S16 respectively. These temperatures are those conventionally

used at the Manufacturing Engineering Centre (MEC) and represent an added superheat of approximately 10-15%, in order to enhance flow length (Beeley 1972).

Two types of casting machines were used to produce the castings. The low temperature vacuum investment casting (VIC) MPA 300 from MCP (www.mcp-group.com), which is an induction melting machine combining inert gas overpressure and a vacuum assistance for casting non-ferrous alloys like Al, Zn and Cu, and the PPC 3200S casting unit from Schultheiss (www.schultheiss-gmbh.de), an induction melting centrifugal casting machine (CIC) combining inert gas overpressure and vacuum assistance to cast high temperature alloys such as Fe, Ni and Ti. The schematic drawings of the casting units are shown in figure 3.4 and their main technical specifications are provided in table 3.3. Argon and Nitrogen were used in our study as the inert gas for centrifugal and vacuum casting units respectively.

3.2.3. Mould materials and pre-heating

Two types of investments, both supplied by Hoben International, were used in our experiment. ZA12 and LM25 alloys were cast using a classical gypsum-bonded investment (M028) while 316 S16 was cast in a phosphate-bonded silica investment (M062) which exhibits a higher thermal resistance at elevated casting temperatures. These investments' compositions are provided in table 3.4. The mixing water to powder ratios (L/Kg) used were those specified by the manufacturer and were 0.29 and 0.33 for M028 and M062 respectively.

The moulds' pre-heating temperatures were set at 250°C and 600°C for the non-ferrous alloys and 316 S16 respectively. These temperatures were empirically chosen since they were the minimum mould temperatures enabling a successful production of sound castings incorporating meso/micro features with high AR.

Technology	Build Size mm	Accuracy	Thermoplastic material	Layer thickness µm
PatternMaster	250*190*228	0.025 mm/mm in X-Y and Z	Wax	13 to 76
ThermoJet	304*152*228	0.025mm/25mm in X-Y and Z	Organic Polymer	40

Table 3.1. Main characteristics of the ThJ and PM building machines.

Alloys	Composition (%wt)
ZA 12	Al 11; Cu 0.78; Fe 0.018; Si 0.12; Mg 0.023
LM 25	Si 7; Cu<0.78; Mg 0.4; Mn 0.3; Fe<0.5; Ni<0.5; Zn<0.1
316 S16	C 0.08; Cr 17; Ni 12; Mn 2.0

Table 3.2. Alloys composition.

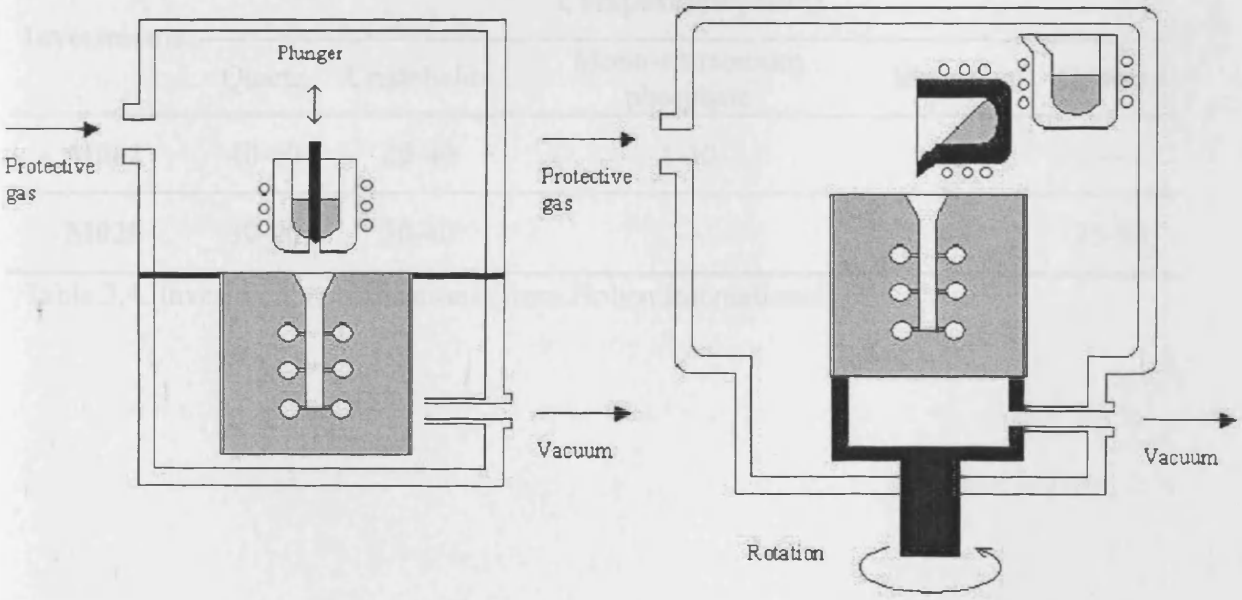

Figure 3.4. Schematic drawings of both investment casting units.

Process	MCP Equipment	Shultheiss
Alloys	Al, Zn, Cu	Fe, Ni, Cr, Ti
Max Flask Size	diam350 x 500 mm	diam120 x 160 mm
Min Flask Size	diam125 x 250 mm	
Max. Melt. Temp.	1300°C	2200°C
Crucible Capacity	3 liters	100 cm^3, 750g Fe-alloy
Induction heater power	25 kW	20 kW
Vacuum	-1000 mbar	-1000 bar
Overpressure	1500 mbar	2000 mbar

Table 3.3. Specifications of the casting units.

Investments	Composition (%wt)				
	Quartz	Cristobalite	Mono-ammonium phosphate	Magnesia	Gypsum
M062	40-60	20-40	5-10	4-8	---
M028	30-40	30-40	---	---	25-35

Table 3.4. Investment specifications (from Hoben International)

3.2.4. Geometrical analysis

The geometrical accuracy analysis was performed on a specially designed test part named "Pyramid" (Figure 3.6) using an optical measurement machine Mitutoyo Quick Vision Accel (QV) (www.mitutoyo.co.uk). Each test part was analysed before and after casting so that the variation due to the multi-step process of the VIC could be highlighted. The choice of a contact-free measurement system was more appropriate than the commonly-used touch probe technique because of the small sample size and the brittleness of the thermoplastic material (Dickens et al. 1995; Chua et al. 2005) used by the RP building machines. Since twenty test parts were measured by a single operator for this analysis, our experimental settings did not match those required to apply the conventional and well-established Gage R&R procedure used in the casting industry to assess the measurement variability of the pattern shop (Peters et al. 1996 b). However, a measurement error test was performed on the QV system to estimate whether its precision error was of acceptable magnitude relative to the size of the feature measured. A randomly selected metallic test part was measured 10 times at 3 different locations which required the use of one of the 3 magnifications available on the QV system (x1, x2 and x6). For each set of measures, the system was re-initialized and the part repositioned on it. The measurement error at each magnification was obtained using the following formulae (Peters et al. 1996 b):

$$Measurement \cdot Error = \frac{Measurement \cdot Variability}{Pattern \cdot Tolerance} * 100 \qquad (3.1)$$

The measurement variability in (3.1) was characterized by the standard deviation (SD) relative to the size of the feature measured. It was calculated for the series of 10 repetitions performed at each magnification. Since no pattern tolerance was specified in our study, the pattern tolerance was arbitrarily set as 5% of the average step dimension measured for each magnification. The results showed that the QV system

had a measurement error of less than 10% regardless of the magnification used, justifying its suitability for our dimensional analysis investigation (Peters et al. 1996 a). Details of the QV system measurement error analysis are provided in appendix 3.1.

3.3. Case study

Three different designs were used to perform the study. The first test part, called "Logo", with an overall size of 19x16x3 mm (Figure 3.5), included intricate and small features with dimensions down to 250 μm and aspect ratio up to 2.4. These test parts produced using the ThJ technology were used to assess and compare the overall quality of castings produced using different alloys. The features analyzed in these test parts were the characters "M" and "ing" magnified as shown in figure 3.5. The test part "Pyramid" (Figure 3.6) was a structure of 10 steps with dimensions from 11.5x11.5 mm to 300x300 μm at the top that represented a reduction by a factor of 1.5 at each step. This unconstrained geometry allowed the metallic parts to shrink freely into the mould. The Pyramids were used to compare and assess the potential changes in the geometrical accuracy of both RP machines by progressively downscaling the observed features to the sub-millimetre range. Twenty Pyramids were produced for this investigation, ten using each manufacturing technology, ThJ and PM respectively. After arbitrarily numbering the twenty Pyramids, each set of ten was divided into two groups of five Pyramids so that they could be cast using both LM25 and ZA12 alloys. Therefore, a total of four sample groups each containing five theoretically identical Pyramids were produced.

The last test part, called "Rib", incorporated six ribs of 250 μm thick and several ranges of AR: 10-20; 20-30; 30-40; 40-50 and 50-60 with an AR increase between ribs of a step of 2. Figure 3.7 shows an example of a cross-sectioned CAD file of a

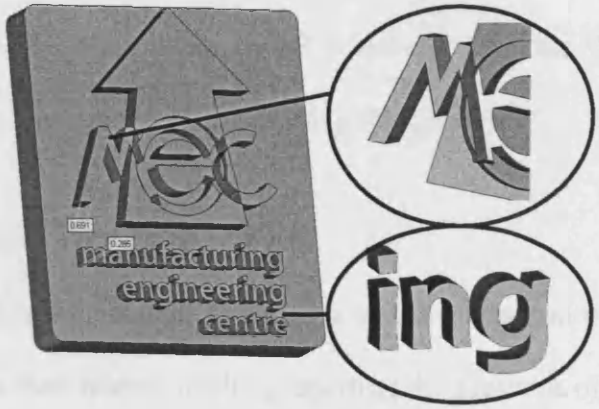

Figure 3.5. Logo test part and its observed characters "M" and "ing".

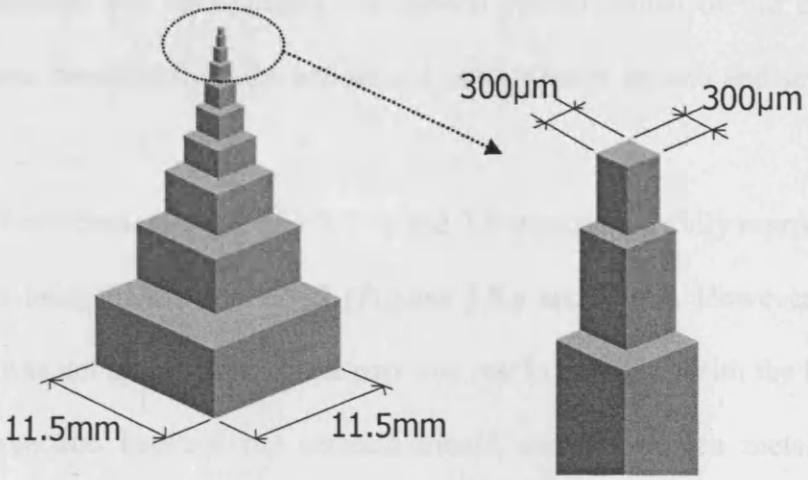

Figure 3.6. Pyramid test part.

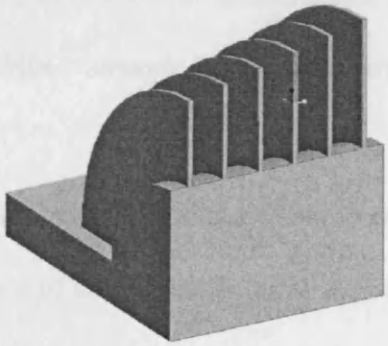

Figure 3.7. Crossed section of the "Rib" test part featuring an AR range of 40-50.

Rib test part having an AR range of 40-50. These test parts were used to empirically investigate what could be the maximum AR achievable with the VIC process both for LM25 and ZA12 by varying the mould pouring temperature.

3.3.1. Casting soundness and typical defects

First, the evaluation procedure included a visual inspection of the castings. This step aimed to assess their overall quality, reporting the presence of major defects such as casting soundness, determining the quality of the reproduction of small and intricate features and also judging the general surface finish of the castings. The castings were removed from the investment using a water jet unit and separated from the gating system.

The small characters with AR of 1.7, 2.3, and 2.4 were successfully reproduced on the Logo parts using LM25 and ZA12 (Figures 3.8.a and 3.8.b). However, such good definition was not achieved when the part was cast in 316 S16. With the latter alloy, a chemical reaction between the ceramic mould and the molten metal created an oxidation layer surrounding the castings, considerably affecting the definition and sharpness of their smallest features (Figures 3.9.a and 3.9.b). Also, on the surface of some 316 S16 castings there were signs of small flashes, resulting from the formation of cracks in the phosphate M062 ceramic investment during the firing process (Figure 3.10).

Small spherical imperfections were found in some complex features of the Logo part as well as on the surface of some ribs (Figures 3.11.a and 3.11.b). They were the result of air bubbles trapped on the surface of the wax patterns that were not evacuated during embedding. Possible reasons for these defects could be the position of the patterns in the casting tree, insufficient vacuum, and/or inadequate slurry consistency.

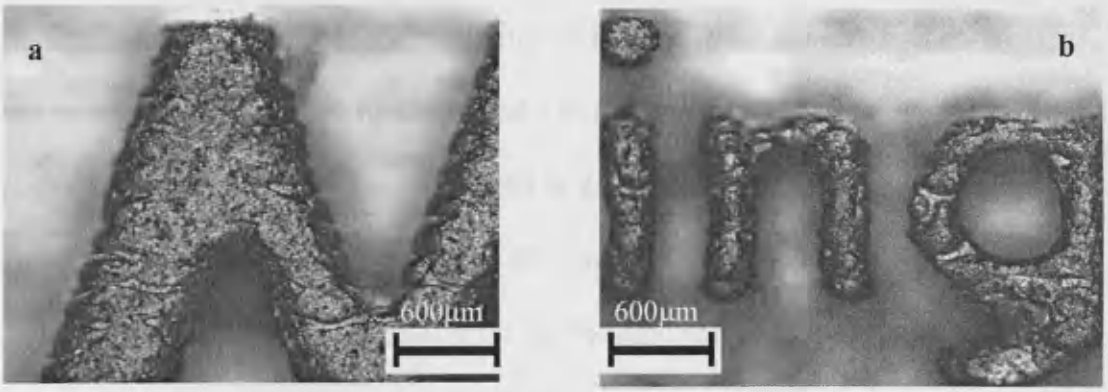

Figure 3.8. Logo features cast in ZA12: a) "M"; b) "ing".

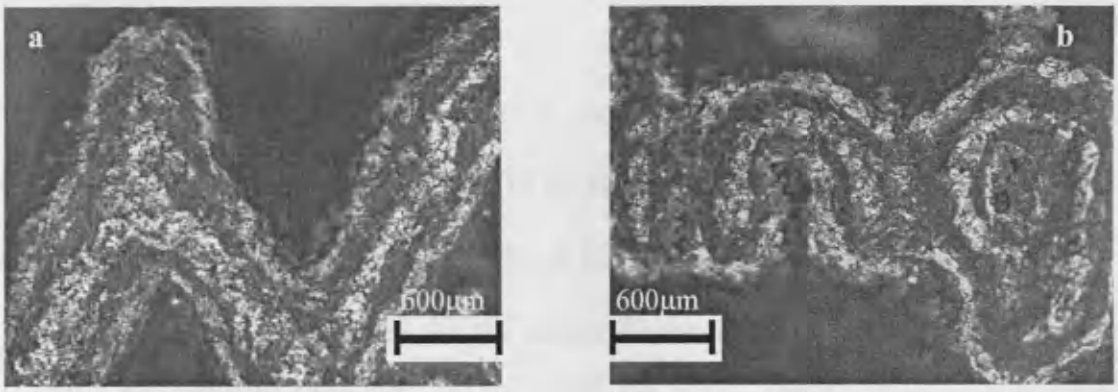

Figure 3.9. Logo features cast in 316 S16: a) "M"; b) "ing".

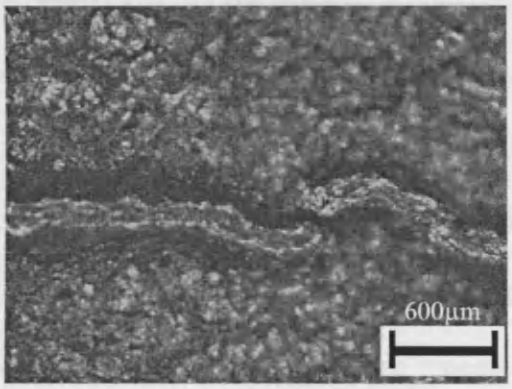

Figure 3.10. Flashes on 316 S16 casting due to mould cracking during firing.

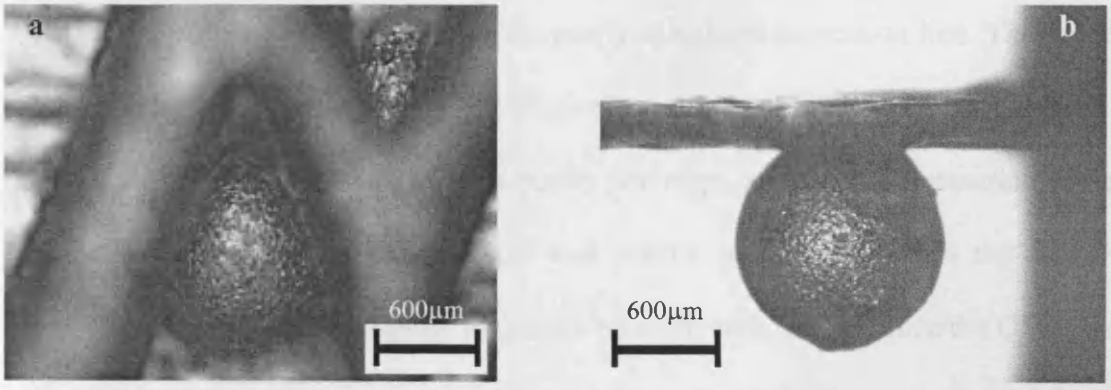

Figure 3.11. Casting defects due to embedding problems: a) Logo "M"; b) Rib.

The best results in terms of reproducibility of features were achieved when the parts were cast in ZA12, followed by LM25 and 316 S16.

The Pyramid parts were only produced in ZA12 and LM25 since 316 S16 did not exhibit enough castability to properly fill the smallest mould cavities. Generally, LM25 and ZA12 performed similarly for all Pyramid test parts, producing successful and sound castings.

3.3.2. Pyramid measurement procedure

The measurements of the Pyramids were conducted from two different observation sides, ZX and ZY (Figure 3.12.a). The nominal dimensions in ZX and ZY are: 3.83, 2.56, 1.7, 1.14, 0.76, 0.5, 0.34, 0.22, and 0.15 mm, respectively (Figure 3.12.b). The procedure followed for the measurement of the Pyramids consisted in measuring the steps 1 to 9 observed from each observation side, e.g. ZY as in figure 3.12.b. Once a Pyramid was positioned on the system, it remained in a fixed position throughout the entire measurement procedure. As illustrated in figure 3.13, the system automatically selected a minimum of ten points by contrast differentiation inside a predefined frame drawn by the operator around the edge of interest. Using the least square criterion, the system approximated the first edge observed (Ei) by a line (Li). A second and independent selection of data points was then repeated on the same edge. This time, the operator asked the system to approximate a middle point (Pi), located half way between the extremities of the newly calculated regression line. The process was then repeated for each of the ten edges observed per observation side. The need to select two independent sets of data points per edge, so that the measuring system could calculate an approximated line and middle point, arose from the fact that regressed lines exhibited angular variations between each other. Since the QV system was unable to calculate the distance between two non-parallel lines, it required the

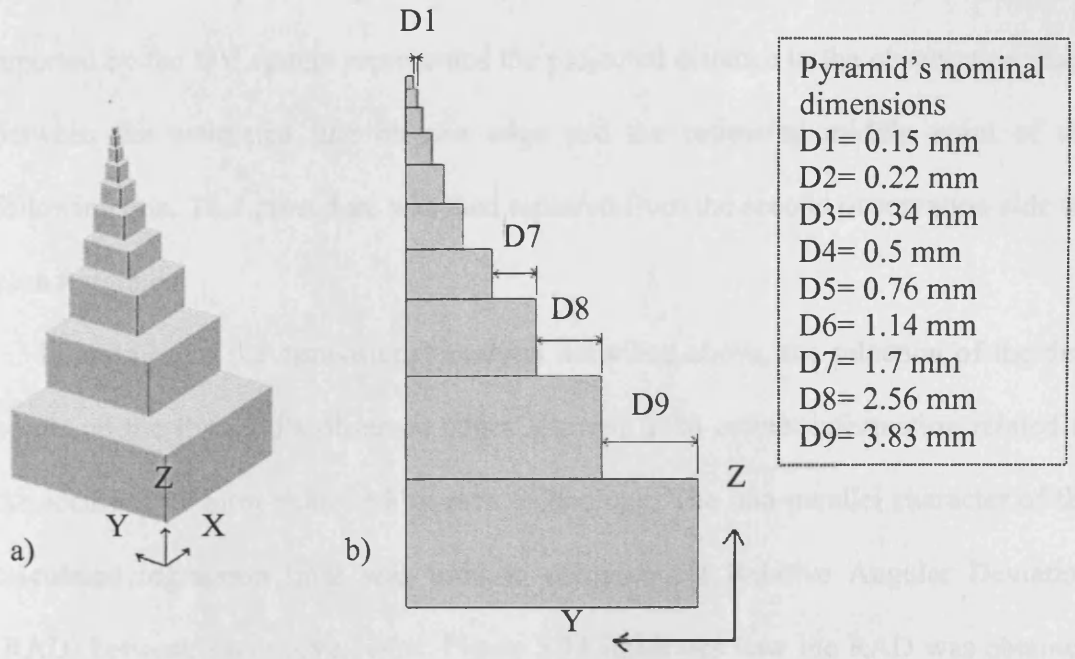

Figure 3.12. Pyramid test part: a) Observation sides ZY and ZX; b) Measured dimensions from the ZY observation side.

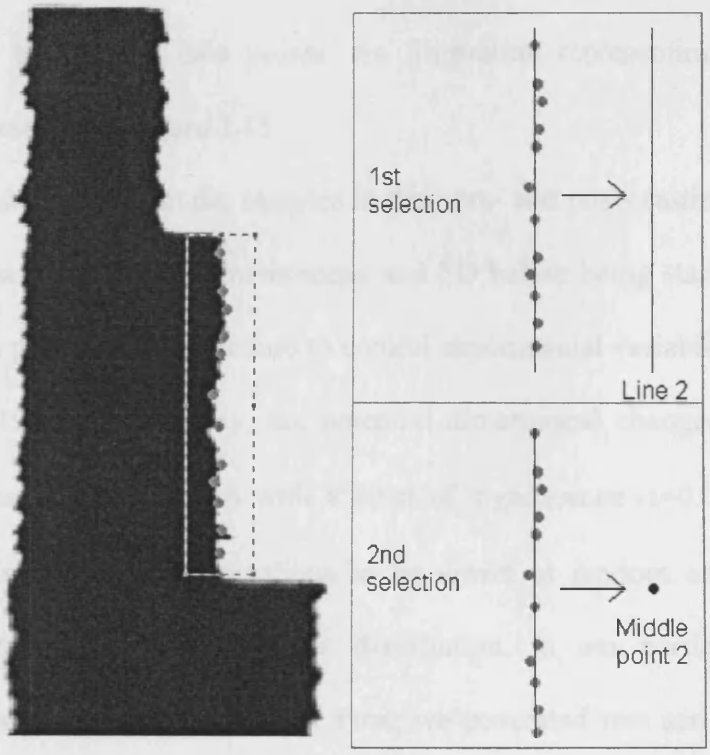

Figure 3.13. Data point selection on a Pyramid's second edge (E2).

calculation of an equivalent point. Thus, the measured distance in the observation side reported by the QV system represented the projected distance in the observation plane between the estimated line on one edge and the estimated middle point of the following one. This procedure was then repeated from the second observation side for each Pyramid.

In addition to the dimensional analysis described above, the selection of the data points on the Pyramid's observed edges allowed us to collect information related to the accuracy of form exhibited by each technology. The non-parallel character of the calculated regression lines was used to compute the Relative Angular Deviation (RAD) between successive edges. Figure 3.14 illustrates how the RAD was obtained between three regression lines at the tip of a Pyramid. Then, the spreading of each set of data points was used to assess the straightness of the Pyramid's edges. The straightness value, reported in millimetres, represented the diameter of the smallest cylinder that bounds the data points. An illustration representing this theoretical cylinder is presented in figure 3.15.

The data collected from the samples in their pre- and post- casting state were first compared based on their arithmetic mean and SD before being statistically analysed by applying a paired t-test procedure to control experimental variability (Montgomery and Runger 1994). In this way, the potential dimensional changes brought by the casting process were estimated with a level of significance α=0.05. The use of a paired t-test requires the observations to be drawn at random and the difference between pairs to follow a Gaussian distribution. In our particular case, these assumptions were verified as follows. First, we generated two series of ten random numbers, respectively for the pattern and casting stages, to determine in which order the Pyramids had to be measured. Then, a descriptive analysis of the difference between pairs was done to assess whether or not the assumption of a Gaussian

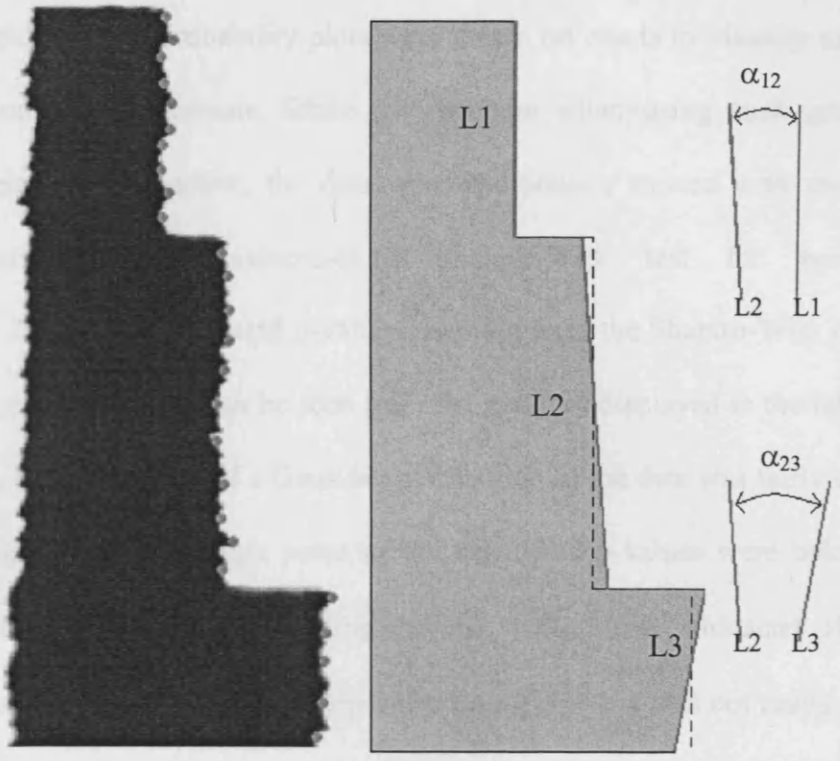

Figure 3.14. Calculation of the RAD based on the non-parallelism character of the regressed lines.

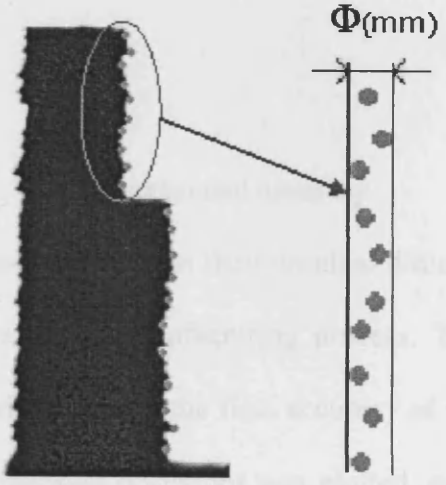

Figure 3.15. Edge straightness based on a theoretical smallest cylinder bounding the data points.

distribution held. Normal probability plots were drawn on charts to visually assess if this assumption was appropriate. Since the outcome when using such graphical methods is relatively subjective, the data were additionally treated with the more formal statistically-based goodness-of-fit Shapiro-Wilk test for normality (Montgomery 2005). The calculated p-values resulting from the Shapiro-Wilk test are provided in appendix 3.2. As can be seen from the p-values displayed in the tables of appendix 3.2., the assumption of a Gaussian distribution of the data was fairly correct in our investigation. Even though some of the calculated p-values were below the level of significance (α =0.05), indicating that the "non-normal" character of these data was statistically significant, their departure from normality was not really strong (0.0001<p). Moreover, it is recognized that even though the t-test assumes a normal distribution of the data, it is relatively insensitive to this assumption (Montgomery and Runger 1994). Therefore, a small departure from normality of some of the treated data should not have any influence on the results' interpretation from the paired t-test analysis.

3.3.3. Accuracy of position: linear dimensional accuracy

The deviations of micro-features from their nominal dimensions are important in studying the accuracy of a micro-manufacturing process. Thus, to investigate the influence of the manufacturing route on the final accuracy of the castings, the length-scale dependence of the dimension deviations was plotted, as shown in figures 3.16 and 3.17. Additionally, these charts display the deviation of castings' dimensions from their nominal in percentage terms. The accuracy of each process chain was characterised by the amplitude of the deviations from their nominal, while their

a)

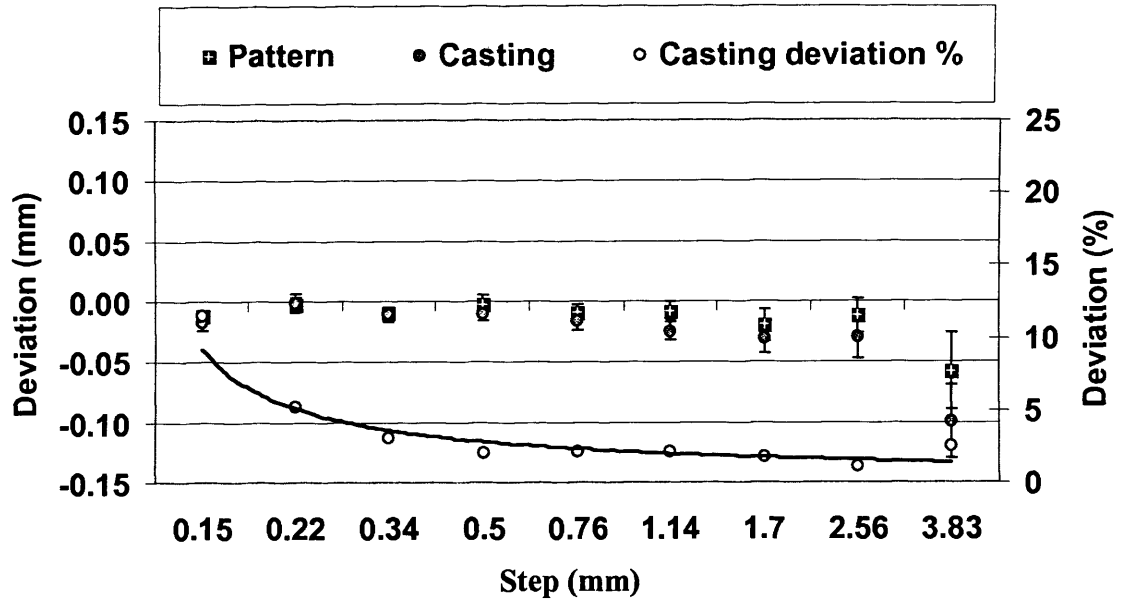

b)

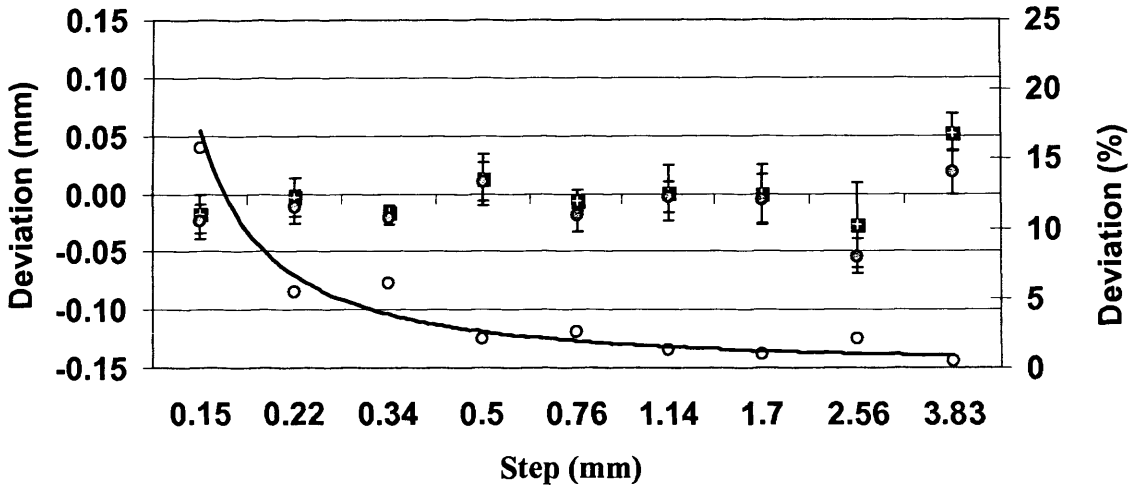

Figure 3.16. ZA12 deviation from the nominal dimensions specified on the CAD drawing: a) PM; b) ThJ.

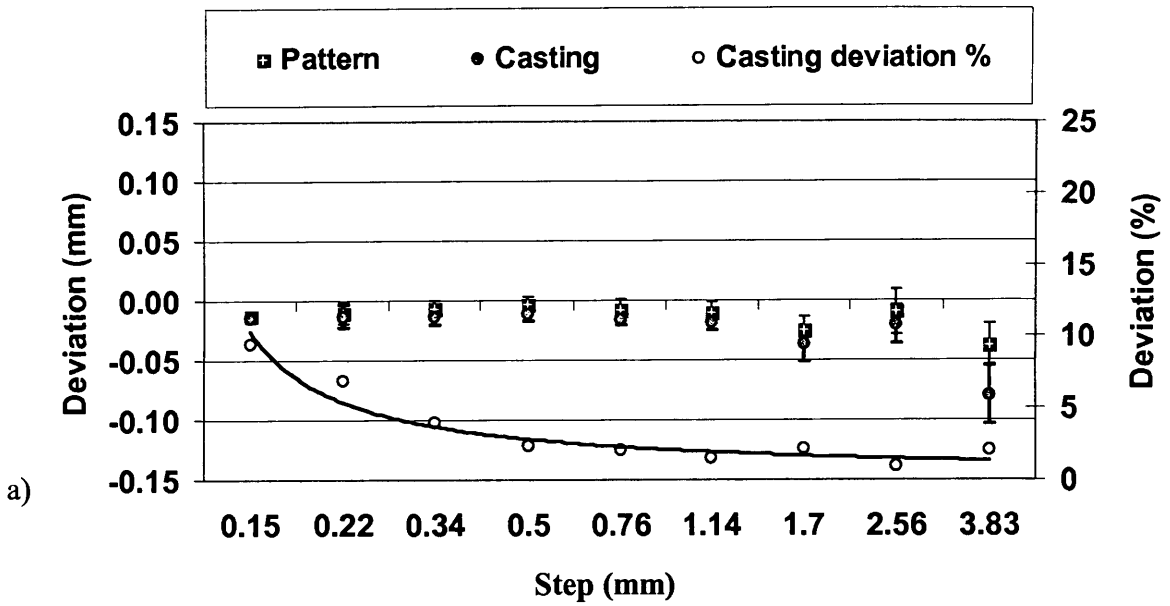

a)

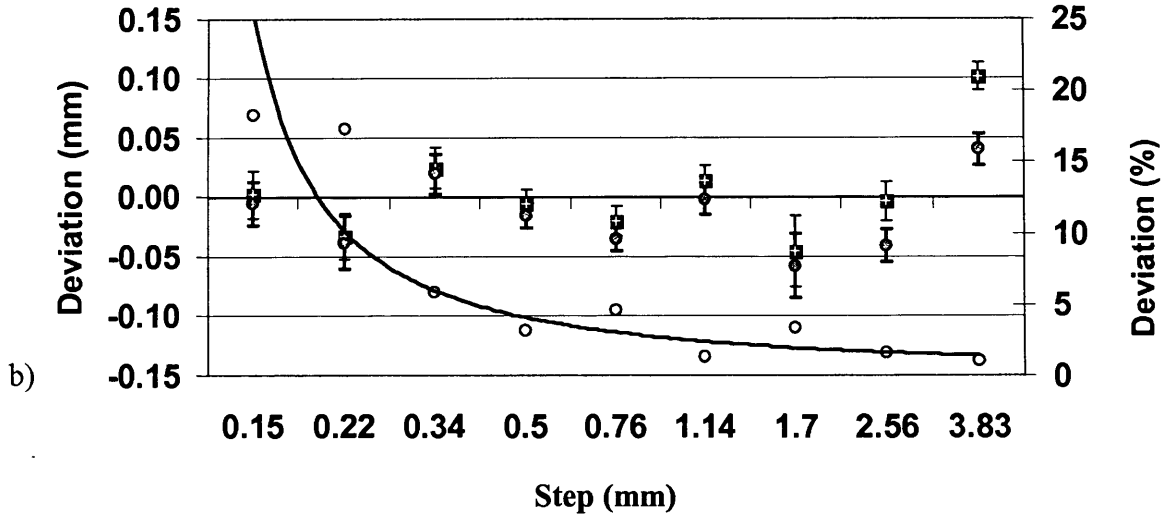

b)

Figure 3.17. LM25 deviation from the nominal dimensions specified on the CAD drawing: a) PM; b) ThJ.

degree of scatter, as well as the SD bars plot on the graphs, provided information on their consistency.

As illustrated by the charts of figures 3.16 and 3.17, the PM castings exhibited more accurate and consistent results than ThJ regardless of the alloy employed.

Generally speaking, the smaller the feature measured, the higher was the percentage of deviation from the nominal. The maximum percentage of deviation revealed on the castings for features smaller than 340 μm was in the range of 5-10% and 5-20% for the PM and ThJ technologies respectively.

The deviation of the meso/micro-scaled features from their nominal dimensions for the ThJ patterns and castings was within ±50 μm (Figures 3.16.b and 3.17.b) but exceeded 100 μm for the largest step of 3.83 mm. The main reason for this was the volumetric solidification contraction occurring during cooling of the thermoplastic material. This shrinkage led to significant shape distortion of the patterns, resulting in an accuracy deterioration that affected both their linear and angular dimensions.

The PM process chain produced samples with the highest dimensional accuracy, within ± 50 μm as shown in figures 3.16.a and 3.17.a. The charts depicted a linear dependence between the deviations and the nominal dimensions, indicating the higher consistency of the process. It appeared that the biggest step of the patterns, at the base of the pyramids, exhibited a significantly higher deviation than the others. This was the consequence of building problems associated with the layer milling operation of the PM process, which affected the definition of some of the Pyramids' biggest steps.

The accuracy loss between the patterns and their respective castings, because of the metal shrinkage, was more pronounced for the bigger steps of the pyramids, where a relatively large volume of material had to solidify. The difference between the behaviour of the LM25 and ZA12 alloys was not significant, although LM25 castings exhibited a slightly higher shrinkage, probably due to the aluminium higher

solidification volume contraction at 6.5% for aluminium compared with 4.7% for zinc (Beeley 1972).

The results of the paired t-test statistical analysis performed on the lost patterns and respective metal castings are summarized in the tables of appendix 3.3. They show that the features with dimensions bigger than 1.7 mm underwent statistically significant changes for both alloys, with p-values much lower than the α-level (α=0.05). Smaller steps, which were associated with smaller sections of the pyramids, were less affected by the dimensional changes due to metal shrinkage between pattern and casting stages. However, it appeared that p-values associated with features smaller than 1.7 mm were sometimes slightly lower than the α-level. Even though in those cases the dimensional changes were significant from a statistical standpoint, the close proximity of the p-values to the level of significance may be insignificant from an engineering point of view.

3.3.4. Accuracy of form

3.3.4.1. Relative Angular Deviation

The arithmetic mean and SD of the RAD (expressed in degrees) for each sample group was plotted as a function of steps' nominal dimensions (Figures 3.18, 3.19, 3.20 and 3.21). No clear difference could be determined between the measurement results carried out on the YZ and XZ observation sides. For both studied processes, LM25 and ZA12 alloys performed similarly. Considering both technologies, it appeared that the steps with dimensions in the range 0.34 to 2.56 mm were fabricated consistently with the highest accuracy. For that particular dimensional range, the maximum RAD measured was in the order of 1°. The accuracy and the consistency of the PM's patterns and their respective castings were the highest, especially for the steps with dimensions below 340 μm, while the ThJ technology could not achieve the same level

of accuracy and consistency for this dimensional range. The reason why ThJ seemed to have reached a sort of accuracy threshold for features below 340 μm, might be explained by the different manufacturing processes employed by each technology. PM offers the possibility to build external support walls enclosing the perimeter of the pattern, creating a mould to be filled by the build material. Good wetability of the building material onto the support ensures a proper and complete filling of the cavity. Any excess volume of the building material is further rectified during the layer milling stage. Therefore, after dissolution of the support material, PM's patterns and respective castings exhibit a sharp resolution of fine details (Figure 3.22). On the other hand, ThJ only uses its positional accuracy capabilities for depositing droplets of building material at a temperature slightly above its phase transition. Therefore the wetting property of the thermoplastic material employed dictates the degree of spreading of the droplets onto the deposited surface. This microscopic behaviour may be insignificant for patterns having conventional dimensions but becomes increasingly important when considering micro-features defined by a volume equivalent to that of a few hundred droplets only. This phenomenon is highlighted by the lack of sharpness of ThJ's Pyramid's tip of figure 3.23.

Interpreting the p-values from the paired t-test analysis performed on the patterns' and castings' RAD in appendix 3.3, it seemed that the duplication process had no statistically significant influence on this parameter ($p>0.05$).

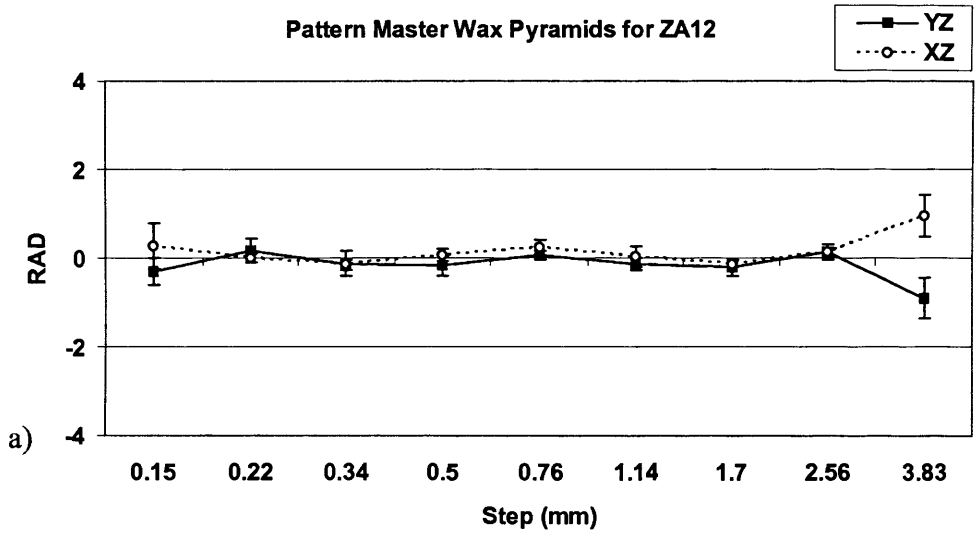

a)

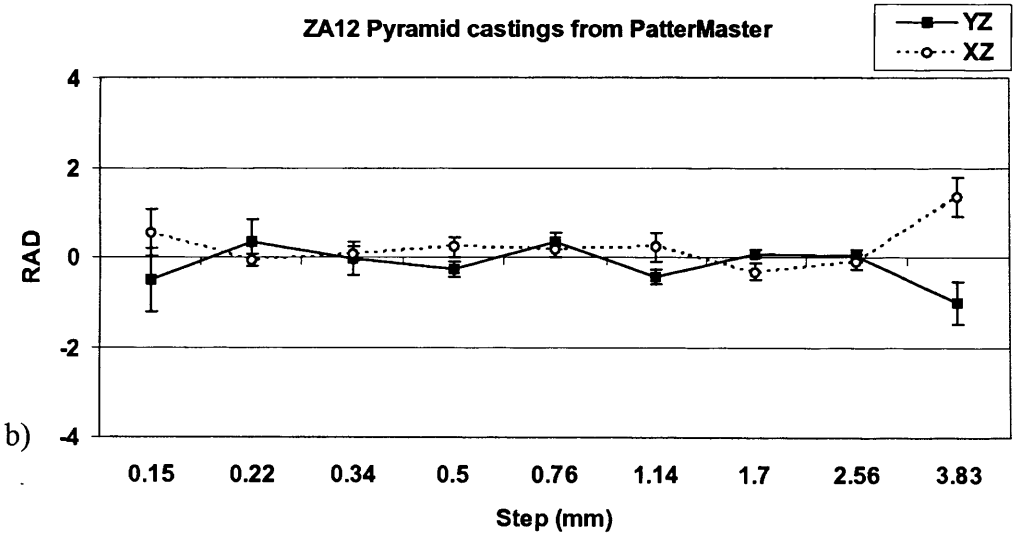

b)

Figure 3.18. RAD of PM's Pyramids cast in ZA12: a) Lost samples; b) Castings.

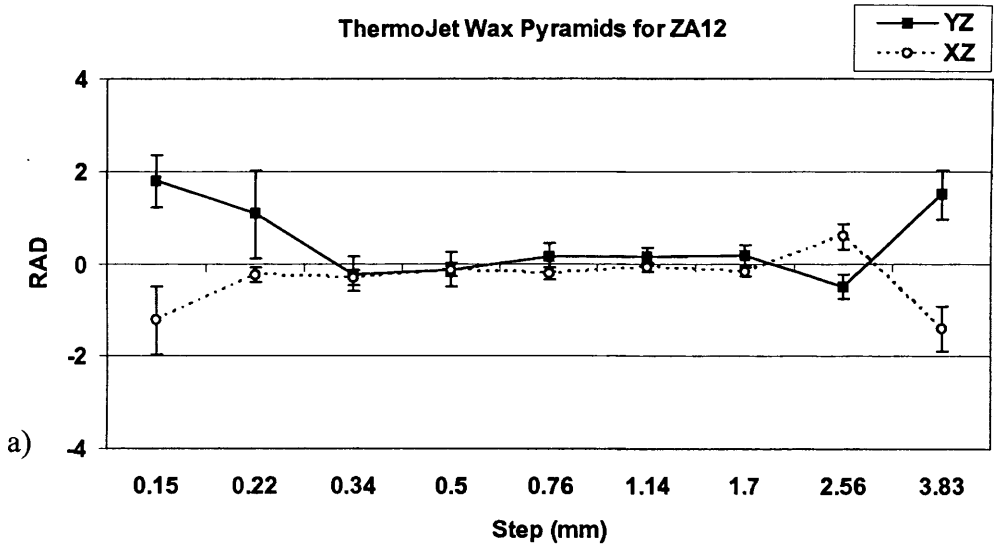

a)

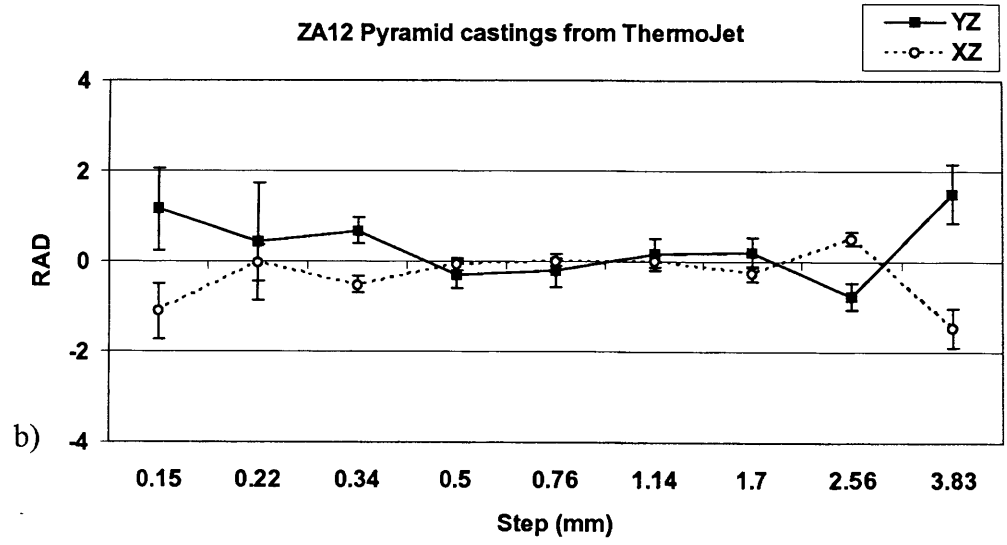

b)

Figure 3.19. RAD of ThJ's Pyramids cast in ZA12: a) Lost samples; b) Castings.

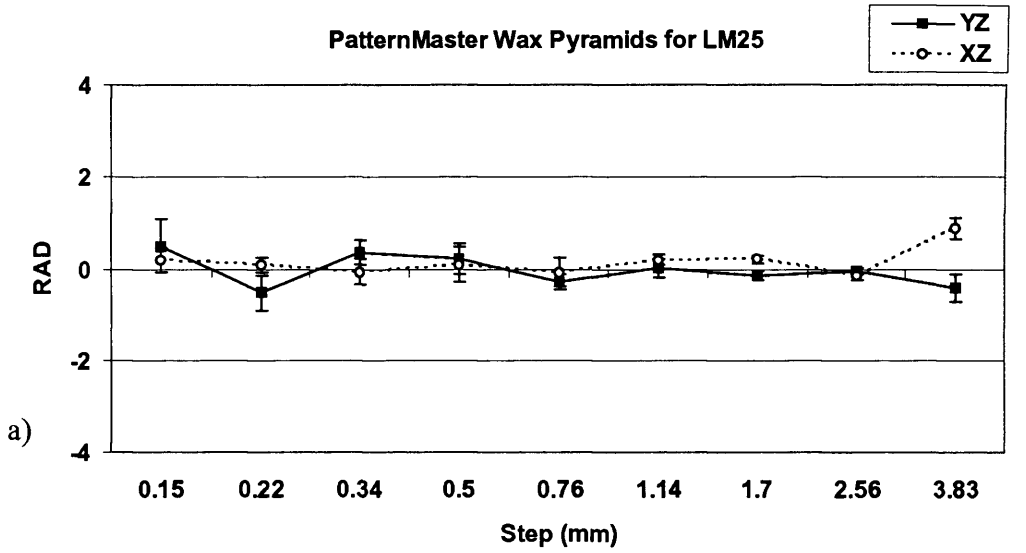

a)

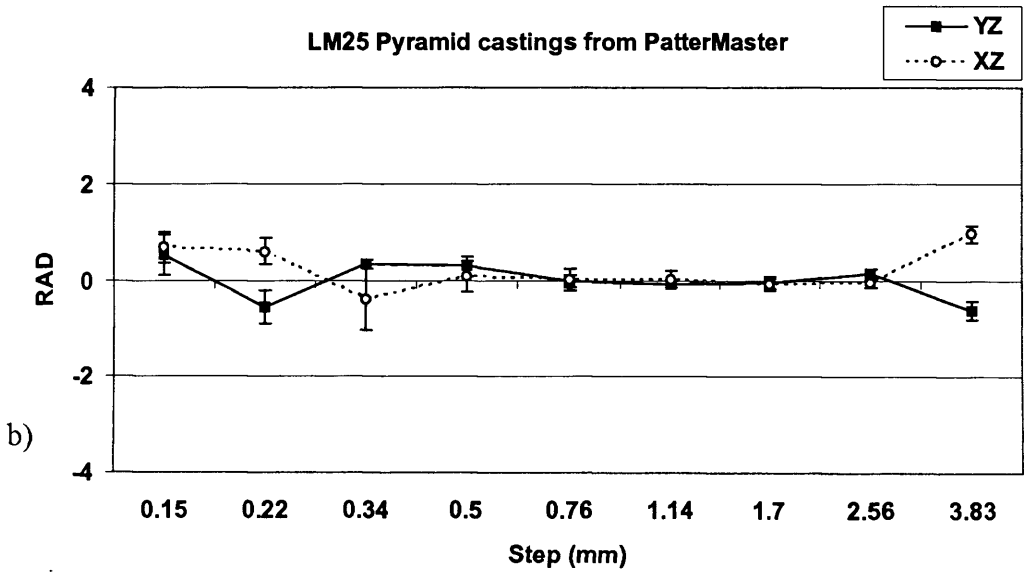

b)

Figure 3.20. RAD of PM's Pyramids cast in LM25: a) Lost samples; b) Castings.

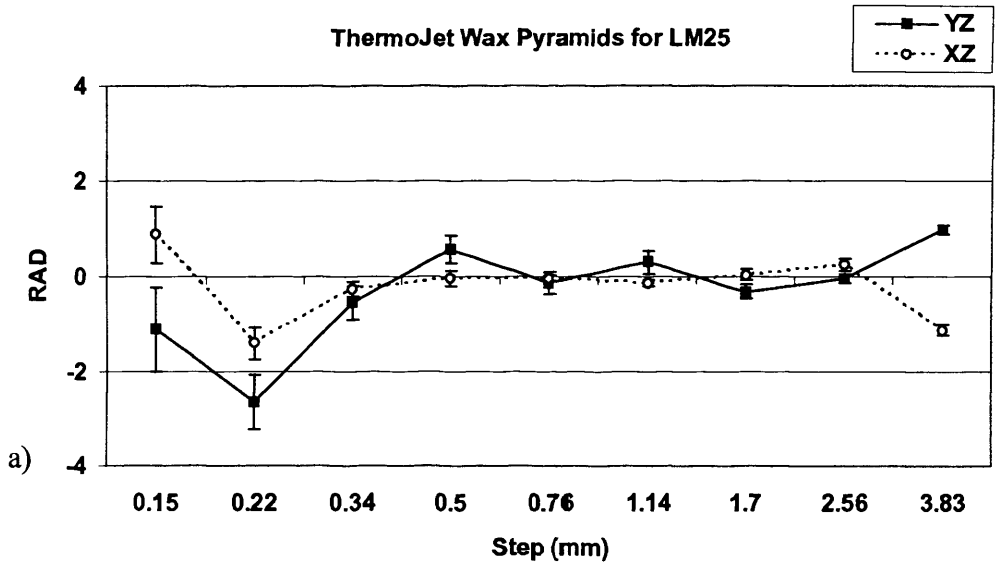

a)

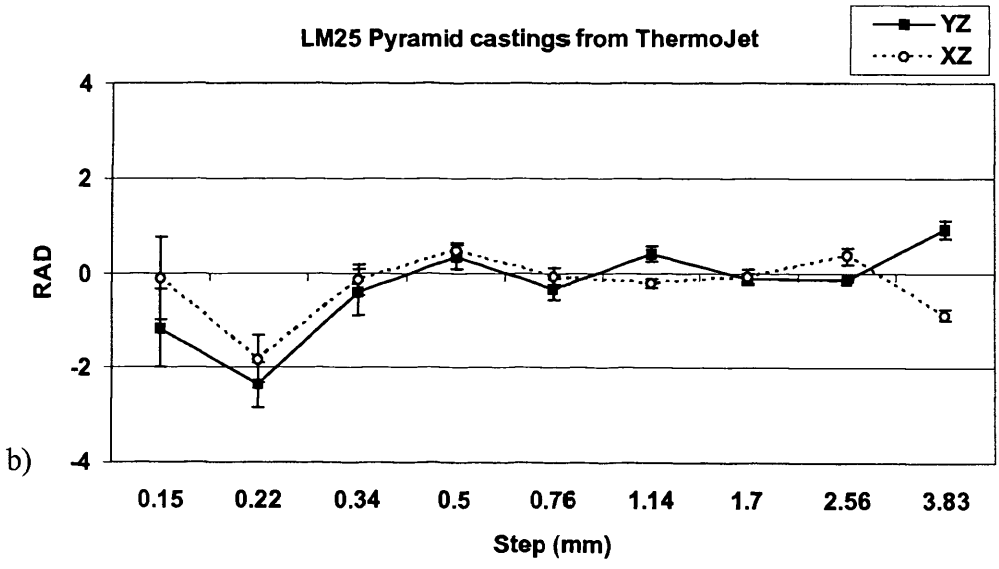

b)

Figure 3.21. RAD of ThJ's Pyramids cast in LM25: a) Lost samples; b) Castings.

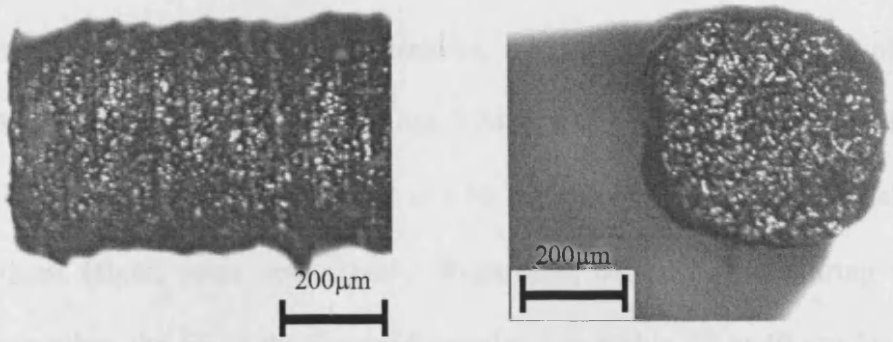

Figure 3.22. Sharpness of PM's Pyramids'tip cast in ZA12.

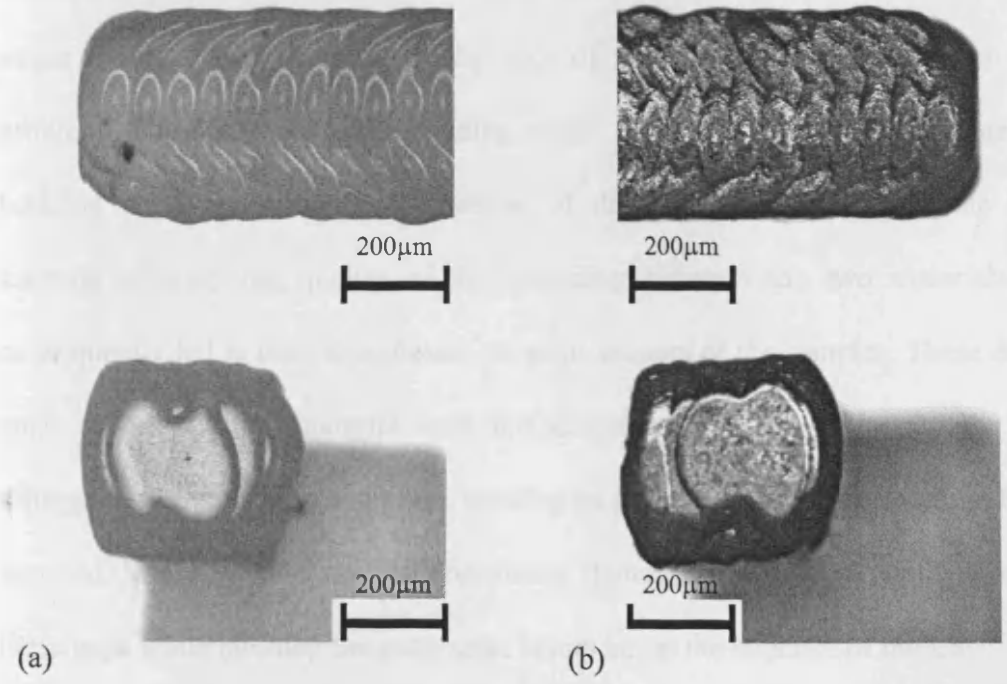

Figure 3.23.Textured surface of ThJ's Pyramids'tip highlighting the influence of the droplets' size relatively to that of the feature built:
a) Lost pattern; b) Casting.

3.3.4.2. Edge Straightness

Studying this parameter, it appears that no distinction can be made between each observation side. Therefore the arithmetic mean and SD calculated for the edge straightness (ES), expressed in millimetres, includes both ZX and ZY observation sides. The results were plotted on figures 3.24 and 3.25 as a function of the Pyramids' edges. Edges were numbered from E1 to E10, referring to the Pyramids'smallest (Tip) and biggest (Base) steps respectively. Regardless of the manufacturing route and employed alloy, the ES of the Pyramid samples was within 20 to 40 μm for the range of edges E1 to E9. Pyramids produced by both technologies exhibited a deterioration of the ES with the increase of the step size, which was mainly attributable to the thermoplastic material shrinkage during solidification and further cooling. The worsening of the ES became even more significant for the edges E10 for both technologies. However, in the case of PM, the much stronger deterioration of the E10 edges (80 to100 μm) was a consequence of material shrinkage and layer milling problems faced at the pattern building stage. More precisely, the shrinkage of the building material during the deposition of the very first layers onto the support material affected the quality of the bounding between the two materials which consequently led to their detachment on some corners of the samples. These detached areas of the building material were further broken and removed from the sample through the layer milling operation, creating an empty volume in place of the building material. When the part was not completely damaged, the system managed to fill in these gaps while building the successive layers but at the expense of the ES.

Regarding the paired t-test analysis, no statistically significant differences were found in the pre- and post-casting states of the samples ($p>0.05$) (Appendix 3.3).

a)

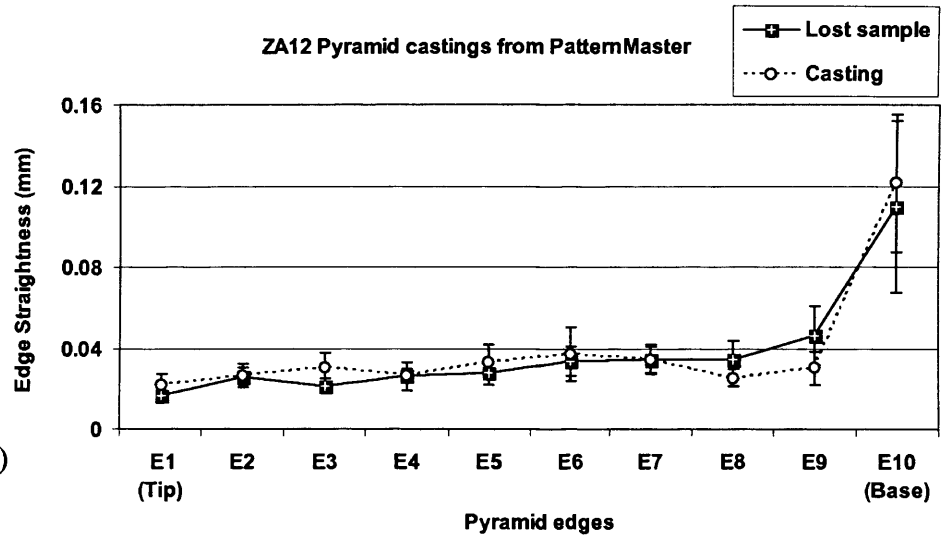

b)

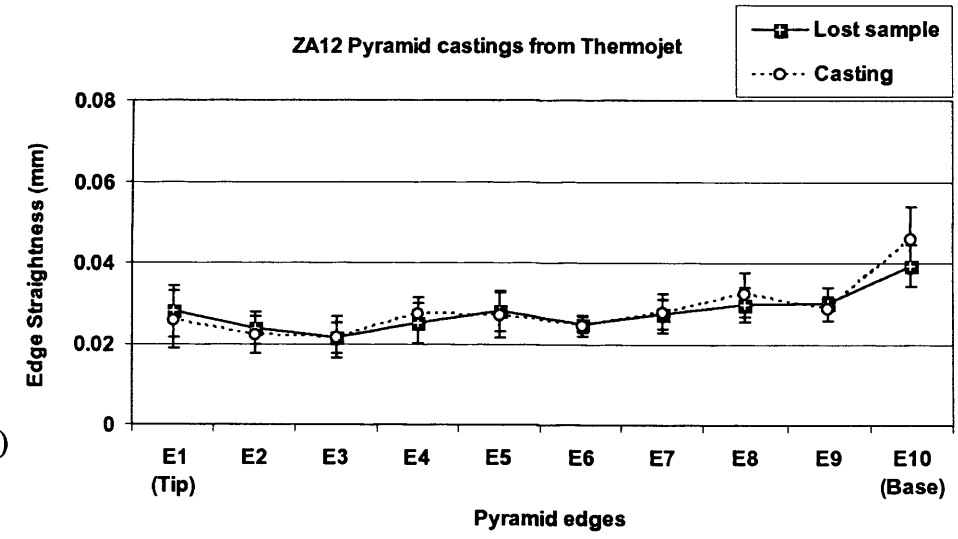

Figure 3.24. ES of the Pyramids' lost samples and their respective ZA12 castings: a) PM; b) ThJ.

a)

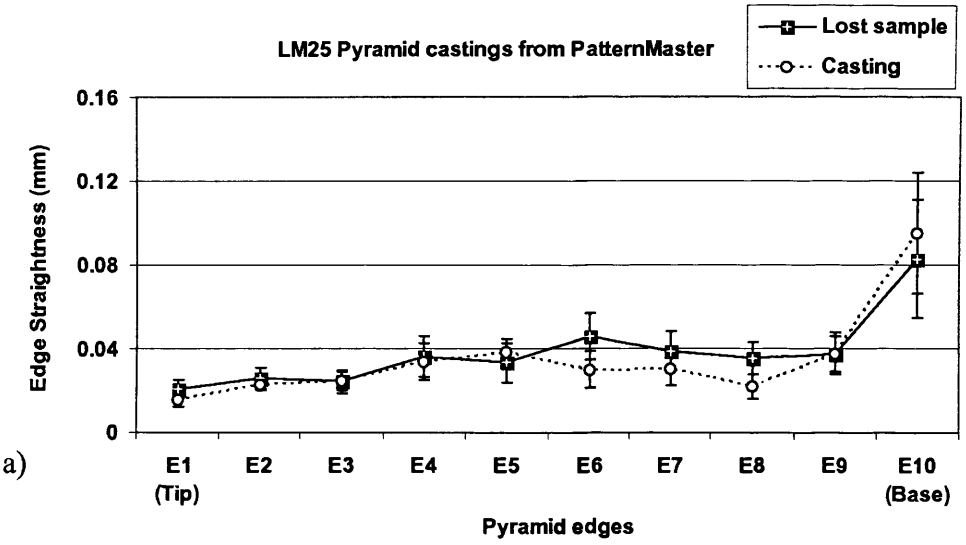

b)

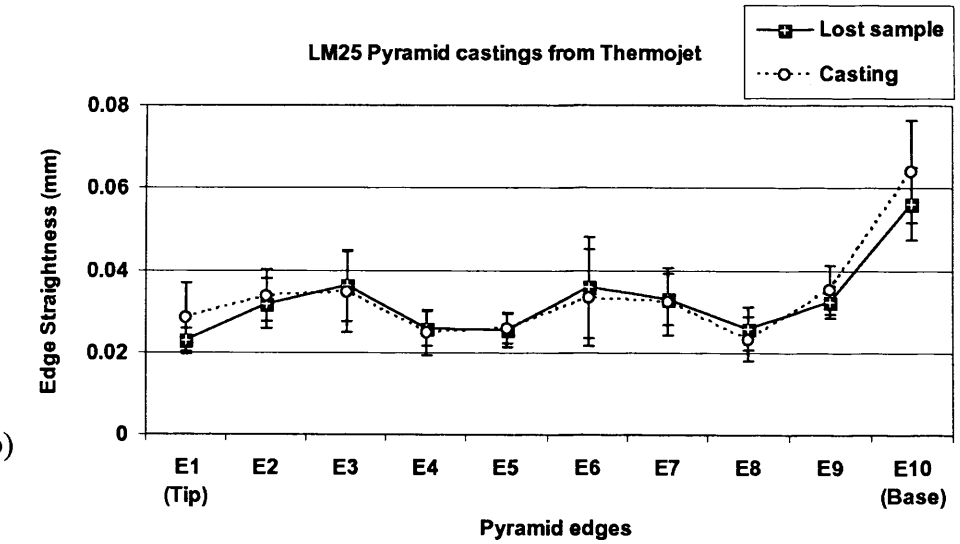

Figure 3.25. ES of the Pyramids' lost samples and their respective LM25 castings: a) PM; b) ThJ.

3.3.5. Maximum aspect ratio achievable on the rib test part

When casting micro features with high AR, the successful filling of the mould is a challenging task since not only does it rely on the maximum flow length achievable by the alloy for specific materials and processing parameters but also needs to overcome the influence of microscopic forces such as surface tensions. Also, the presence of trapped gases in the mould prior to casting can create a back pressure effect, thus limiting the ability of the molten alloy to completely fill the mould. Moreover, the problem becomes even more complex if one considers the dynamic and thermal natures of the casting process itself. The fact that VIC technology combines vacuum of the mould before casting with overpressure after casting on top of the sprue gives to the process a considerable advantage over conventional casting processes in overcoming these mould filling issues.

This section investigates the capabilities of the VIC process for casting features in the micrometre range with high AR using conventional casting alloys such as ZA12 and LM25.

The design of the Rib test parts incorporated six ribs with a thickness of 250 μm and several ranges of AR as described earlier in the chapter. The choice of a rib thickness of 250 μm was made since it was the minimum thickness that the ThJ technology could consistently produce without failure and within close dimensional tolerances. The varying parameter for this investigation was the mould pouring temperature since it is known for being the most important parameter governing the rate of solidification when considering casting technologies involving relatively insulated moulds such as in VIC (Flemings 1974). Experiments consisted of gradually decreasing the mould temperature from 450°C until failure of the castings.

3.4. Summary

This chapter reports an experimental study that compared the capabilities of two RP building machines, PM and ThJ, for producing accurate sacrificial patterns having meso/micro-scaled features to be duplicated in metals such as LM25, ZA12 and 316 S16 through VIC and CIC. The soundness and overall quality of the castings together with the accuracy of shape and form of the two manufacturing processes were assessed and compared. Additionally, the maximum AR achievable on 250μm thick features using both LM25 and ZA12 was investigated. The following general conclusions were drawn:

- From a visual stand point, ZA12 and LM25 performed similarly. Both alloys exhibited good reproduction of the micro-features present on the lost patterns. This was not the case with the 316 S16 alloy, for which the micro-replication capabilities were limited by both incomplete mould filling and a chemical reaction between molten alloy and investment material which created an oxidation layer, strongly affecting the resolution of the cast micro-features.
- The overall performance in terms of accuracy and consistency of the two processes were relatively similar with an advantage to PM which exhibited slightly better results.
- The accuracy of ThJ and PM patterns appeared to be the key factor for producing high quality castings because the metal shrinkage did not affect significantly the accuracy of the features of the Pyramids that were smaller than 1.7 mm. When considering meso/micro features, the dimensional variability caused by the metal casting step of the LWP is therefore of minor importance in comparison with inaccuracies attributable to the pattern building processes.

- Using conventional casting machines, parts featuring ribs with thicknesses of 250μm and maximum AR of 50 and 60 were consistently produced in LM25 and ZA12 respectively with a minimum mould pouring temperature of 250°C.

CHAPTER 4: Benchmarking of Lost Wax Process (LWP) using two RP technologies with the Fcubic direct shell process for producing micro-castings

The use of RP technologies for manufacturing functional prototypes has been undergoing a dynamic development over the past twenty years, leading to the emergence of new technologies and broadening the range of available materials and potential applications. An evolution of considerable interest in the field of metal casting of meso/micro components is the development of new manufacturing techniques such as the Direct Shell Process (DSP). The technology studied in this chapter has been developed by Fcubic (www.fcubic.com) and offers the possibility of producing ceramic shells for metal casting directly from the CAD model, without the use of sacrificial patterns. This different approach significantly shortens the manufacturing route required for the production of micro-castings as highlighted by the following two technological chains:

- **Fcubic-DSP**: 3D CAD modelling > fabrication of **Fcubic DSP shells** > **flask preparation** > **heating** > casting > shell removal.
- **LWP**: 3D CAD modelling > fabrication of **ThJ/PM patterns** > **cluster preparation** > **vacuum embedding** > **burning** > casting > shell removal.

The purpose of this chapter is to investigate and assess the capabilities of the new Fcubic DSP for producing metal casting of meso/micro components through benchmarking with the conventional Lost Wax Process (LWP). The choice of a benchmarking approach was made since it is a useful tool providing accurate and reliable information on the system performance when considering a specific test part.

4.1. The Fcubic-Direct Shell Process

4.1.1. Technology and materials

Fcubic has developed high precision ink jet equipment to be used for manufacturing parts or functional printing on substrates. The process uses an RP technology to manufacture net shape functional parts. The company produces two types of machines with different building capacities, the fcubic c300 and fcubic c50 (Figure 4.1), the latter being used in our experiments as more appropriate for the manufacture of small parts (building envelope size 50x150x50 mm). Since raw materials are powder-based, it offers the possibility of manufacturing ceramic parts including zircona, stainless steel (316L) and other ferrous alloys, titanium, etc. depending on the needs and applications. This four axis system has a maximum positional accuracy of the print head of 2μm and exhibits an overall resolution of approximately 35 μm in x, y and z. When considering the manufacture of small parts, in the range of a few millimetres high, the manufacturer claims achievable productivity similar to that of injection moulding giving the process a considerable advantage over other RP technologies.

For producing the ceramic cores Fcubic used the standard "stl" file format. The CAD files were processed by a design tool that allowed: (i) shelling of the file; (ii) design of the feeding system; (iii) advanced slicing and (iv) accurate bitmap generation.

The ceramic direct shell materials used in the experiments were plasma sprayed zirconia (ZrO_2) spherical particles with a diameter of 20-70 μm infiltrated with zirconia soil ink catalyst (Nyacol $ZrYS_4$). After printing, the green part present on the building platform was placed into a furnace for 1h at 900°C. This post-curing step aimed at strengthening the shells by sintering the catalysed ceramic particles together. The presence of Nyacol enhances the necking between the 'wet' particles and also permits the lowering of the processing temperature.

a)

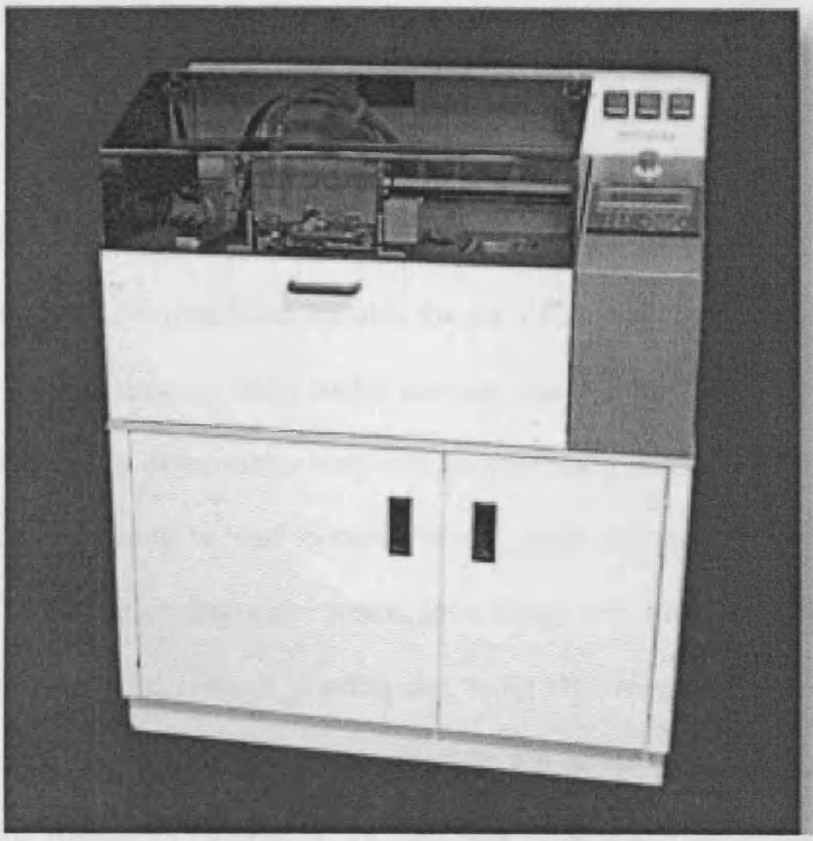

b)

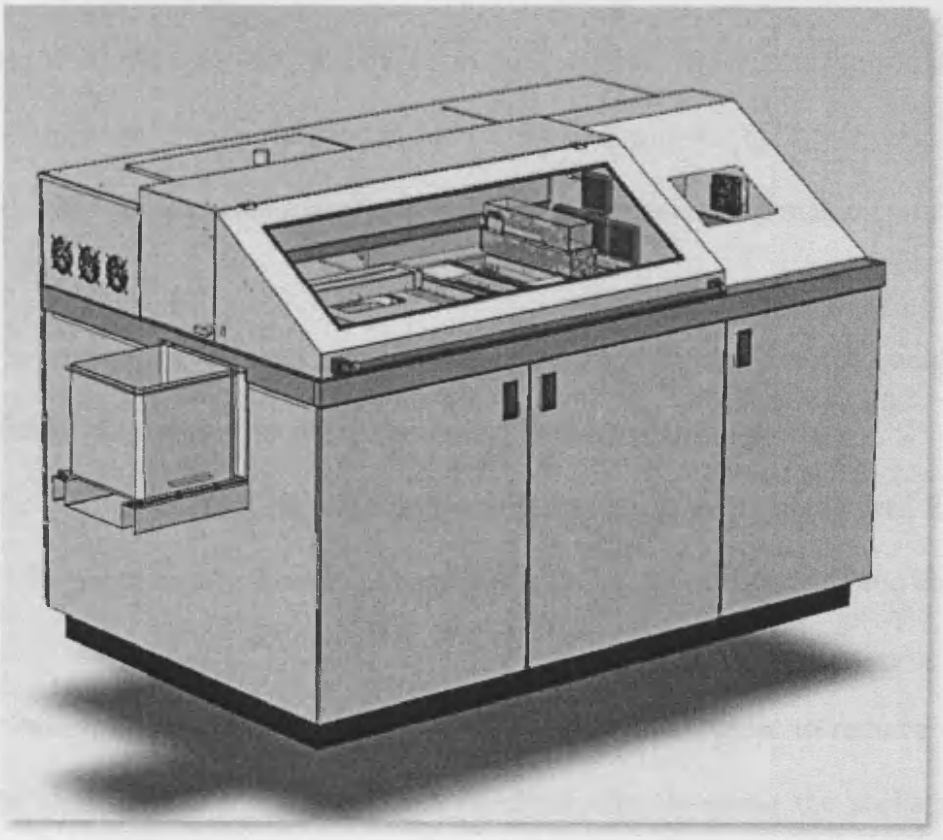

Figure 4.1. Fcubic machines: a) c50 demonstrator; b) c300 demonstrator.

Finally, the shells were cleaned from the unsintered surrounding and trapped material by combining vibration and blowing.

4.1.2. Casting production procedure

The production of casting block moulds for the VIC technology available in the MEC was achieved by pouring ceramic slurry under vacuum into a flask containing the wax tree. Since the flasks used in our experiments were not geometrically compatible for a straightforward implementation of ready to cast ceramic shells, their design had to be modified. CAD drawings of the modified flasks are presented in figure 4.2. First, the sprue of the shell was joined to a prefabricated ceramic pouring cup using high temperature resistant glue (Figure 4.2.a). Then the flask was placed and clamped on top of the shell/pouring cup sub-assembly (Figure 4.2.b). The empty volume of the flask was filled with coarse sand. Finally, the flask was closed from the back side end by a screwing system, which compressed the sand, thus insuring a proper holding of the shell inside the flask (Figure 4.2.c). This hybrid experimental design exhibited considerable advantages over the traditional mould making process:

- The ceramic investment material was replaced with sand, which could be recycled after casting, thus reducing the amount of waste ceramic materials.
- The burning-out process was significantly reduced to the time required for heating the flask up to the desired casting temperature, saving production time and energy.

After casting, the bottom of the flask was unscrewed in order to remove the sand and access the shell. The castings were then obtained after breaking the shells using a high pressure water jet unit.

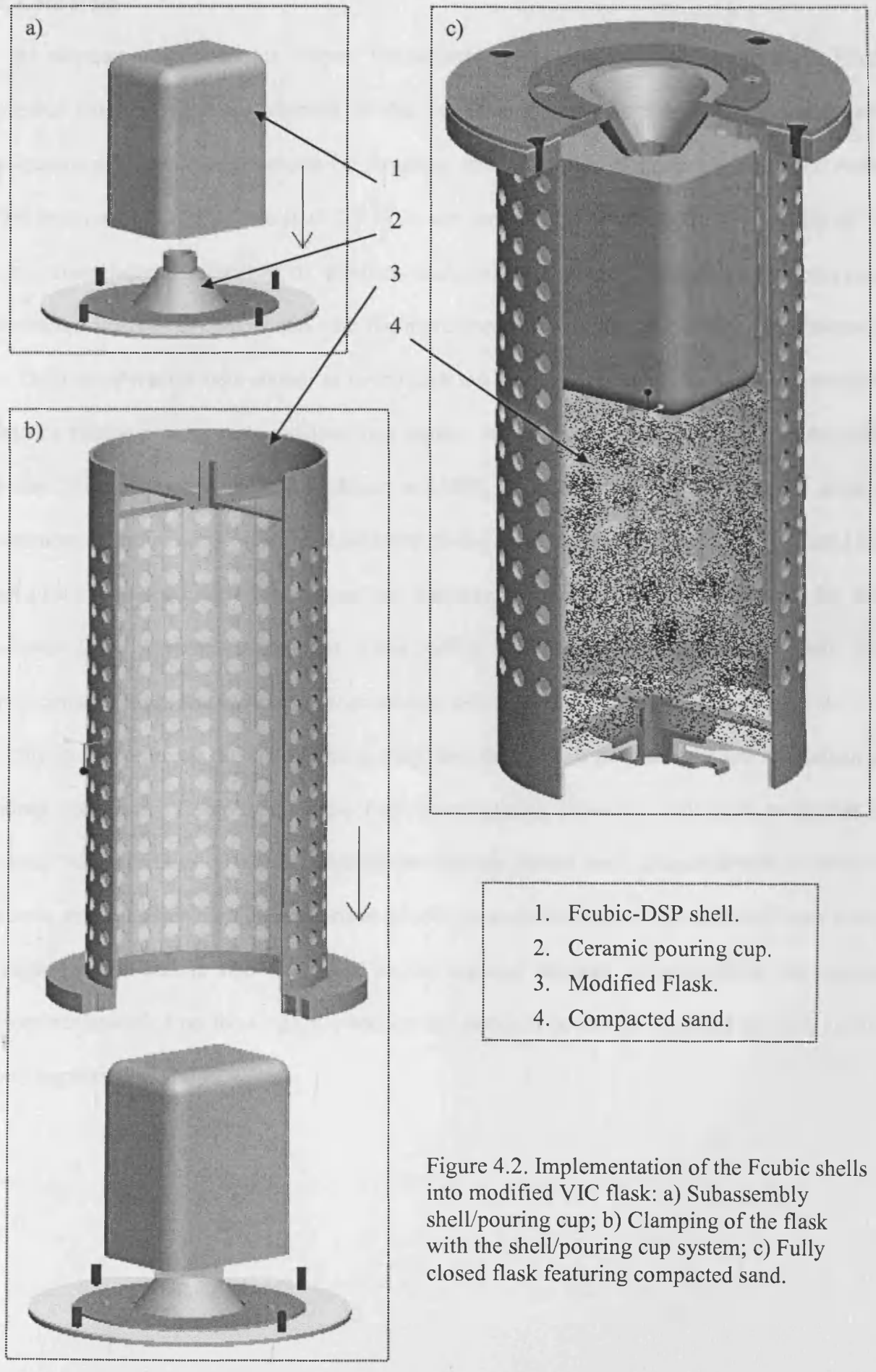

Figure 4.2. Implementation of the Fcubic shells into modified VIC flask: a) Subassembly shell/pouring cup; b) Clamping of the flask with the shell/pouring cup system; c) Fully closed flask featuring compacted sand.

4.2. Case study

As mentioned earlier in this chapter, benchmarking is a useful tool for comparing different processes since a judicious selection of the benchmark test part reveals the strengths and weaknesses of the studied processes by targeting the parameters of interest (Childs and Juster 1994; Ippolito et al. 1995; Chua et al. 2003). In our particular case, a strength is the ability of the Fcubic manufacturing process to produce accurate and consistent castings incorporating meso/micro features in comparison with the more conventional processes studied in Chapter 3. The Logo and Pyramid were chosen as benchmark test parts in this study. The castings produced using the Fcubic process were analysed in a similar way to those fabricated applying the LWP process. The Logo test parts were produced in LM25, ZA12 and 316 S16 and used for a visual assessment of the castings' quality. Additional to the parameters analysed on the Pyramid test parts in the previous chapter, roughness and porosity measurements were carried out for both processes. Five Pyramids were cast using LM25 and ZA12, ten castings in total. The experimental settings and measurement procedure were identical to those used in Chapter 3.

The study compares the soundness, quality, and the relative production costs and labour of castings produced by employing these two manufacturing processes. For each parameter of interest, the capabilities of the investigated two process chains were compared both in terms of accuracy and consistency. The comparison of each process in terms of accuracy and consistency in respect to the feature size was based on the castings' average deviation from the nominal dimensions specified on the CAD file and on the standard deviation exhibited by each sample group respectively.

4.2.1. Casting soundness and typical defects

4.2.1.1. Logo test parts

Castings produced employing DSP sustained some surface imperfections and occasionally small sections of some features were not reproduced (Figure 4.3.a). The micrographs showed that some ceramic particles were trapped on the metal surface of LM25 and ZA12 parts (Figure 4.3.b) which affected significantly the reproduction quality of the micro-features (Figures 4.3.c and 4.3.d). The primary reason for this could have been that the internal mould surfaces were not cleaned sufficiently well from the unsintered ceramic particles. The zirconia ceramic showed much higher resistance to chemical reaction with 316 S16 compared to the conventional phosphate ceramic used at the MEC for casting high temperature alloys. Consequently, the oxidation layer formed on the surfaces of the 316 S16 parts was negligible compared to that formed on the LWP castings (Figure 4.4.a). This simplified the investment removal operation and resulted in a better surface quality of the castings (Figures 4.4.b and 4.4.d). Also, the high resistance of zirconia ceramic to thermal constraints represents a considerable advantage of Fcubic technology over other rapid shell manufacturing processes (Tang et al. 2003; Bernard et al. 2003; Corcione et al. 2006; Bassoli et al. 2007) in its ability to cast high melting point alloys.

None of the DSP castings suffered defects such as flashes or small spherical defects that could have been formed during the embedding and firing phases. However, the molten 316 S16 did not manage to fill completely the smallest cavities of the DSP moulds, preventing the reproduction of the "ing" characters on the Logo test part.

4.2.1.2. Pyramid test parts

Generally, LM25 and ZA12 performed similarly. Considering each alloy, only two Pyramid castings out of five were successfully produced while the others exhibited missing steps at their tip (Figure 4.5). The castings had a rougher surface texture than those produced using LWP,

which considerably affected the sharpness of the smaller features. The important proportion of Pyramid castings with missing tips could be the consequence of:

- A difference in the air permeability of the zirconia shells compared to that of the gypsum-bonded silica investment that could have affected the effectiveness of the flask air evacuation under casting conditions.
- A difference in the wetting properties of the molten alloy when poured inside the gypsum-bonded silica investment and the zirconia ceramic shell. Any change in the macroscopic contact angle at the solid/liquid/gas interface would affect the mould filling into micro-cavities.
- Obstruction of the smallest cavity of some shells due to improper cleaning from unsintered particles and/or manufacturing inconsistencies occurring when building intricate features in the micrometre range.

Studying the failed samples, it could be seen that the molten alloy occasionally agglomerated with the mould material, creating a coarse metallic surface structure that surrounded the Pyramid (Figure 4.6.a and 4.6.b). Figure 4.7 shows cross section pictures of that coarse structure enveloping the Pyramid of figure 4.6.b. As can be seen, the molten alloy penetrated as far as 2 mm deep inside the shell before solidifying. This phenomenon may be explained as follows: the accurate deposition of the catalyst is primordial in enhancing the diffusion of atoms between adjacent particles during sintering. Therefore, occasional printing errors/inaccuracies during shell building may consequently result in an improper necking between zirconia particles during sintering. Then, at the casting stage, this local lack of bonding between the particles of the shell, together with the influence of the vacuum/overpressure conditions, may allow the molten alloy to penetrate into it, thus creating the observed coarse structure.

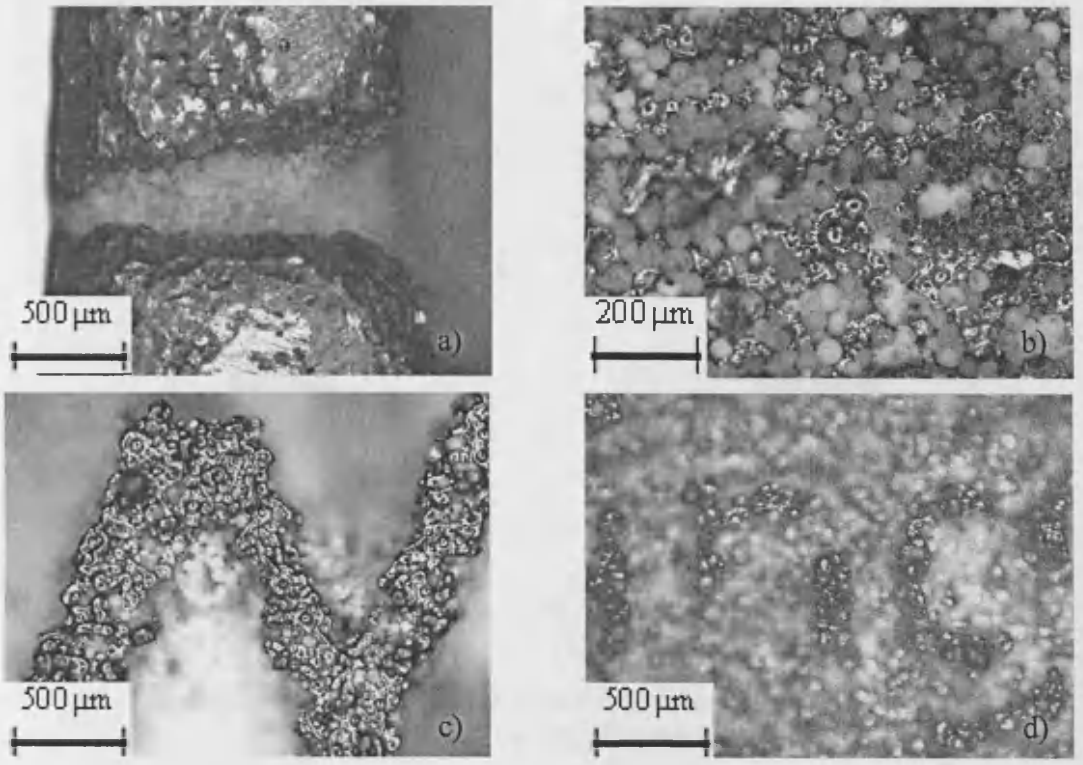

Figure 4.3. LM25 Logo castings form the DSP:
a) Missing section; b) Trapped ceramic particles. c) "M"; d) "ing".

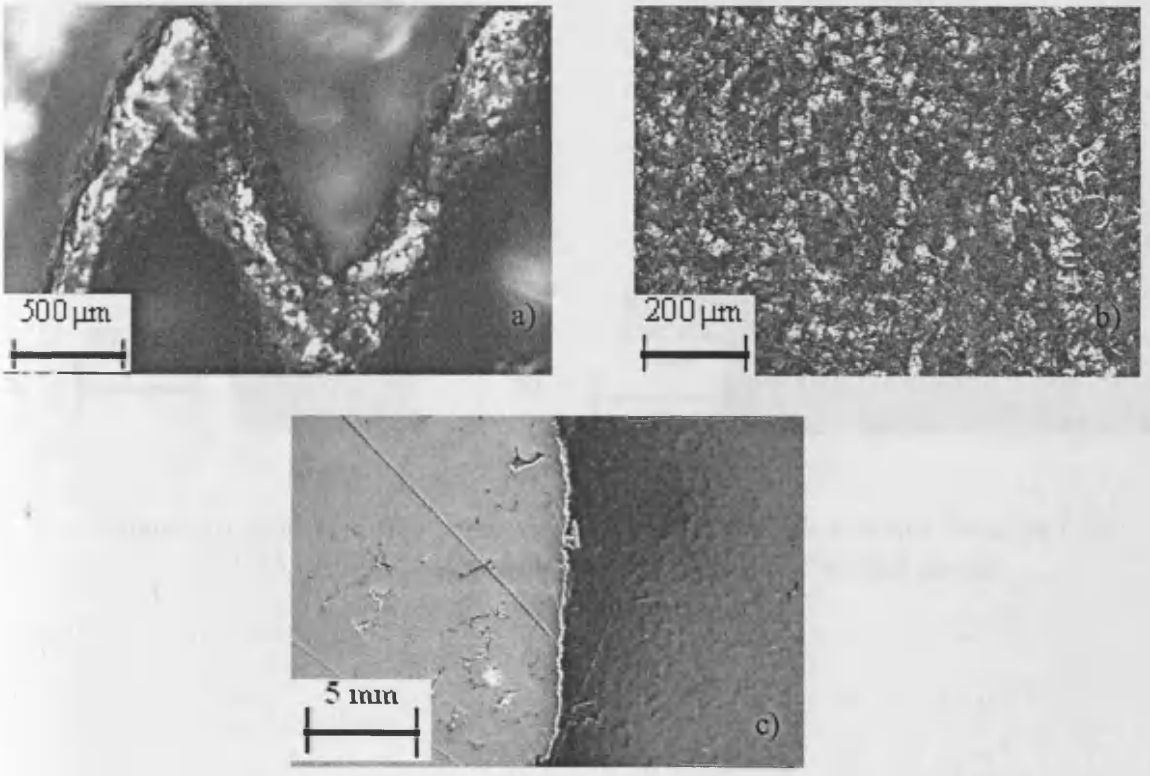

Figure 4.4. 316 S16 results using the DSP:
a) "M"; b) surface finish: c) cross section.

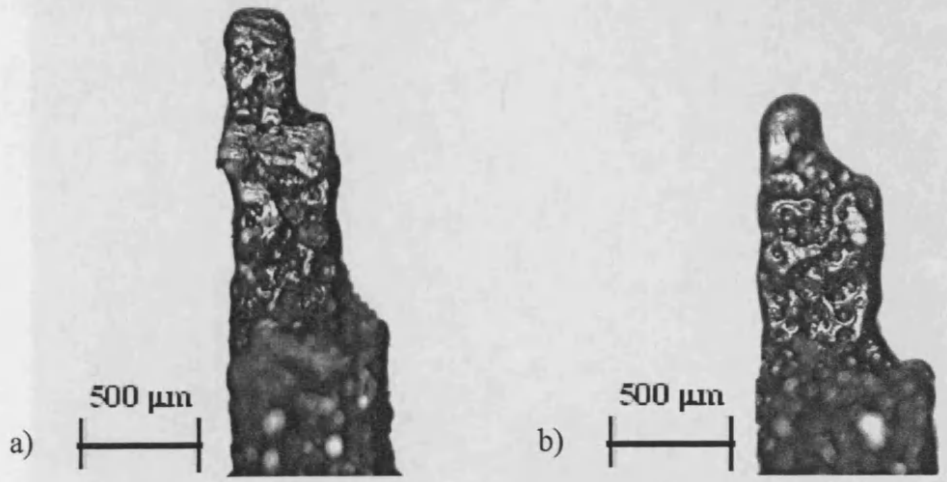

Figure 4.5. LM25 Pyramid castings employing the DSP:
(a) successful casting; (b) missing tip.

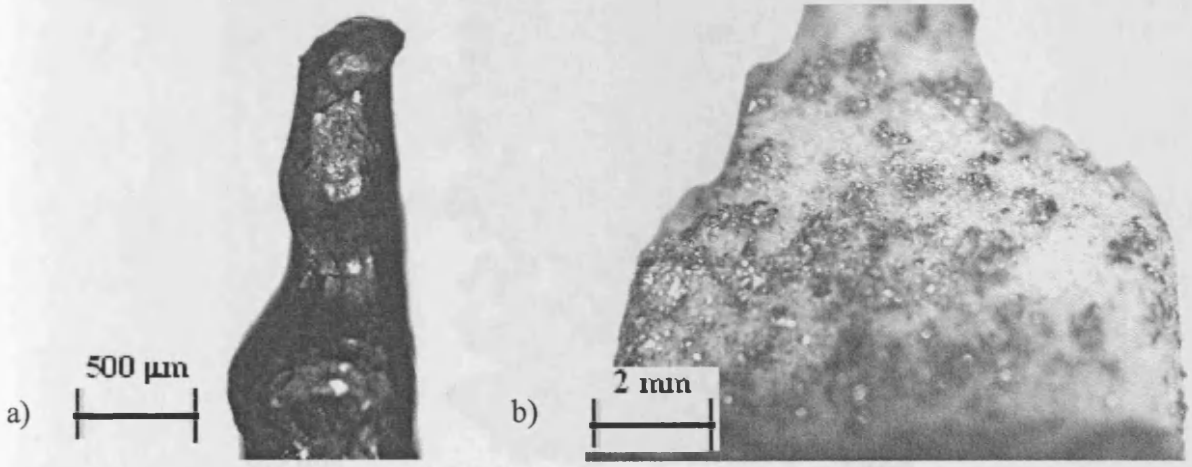

Figure 4.6. Coarse structure enveloping some Pyramids castings from the DSP:
a) ZA12 Pyramid tip after blasting; b) ZA12 Pyramid as-cast.

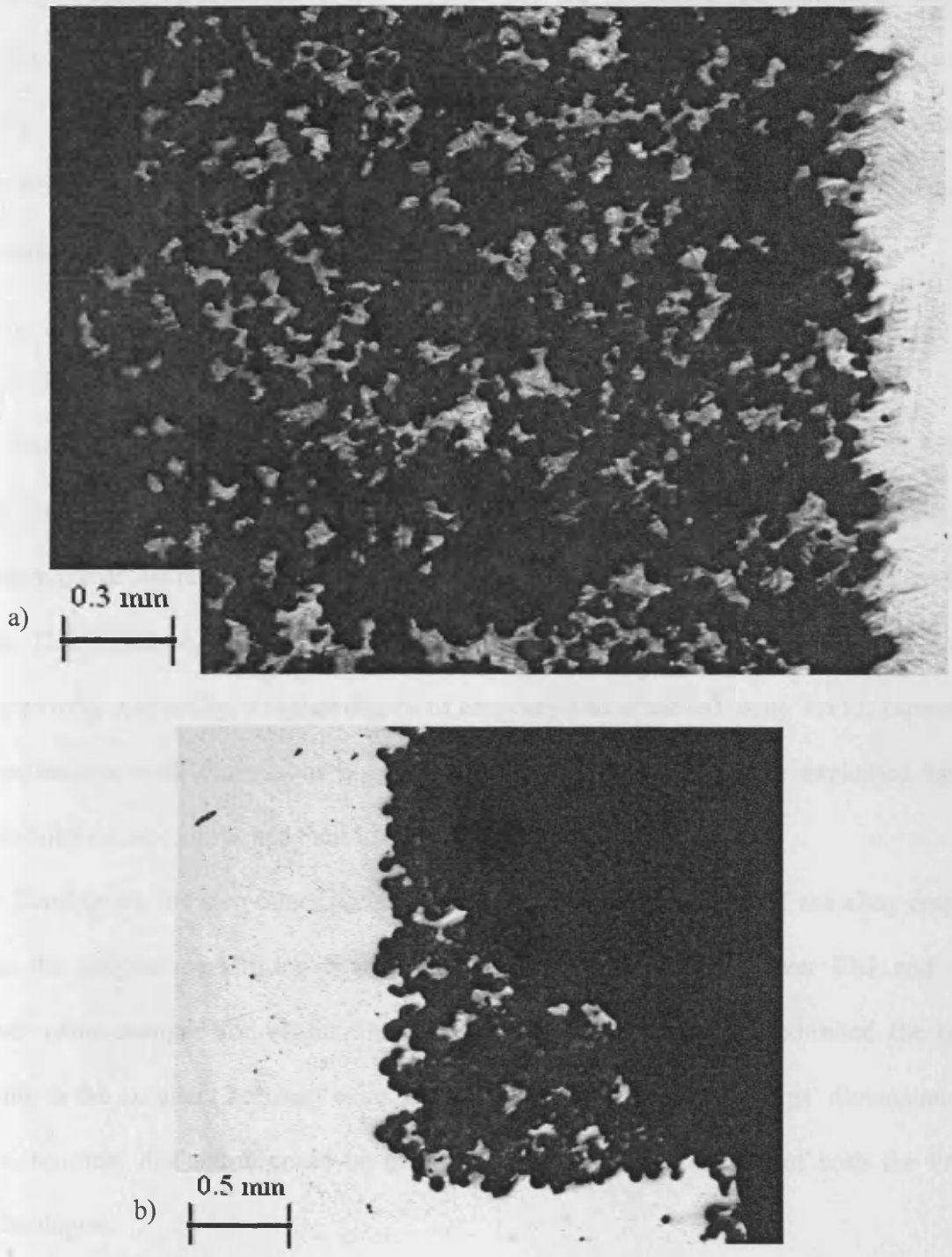

Figure 4.7. Cross sections of a ZA12 Pyramid showing the alloy penetration inside the DSP's shell: a) Back of the Pyramid; b) Junction between two steps.

From these observations it was obvious that the vacuum effect was sufficient enough to overcome capillary forces by sucking the molten alloy through the ceramic particles. Therefore, it was unlikely that the missing tips observed on some samples originated from a difference in the wetting properties of the molten alloy between the gypsum-bonded silica investment and the zirconia ceramic shells.

4.2.2. Accuracy of position: linear dimensional accuracy

The accuracy of the DSP was similar to that of the ThJ process chain, with deviations within ±50 μm (Figure 4.8). Resembling the results obtained for the LWP chains, the maximum percentage of deviation from the nominal dimension was obtained for the smaller step of 150 μm. This percentage of deviation was approximately 13% and 25% for ZA12 and LM25 respectively. Generally, a higher degree of accuracy was achieved using ZA12, especially for the steps/features with dimensions bigger than 340 μm, which could be explained by the better castability of zinc alloys and their lower solidification shrinkage.

Considering the step dimensional range 0.15-0.5 mm, regardless of the alloy employed, PM was the process performing best, exhibiting a higher accuracy over ThJ and DSP. This observation changed for bigger dimensions, for which DSP often exhibited the best results, owing to the excellent accuracy of its ZA12 Pyramids' castings. For steps' dimensions above 0.5 mm, no clear distinction could be made between the achievements of both the PM and ThJ technologies.

Considering now the consistency of each process, PM was clearly the most consistent among the three investigated processes, especially regarding the dimensional range 0.15-1.70 mm. The significantly better consistency of PM over the other two processes might be explained by the high accuracy and good consistency achieved at the pattern building stage. This building advantage was considerably reduced when increasing the step dimension above 1.70 mm. This

could be attributable to the accuracy loss due to metal shrinkage during solidification of the Pyramids' biggest steps, which resulted in a statistically significant change between the linear dimension measured at the pattern and casting stages (see Chapter 3).

4.2.3. Accuracy of form

4.2.3.1. Relative Angular Deviation

As shown in figure 4.9, the angular deviations of the Fcubic samples were more scattered compared to that of the ThJ and PM process chains (Figures 3.18; 3.19; 3.20 and 3.21), exhibiting higher RAD values and variability, particularly when considering RAD associated with steps smaller than 0.5 mm. However, the DSP Pyramid castings did not suffer strong degradation of the RAD at their biggest step of 3.83 mm. This could be explained by the fact that the DSP shells did not suffer from shape distortion due to heterogeneous material shrinkage during sintering as well as manufacturing problems with the two other RP processes. Regardless of the alloy employed, PM led to the production of castings being both more accurate and consistent over the other two investigated technologies, ThJ and DSP respectively. However, even though PM generally performed best, the repeatability of the ThJ technology was closer to, sometimes overtaking that of PM. In any case, the consistency of the PM was superior to that of the DSP.

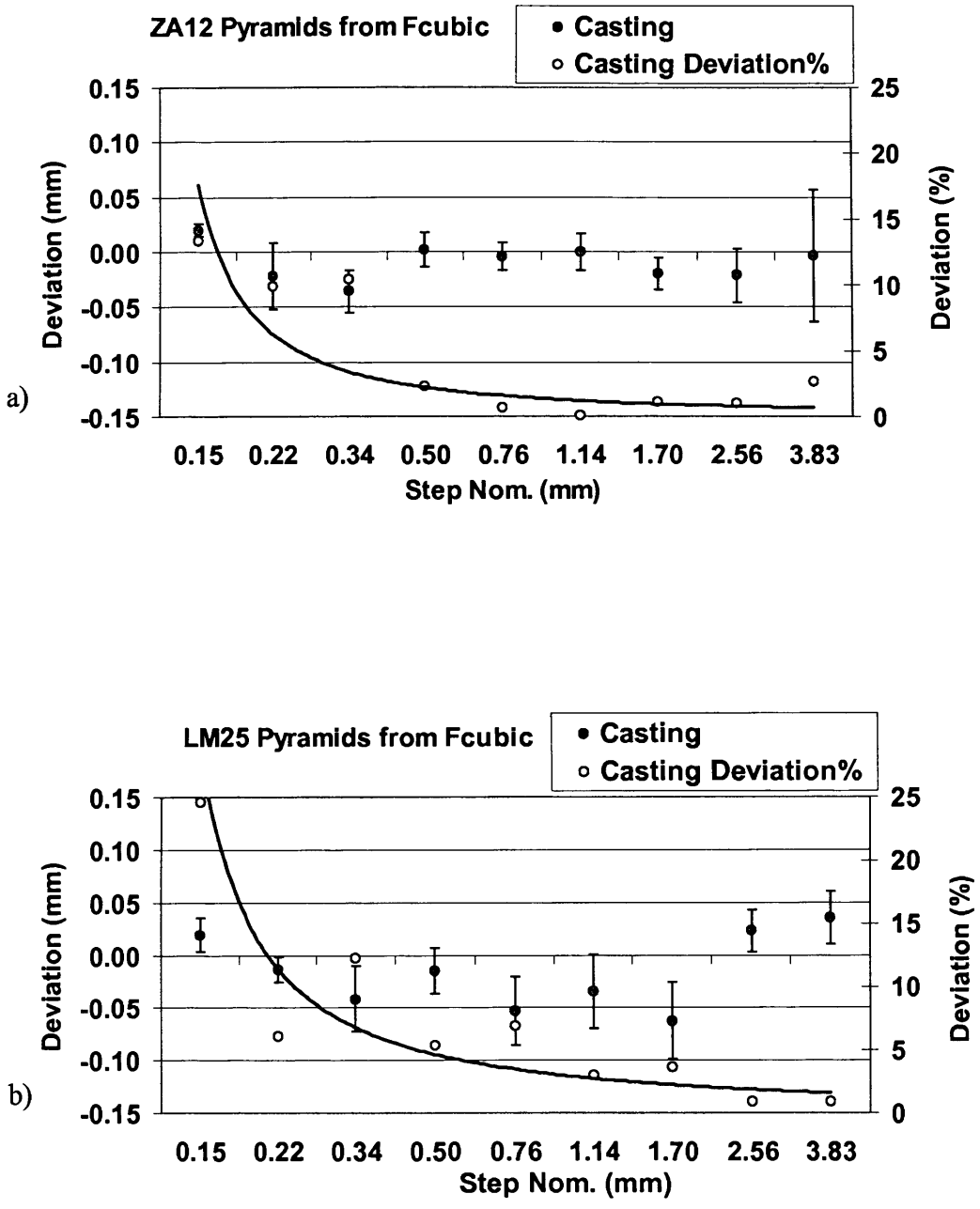

Figure 4.8. Deviation of DSP's Pyramid castings from the CAD nominal dimensions: a) ZA12; b) LM25.

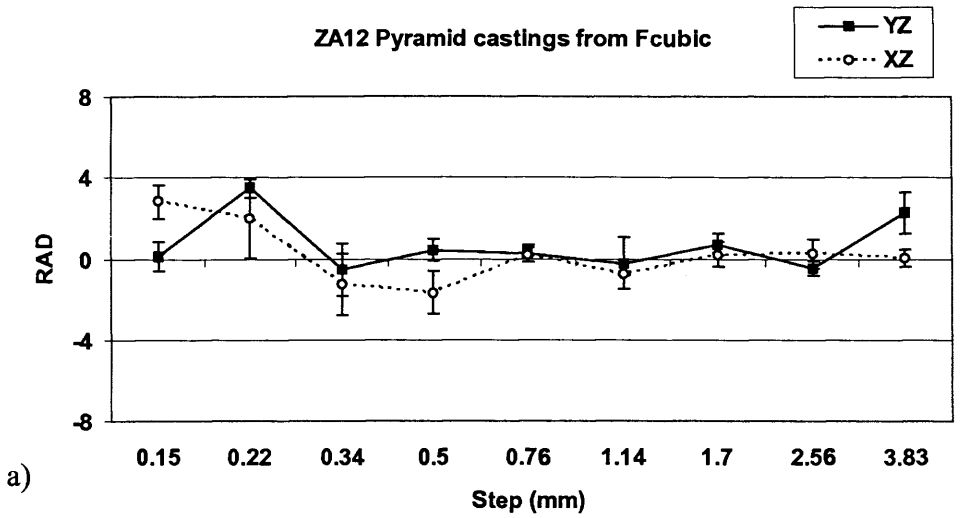

a)

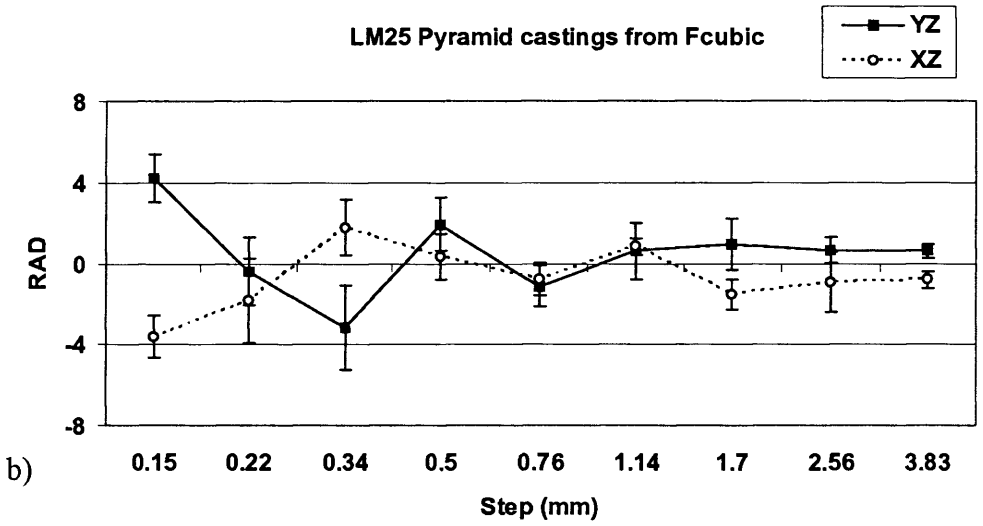

b)

Figure 4.9. RAD of Pyramid castings from DSP:
a) ZA12; b) LM25.

4.2.3.2. Edge Straightness

Analysing the graphs of figure 4.10, it appeared that regardless of the alloy employed, the edge straightness of the DSP castings deteriorated with an increase of the step size, rising from 20 μm at the Pyramid's tip (E1) to about 55 μm at the edge E5. The main contrast with the observations taken in the case of LWP was that the edge straightness of the DSP castings remained constant between E5-E10, with straightness values falling in the range 45 μm to 65 μm. Here again the analysis of the PI charts correlated with the observed phenomenon.

Generally, the LWP chains exhibited close performances, PM being slightly more accurate for edges associated with small dimensions (E1-E3). The important drop in the accuracy of PM for the edge E10 was again attributable to the layer milling problems faced during the building of the PM lost samples (See Chapter 3). Regarding edges associated with the Pyramids' smallest dimensions, e.g. E1-E4, DSP produced castings having straightness values similar to those obtained using LWP. Unfortunately, the matching accuracy of the DSP with the LWP processes ceased for edges above E4. Since it has been demonstrated in Chapter 3 that the solidification shrinkage did not affect the edge straightness of the Pyramids in their pre- and post-casting states, there was little chance that the deterioration of the DSP castings' edge straightness could correlate with the more pronounced linear shrinkage occurring on the Pyramids' biggest steps. Therefore, this deterioration might be solely explained by a lack of process consistency together with the use of a relatively coarse ceramic powder. However, these effects could have been studied better if all castings produced using DSP had been successful.

From a consistency point of view, no strong distinction could be made between the three investigated processes.

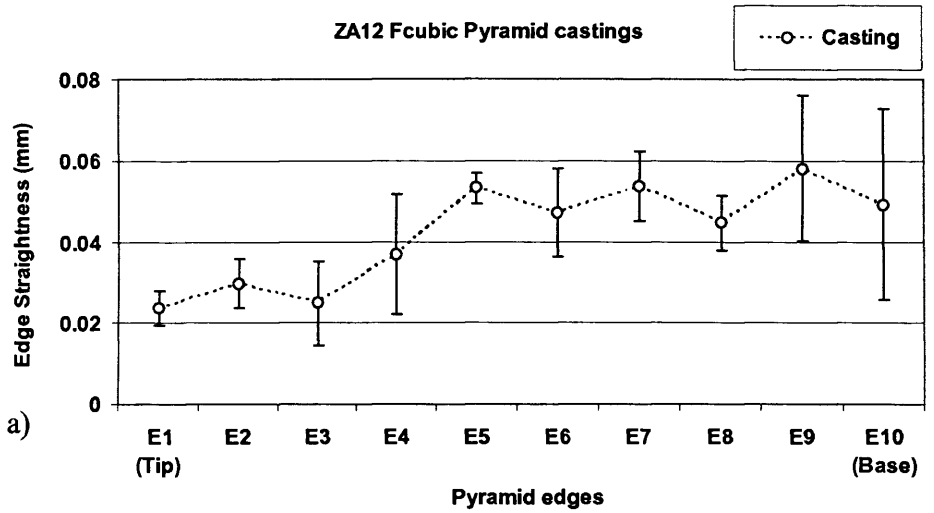

a)

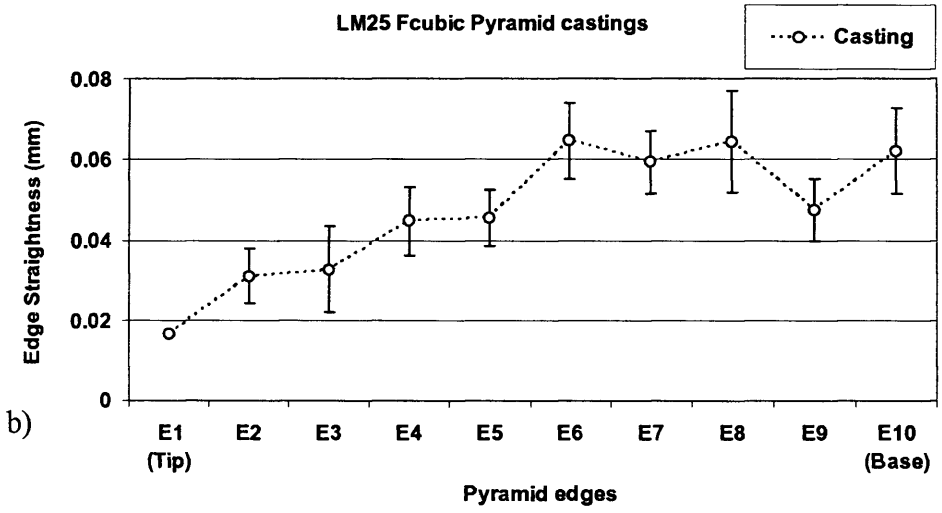

b)

Figure 4.10. ES of the DSP's Pyramid castings:
a) ZA12; b) LM25.

4.2.4. Surface finish

The surface quality of the Pyramid castings was assessed through roughness measurements performed on the pyramid castings as processed using the Mitutoyo SJ-400 tester with standard stylus. Following the Mitutoyo standard procedure, roughness measurements were taken on different pre-selected surfaces along directions parallel to the main building axis X, Y and Z of the RP machine (Figure 4.11). In order to provide more information about the surface texture variability of each sample, the results displayed two parameters, Ra and Rz (ISO/JIS), both expressed in micrometres. Since the Ra calculation neutralizes the few outlying points so that extreme values have no significant impact on the final results, it is an effective method for monitoring surface texture and ensuring consistency in measurement of multiple surfaces. On the other hand, extreme points have a much greater influence on the final value of the Rz measurement, providing additional information on the surface texture variability of each sample. Below is the definition of both parameters provided by the Mitutoyo's roughness tester SJ 400 technical handbook:

- Ra represents the arithmetic mean of the departures of the roughness profile from the mean line within the evaluation length.
- Rz ten points height, is the average height difference between the five highest peaks and the five lowest valleys within the evaluation length.

Figure 4.12 shows the results from the roughness measurements performed on the castings produced using the three studied process chains. From a general stand point, it can be seen that the plots of Ra and Rz follow identical trends depending on the measurement location and direction. Regardless of the measurement direction, ThJ exhibited the smallest average roughness followed by PM and finally DSP with Ra values of 2, 2.8 and 5.5 μm respectively.

The LWP process chains generally produced castings having a higher roughness along the Z direction in the XZ and YZ planes, which was the consequence of the layer effect associated with

the ThJ and PM RP technologies used to build the patterns (Figure 4.13). It should be noted that in the case of PM, a layer thickness of 38 μm was selected for building the patterns in order to reduce the build time and make it closer to that of ThJ. This was at the expense of the increased layer effect in the Z direction and explained why PM exhibited high roughness values along Z similar to that measured with DSP. Also, the measurements carried out in the XY plane (Top) on castings produced using LWP revealed a smoother surface finish, particularly in case of PM. This observation was the consequence of the surfacing operation performed after each layer deposition by the cutter available on the PM machine. Another interesting observation was that the surface finish of the LM25 castings was generally slightly better than that achieved on the ZA12 ones. This could be explained by the better fluidity of ZA12 compared to LM25, thus copying more closely the internal mould surfaces at the expense of the roughness (Figures 4.14.a and 4.14.b).

Although DSP produced samples having the highest average roughness, it did not suffer strong measurement variability caused by the surface texture anisotropy introduced at the pattern building stage by the PM and ThJ technologies. Instead, it seemed that the size of the ceramic particles employed to produce the shells was the main factor responsible for the higher roughness measured on the DSP castings. Thus, the implementation of a finer-scaled ceramic powder would drastically reduce this roughness to a value similar to that achieved by the LWP chains.

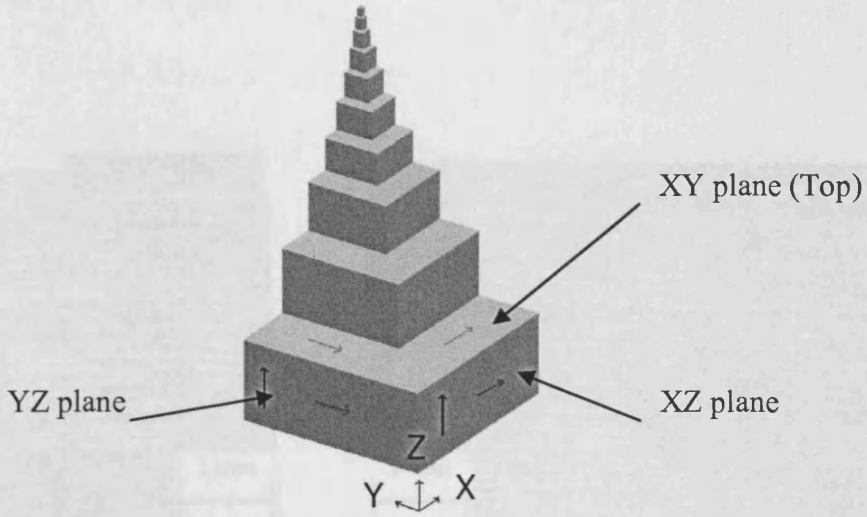

Figure 4.11. Roughness measurement directions.

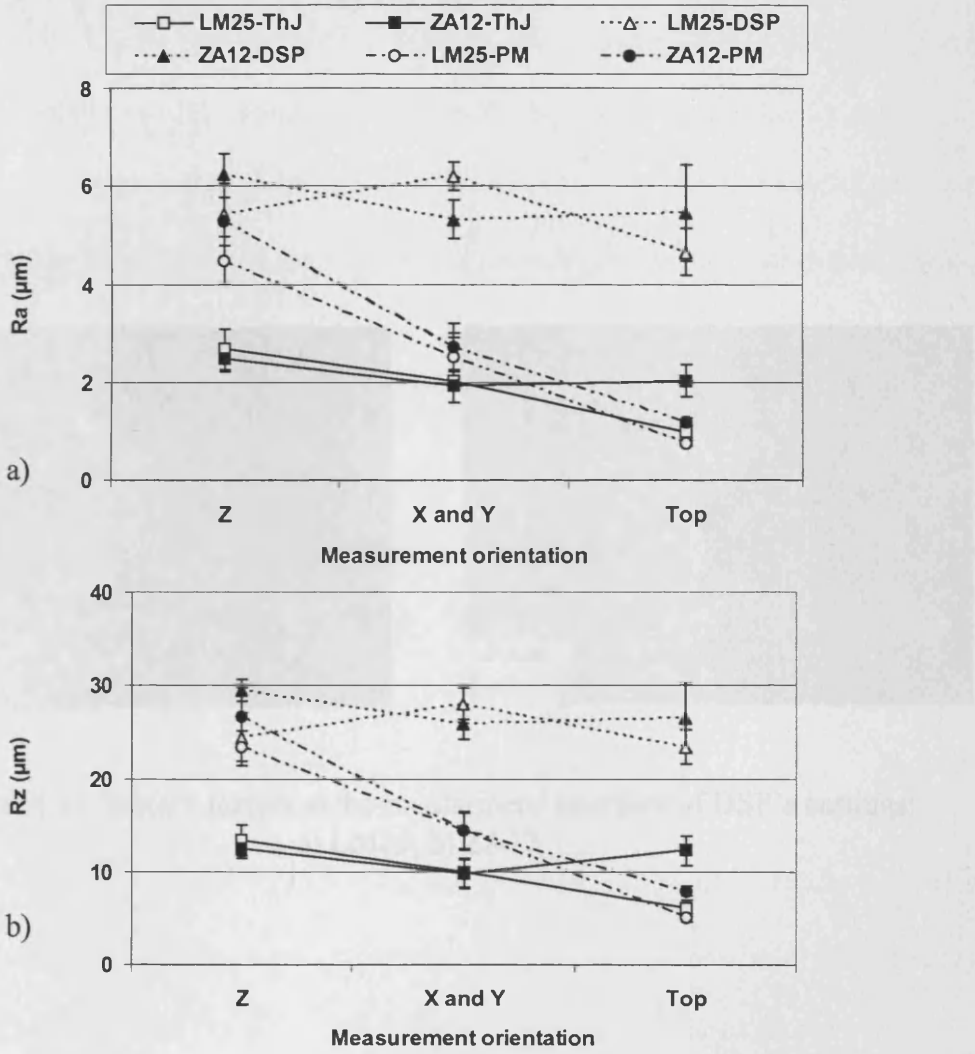

Figure 4.12. Roughness of the Pyramid castings from each technology:
a) Ra; b) Rz.

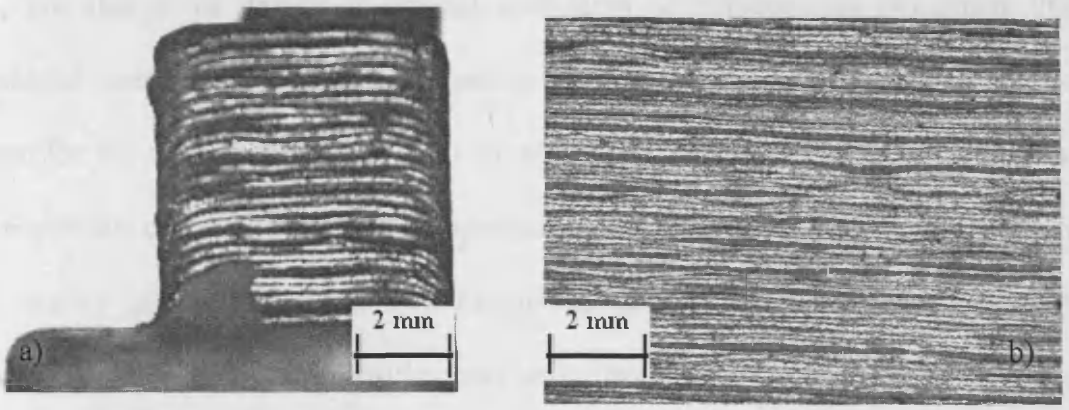

Figure 4.13. Stair-step effect on the surface of LM25 Pyramid castings:
a) ThJ; b) PM.

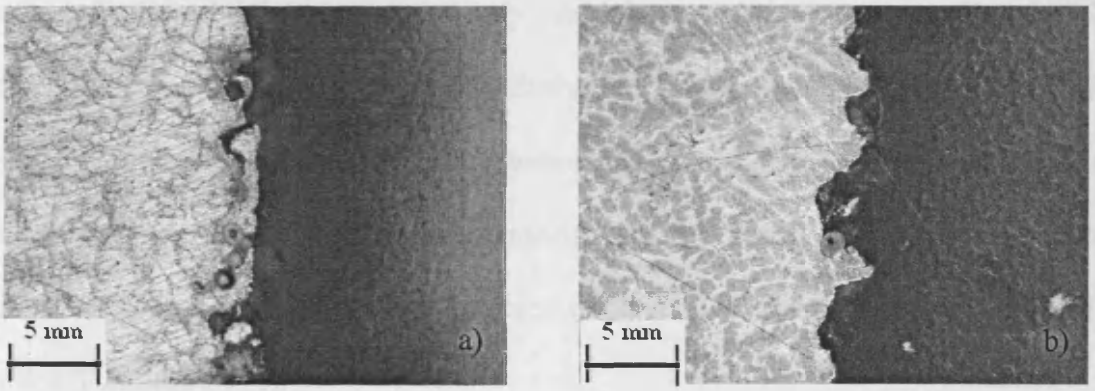

Figure 4.14. Surface texture at the mould/metal interface of DSP's castings:
a) LM25; b) ZA12.

4.3. Porosity

The production of a sound casting does not only refer to its dimensional accuracy and surface finish, but also to its degree of internal soundness or homogeneity (Kaufman, 2004). The presence of casting defects such as porosities is almost inevitable in practice and is a major concern for the foundrymen since their number, size and distribution can exert an adverse influence on the castings' mechanical properties, especially ductility (Beeley 1972). Porosities in metal casting generally fall into two categories; gas-based and shrinkage-based porosities (Flemings 1974). Gas-based porosities may arise from: gases already present in the melt; a significant change in gas solubility between the liquid and solid state; gas entrapped in the liquid during pouring and finally, from a possible mould/metal reaction. Shrinkage-based porosities on the other hand result from the metal contraction during freezing. Adequate gating is a prime factor in reducing major shrinkage defects since it ensures complete feeding of the casting by a steady influx of liquid to compensate for liquid and solidification contraction. However, the formation of micro-shrinkage porosities only visible on a polished surface still occurs in inter-granular or inter-dendritic regions, particularly for alloys freezing over a relatively wide temperature range (Flemings 1974). The formation of a mushy zone during solidification of these alloys confines the fluid flow to interdendritic regions, limiting its ability to compensate solidification contraction. Therefore, resistance to fluid flow is an important source of micro-porosities (Flemings 1974).

Thus, in order to provide additional information on the soundness of the castings produced using the LWP and DSP technologies, a quantitative analysis relating the amount of apparent porosity observed on polished surfaces of some Pyramid castings was performed. Since the type of porosity identifiable in castings may vary significantly depending on their location, measurements were taken both in the vicinity of the mould/metal interface and in the core of the castings. Four groups of Pyramid castings, two per alloy and technology, were randomly selected

among the set of castings. The Pyramids were placed in a rubber mould as illustrated in figure 4.15.a and cast into acrylic resin. After demoulding, the samples were cross sectioned as illustrated in figure 4.15.b. Both surfaces of the Pyramids (Figure 4.15.c) were worn down by approximately 200 μm using a lapping machine combining lubricant and polishing slurry, containing calibrated diamond particles of 3 μm. The samples were finally manually polished with a 1μm diamond polishing slurry and analysed using image analysis software called Omnimet (www.buehler.com). The polished surfaces were entirely scanned by the operator and the observed apparent porosities were both counted and measured, the latter being based on their equivalent surface area. The porosities were then classified per size and the average cumulative count per group displayed in tables 4.1 and 4.2.

Let us consider first the quantity of apparent porosities in the vicinity of the mould/metal interface. Generally, LM25 castings exhibited approximately twice as many micro-porosities as the ZA12 ones. For all castings, porosities were homogeneously spread over the observed surface. Comparing the results obtained between the LWP and the DSP technologies, it appeared that, regardless of their size, the total count of micro-porosities observed on the DSP castings was reduced by 38% and 41% to that of LWP, for LM25 and ZA12 respectively. The general trend for both technologies and alloys was that the smallest porosities in the range of 20 to 500 μm^2 represented the majority of those measured. Only the DSP Pyramid produced in ZA12 exhibited two porosities having an equivalent surface area greater than 5000 μm^2. These observations could be the consequence of both a lower reactivity of the Zirconia ceramic shell with the molten alloy and a higher permeability of DSP moulds, allowing a faster and better evacuation of trapped bubbles from the casting after pouring. This result would offer a considerable advantage to DSP if post-processing operations, such as surface finish machining, had to be performed on the castings.

Looking now at the measurements performed in the core of the Pyramid castings, we can see that no clear distinction between each technological chain can be observed regarding a specific alloy. The quantity of porosities measured in the range of 20 to 500 μm^2 for the ZA12 castings was considerably lower compared to those observed close to the mould/metal interface, a difference of 81% and 70% for LWP and DSP respectively. Similar observations for the LM25 castings could be made considering the same dimensional range, 20 to 500 μm^2, but in more reasonable proportions, with a difference of 60% and 28% for LWP and DSP respectively. The other important difference between micro-porosities measured in the casting core and near the surface of LM25 castings was related to their size and number. If fewer porosities were counted in the casting core, they were on average much bigger. In total, thirteen micro-porosities having an equivalent surface area between 5E3 and 11E4 μm^2 were counted for both DSP and LWP. A logical explanation might be that the more important micro-porosities observed in the casting core were shrinkage-based porosities. ZA12 castings did not behave in the same way, with all porosities measured in the casting core having their equivalent surface area less than 50E2 μm^2. The difference between LM25 and ZA12 castings may arise from the lower solidification contraction of zinc during cooling compared to aluminium.

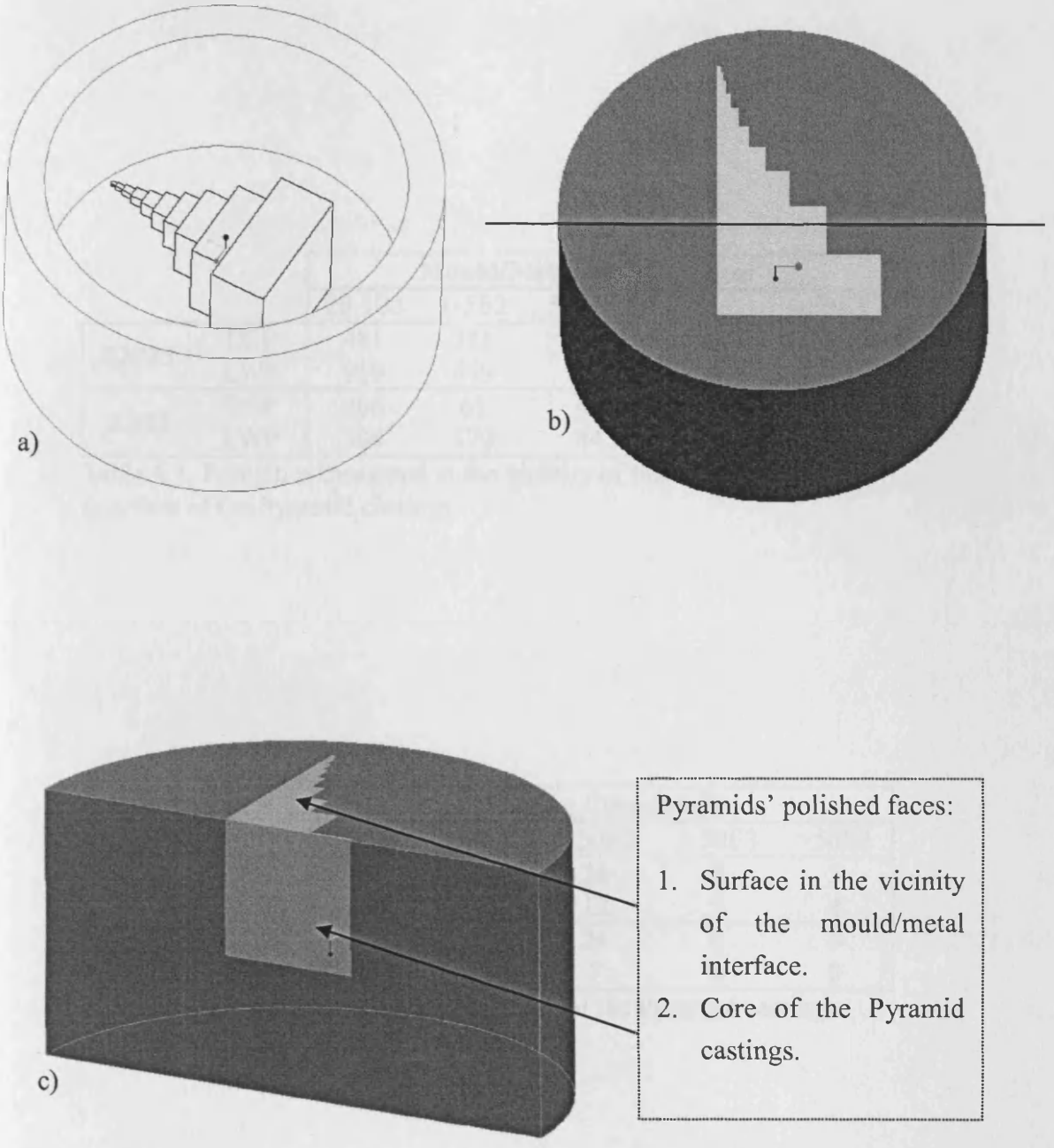

Figure 4.15. Pyramids' porosity analysis:
a) Pyramid positioning in the rubber mould;
b) Pyramid embedded in acrylic resin after demoulding showing the location of the cross-section;
c) Cross-section of the sample highlighting the observed faces.

		Mould/Metal interface (μm^2)				
		20-100	1-5E2	5-50E2	5-50E3	>50E3
LM25	DSP	481	381	77	0	0
	LWP	959	479	87	0	0
ZA12	DSP	206	61	42	2	0
	LWP	304	179	44	0	0

Table 4.1. Porosities measured at the vicinity of the Mould/Metal interface of the Pyramid castings.

		Casting Core (μm^2)				
		20-100	1-5E2	5-50E2	5-50E3	>50E3
LM25	DSP	540	109	26	8	5
	LWP	466	126	12	9	4
ZA12	DSP	31	38	24	0	0
	LWP	38	57	7	0	0

Table 4.2. Porosities measured in the core of the Pyramid castings.

4.4. Production Labour and Costs

If comparing the technological capabilities of different manufacturing processes is of considerable interest from an engineering stand point (Dimitrov et al. 2006), assessing their relative economical viability is a major factor from a commercial point of view. Therefore, benchmarking also needs to account for the relative performance of the investigated process chains in terms of both production time and costs (Hopkinson and Dickens 2001). Table 4.3 lists all the operations included in the investigated two process chains, together with their estimated time and relative costs for producing Logo castings using both VIC for the non-ferrous alloys and CIC for 316 S16. Since production costs may vary between foundries, it was necessary to calculate the castings' production costs relative to a reference cost. It was, therefore, decided to use the cost for producing one Logo pattern using the LWP in our laboratory as one cost unit, assuming that the production cost for a Logo pattern was identical both for the ThJ and PM technologies.

Interpreting the results of table 4.3, it appeared that the production of castings employing DSP was 22% faster than with LWP because the time required for sintering the moulds was shorter than the time necessary for firing the patterns in casting clusters. It should be noted that the shell building operation for DSP was almost nine times that of the pattern building for LWP. This significant difference was due to the relatively important size of the shells, which featured cavities both for the Logo and Pyramids test parts. The production of individual shells per design would have then increased further the leading time advantage of DSP over LWP. Nevertheless, the castings produced employing DSP were 37% and 23% more expensive for VIC and CIC respectively, owing to the important costs associated with the building of the shells.

	Time (hours)				Cost of materials, energy, labour			
	LWP		DSP		LWP		DSP	
	VIC	CIC	VIC	CIC	VIC	CIC	VIC	CIC
File preparation	0.1	0.1	0.5	0.5	0.02	0.02	0.12	0.12
Build preparation	0.5	0.5	0.5	0.5	0.12	0.12	0.12	0.12
Building patterns/shells	1.2	1.2	9	9	1	1	4	4
Cleaning & infiltration/curing	1	1	4	4	0.24	0.24	1	1
Tree & flask preparation	1	1	0.3	0.3	0.24	0.24	0.08	0.08
Embedding in vacuum	1	1	0	0	0.75	0.75	0	0
Firing and flask preheating	18	18	3	4	0.54	0.54	0.12	0.16
Casting	1	2	1	2	0.24	0.48	0.24	0.48
Break out of the ceramic mould	0.5	0.2	0.2	0.2	0.12	0.05	0.05	0.05
Degating & finishing	2	4.5	2	2	0.48	1.1	0.24	0.24
Total	26.3	29.5	20.5	22.5	3.75	4.54	5.97	6.25
Relative Percentage	**78**	**69**	**100**	**91**	**100**	**83**	**63**	**60**

Table 4.3. Relative production costs and time for both technological chains.

4.5. Summary

This chapter reports the results of a benchmarking study for the production of meso/micro castings between the conventional LWP and the Fcubic DSP technology. The main conclusions from this case study are:

- DSP castings produced from the non-ferrous alloys showed a considerable amount of trapped zirconia particles on their surfaces. Also, some of the DSP castings exhibited problems such as missing sections of thin ribs and incomplete reproduction of the smallest step of Pyramid castings. These problems originated most likely from improper cleaning of the unsintered ceramic particles and/or manufacturing inconsistencies occurring at the shell building stage.
- The surface quality of the DSP 316 S16 castings was better than that obtained employing LWP owing to the 316 S16 alloy low reactivity with the zirconia moulds. Similar to LWP, the 316 S16 alloy failed to completely fill the micro-cavities of the zirconia moulds.
- Considering the non-ferrous casting alloys, the micro-replication capabilities of DSP were limited due to the coarse ceramic powder used to build the moulds, together with the considerable amount of trapped particles present at the surface of the castings.
- Regarding features of the Pyramid design associated with dimensions smaller than 1.7 mm, PM was found to be generally speaking the most accurate and consistent technology both in terms of accuracy of position and form, followed by ThJ and finally DSP. However, DSP exhibited similar results to those of the other two processes when considering features associated with the Pyramids' biggest dimensions. This was most likely due to the fact that the DSP technology did not suffer shape distortion problems arising from heterogeneous material shrinkage during the shell manufacturing process.

- The surface roughness of the DSP castings was the most consistent over all studied technologies but suffered from the coarse powder used for the manufacture of the shells.
- DSP castings exhibited a significantly reduced quantity of micro-porosities at the mould/metal interface, owing to the lower reaction between the mould and the molten alloy and possibly because of a faster and better evacuation of trapped gases into the casting after pouring.
- The lead-time of DSP was about 22% shorter than that of the conventional LWP. However, the material, energy, and labour costs were 37% higher.

These conclusions make the Fcubic-DSP technology an interesting alternative for rapid prototyping and the short-run manufacture of metallic parts. It should be noted that DSP is a new process with potential for improvement. The optimization of the mould making process together with the introduction of finer powders could reduce significantly production time and cost and enhance the replication capabilities of micro-features.

CHAPTER 5: Modelling the evolution of the Dendrite Cell Size of cast micro-features as a function of their Aspect Ratio and processing parameters using LM25

It has been demonstrated in the previous chapters that applying RP techniques for producing accurate sacrificial patterns or casting moulds through direct shell processes was quite promising for casting sound meso/micro metallic components within close dimensional tolerances. However, our knowledge is still limited in regards to how the extreme cooling-down conditions associated with this technology when casting features in the micrometre range affect their microstructure and consequently the mechanical properties of the cast components. The importance of answering these questions arises from the emergence of new application areas, e.g. the use of aluminium (Al-Si-Mg) casting alloys in microelectronics cooling devices, polymer replication micro-tools for micro-fluidic applications, mechanical parts such as micro-gearboxes, etc...(Chapter 2). Since the homogeneity and morphology of the castings' crystallographic structure have a direct influence upon their thermal conductivity and mechanical properties, it is important to obtain information on the as-cast microstructure of micro-components in order to enhance their functionality.

Before going further, and in order to explain the necessity of this research, it is interesting to briefly summarize some of the work which has been previously done on Al-Si-Mg casting alloys. It is well known that increasing the cooling rate of castings and consequently the degree of undercooling achieved during solidification, affects the nucleation process and favours the production of superior quality castings through a refinement of their metallographic structure (Flemings 1974). As reported in Chapter 2, the family of Al-based casting alloys is widely used in the foundry industry because of good castability, advantageous weight to strength ratio and suitability for post-processing heat treatment. Studying the microstructure of unmodified aluminium casting alloys, particularly the

morphology of their as-cast dendritic structure, is of considerable practical interest in production casting, since it has been demonstrated over the years that the size of their dendritic structure is directly linked to the rate of solidification achieved during casting according to the following equation from (Spear and Gardner 1963; Cáceres and Wang 1996; Wang at al 2001):

$$\lambda = C \cdot R^{\phi} \qquad (5.1)$$

where: λ - Dendrite cell size (DCS) in [μm]; R (K/s) - solidification rate; C and ϕ - constants. These researchers also demonstrated that a decrease in DCS led to an increase of the tensile ductility of the castings.

In this chapter, an experimental study was conducted to investigate the degree of dendrite refinement when producing micro components using LM25 casting alloy. An empirical model is proposed to describe the evolution of DCS in walls with different thicknesses in the micrometre range as a function of their aspect ratio (AR) for a given alloy, mould material and processing parameters. Additionally, the study reports the morphological changes occurring on the eutectic Si particles, intermetallic compounds and micro-porosities when increasing the micro-features' AR. Finally, an attempt was made to find a relationship between the observed structural refinement in the cast micro-features and their respective mechanical properties through micro-hardness measurements.

5.1. Experimental designs and settings

In order to assess and compare the changes in the solidification conditions occurring when casting walls with different thicknesses (T) and AR, two sets of experiments were conducted in this study. The first set of trials consisted in casting plates with T of 10, 7, 5 and 2.5 mm and AR of 10. These thicknesses were chosen since they represent typical dimensions of precision castings produced at macro scale using VIC. In order to assume a one dimensional

heat flow transfer problem (Flemings 1974), T of the plates was selected to be at least three times smaller than their widths (W). The feeding was done only from one side of the samples as shown in figure 5.1. The second set of experiments was performed on test parts incorporating micro-thin ribs, having a range of thicknesses of 1, 0.75, 0.5, 0.45, 0.3 and 0.25 mm with a maximum AR of 50 and W/T>>3 (Figure 5.2).

It is recognised that in IC, the degree of undercooling achieved during casting of unmodified alloys is primarily dependent upon the mould temperature, making it the most critical processing parameter influencing the as-cast microstructure of the casting (Flemings 1974). Therefore, the mould temperature (T_M) was set as the variable in our experiments, each set of trials using two different temperatures, respectively 250°C and 450°C. The lower temperature was chosen as the minimum temperature allowing successful reproduction of the micro-ribs, the higher as the highest recommended temperature for the macro-precision casting to be reproduced without significant risk of creating overheating defects such as short cracks (Minev 2003). The alloy pouring temperature was kept at a constant value of 720°C. All test parts produced at a specific mould temperature were achieved in a single casting operation to ensure that the processing parameters were strictly identical.

The lost patterns were produced using ThJ technology. Details about the manufacture of the Rib casting test parts and the technology used for their production has already been provided in Chapter 3. After casting, the test parts were sectioned in half along their length, L, to perform a metallographic analysis of their microstructure (Figure 5.2). To minimise the structural changes in the samples, the bigger test parts were cut using a low feeding rate mechanical saw with lubricant while those having T below 5 mm were cut employing electro-discharged machining (EDM). Samples were then cast into acrylic resin and polished using diamond polishing slurries following the methodology described in Chapter 4.

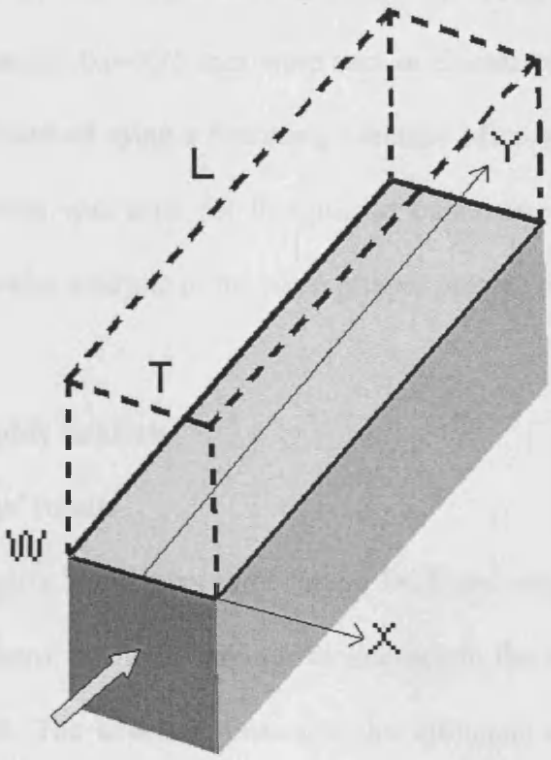

Figure 5.1. Cross-section of a thick casting plate: the metallographic analysis was performed in the plane XY (The thick arrow shows the location of the gating system).

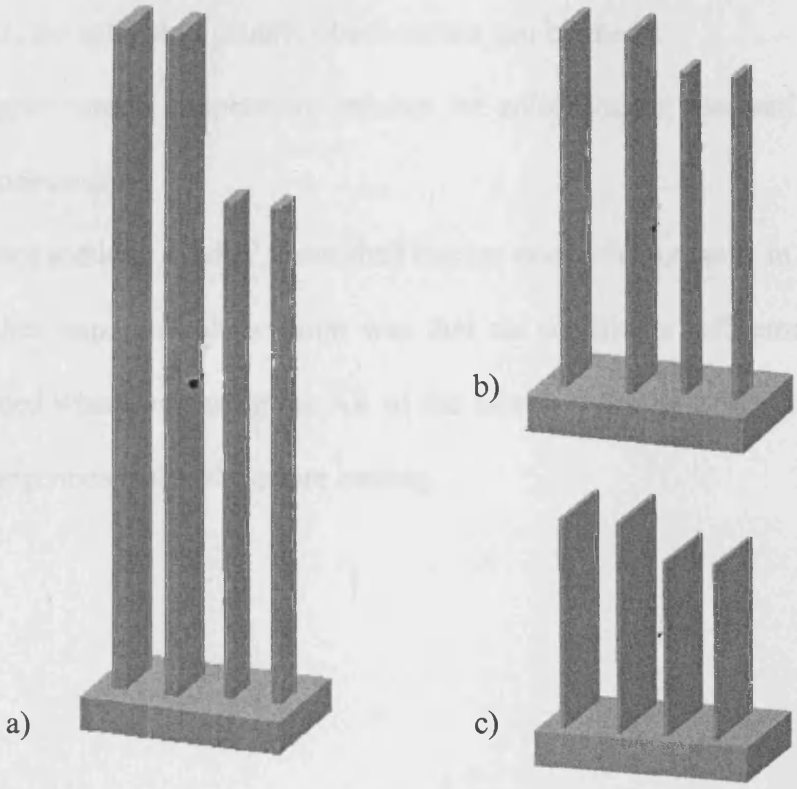

Figure 5.2. Ribs test parts with AR 50:
a) 1mm-0.75mm; b) 0.5mm-0.45mm; c) 0.3mm-0.25mm.

The metallographic analysis was carried out using image analysis software Omnimet. Samples with thicknesses 0.3-0.25 mm were cast in electro conductive copper-filled resin so that they could be observed using a Scanning Electron Microscope (SEM). The XB1540 Carl Zeiss SEM/FIB system was used for imaging at nanometre scale resolution as well as to perform x-ray diffraction analysis of the main phases present on the castings.

5.2. Metallographic analysis

5.2.1. Macro-castings' results

The graphs of figure 5.3 display the average DCS and respective standard deviation (SD) measured on the 'macro' castings, having thicknesses in the range of 10 mm to 2.5 mm as a function of their AR. The analysis illustrates the influence of casting thickness and mould temperature on the as-cast microstructure. This was in agreement with the general solidification theory for castings and ingots produced in insulated moulds (Flemings 1974). In particular, the following generic observations can be made:

- A higher mould temperature reduces the solidification rate and leads to a coarser alloy microstructure;
- Thinner sections solidify faster than thicker ones which results in smaller DCS.

Another important observation was that no significant refinement of the dendritic cells was noticed when increasing the AR of the castings, proving that the degree of undercooling was homogenous inside the entire casting.

a)

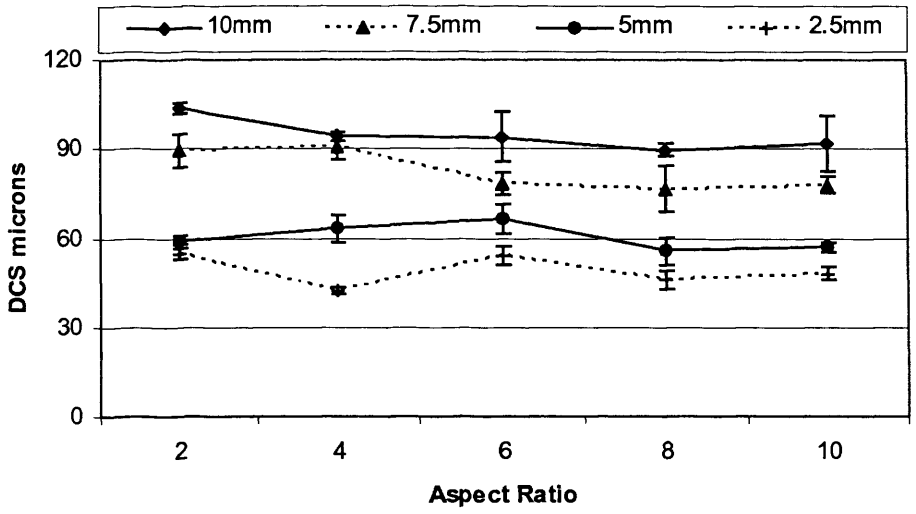

b)

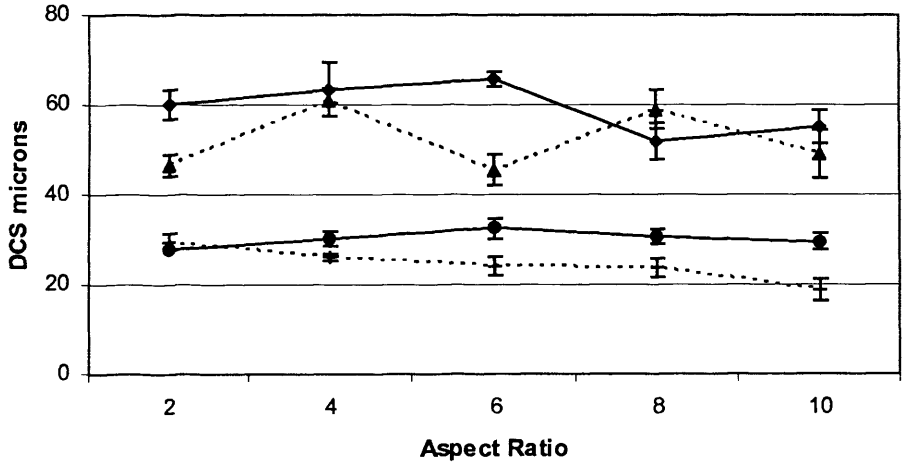

Figure 5.3. Evolution of the DCS on the cast plates with different thicknesses as a function of their AR: a) T_M 450°C; b) T_M 250°C.

5.2.2. Micro-castings' results

5.2.2.1. DCS investigation

The pictures in figure 5.4 together with the graphs of figure 5.5 depict the dependence of DCS refinement in the ribs on AR and T_M. In contrast to the first set of trials the resulting microstructure was strongly dependent on the ribs' AR. It is obvious that when dealing with micro-casting, the solidification rate and corresponding microstructure is AR sensitive. This represented a fundamental difference in the solidification behaviour of castings incorporating meso/micro features which needs further investigation. Classical approaches, therefore, concerning the relationship between the casting microstructure and solidification rate, primarily seen as a function of the thickness solidified, must be re-examined and new models applicable to micro-castings ought to be introduced. The proposed empirical model describing the evolution of the DCS as a function of the ribs' AR and T_M will be presented in §5.5.

Another interesting observation was made of the thin ribs (0.3-0.25 mm) produced with the higher mould temperature of 450°C. It appeared in some cases that a few and relatively coarse primary dendrite arms extended in the ribs up to 5/6 mm away from their base, a corresponding AR of approximately 20 (Figure 5.6). Further across the rib and closer to its tip, a drastic morphological transition of the metallographic structure to very fine grains was observed.

In this case, the influence of the ribs' AR on the micro-castings' microstructure has to be observed in conjunction with the overall heat flow scenario. The thin ribs provide more pronounced directional heat-flow and directional solidification behaviour of the casting. If T_M is high enough (450°C), extended primary dendrite cells' growth may be observed in the root of the thin ribs (Figure 5.6). On the tip of the thin ribs, because of the significant change in the ratio of temperature gradient G to the rate of freezing R (G/R) (Beeley 1972), the structure changes to a more refined and favourable one from the point of view of the castings'

mechanical and thermal properties. If T_M is low enough (250°C), the fast cooling rate predominates as a factor for the structure formation and no directional large dendrite cell growth is observed. That is because a higher degree of undercooling would increase the number of the growing cells which would lead to the interference of the growth process. Thus, an increased number of dendrites of smaller AR and overall size are observed. Such a contrasting morphological picture could not be observed for cast sections of a few millimetres thick due to a less pronounced directional heat flow.

This is an important observation in thin rib meso/micro castings since it proves the importance of the mould temperature as a parameter to be monitored in order to achieve a homogenously refined casting structure with corresponding ductility, strength and thermal conductivity. In other words, the small thickness of the rib-type features should not be regarded as a prerequisite for achieving a fast cooling rate with a corresponding favourable structure. The mould temperature is still as important, if not an even more so, in achieving an appropriate casting structure.

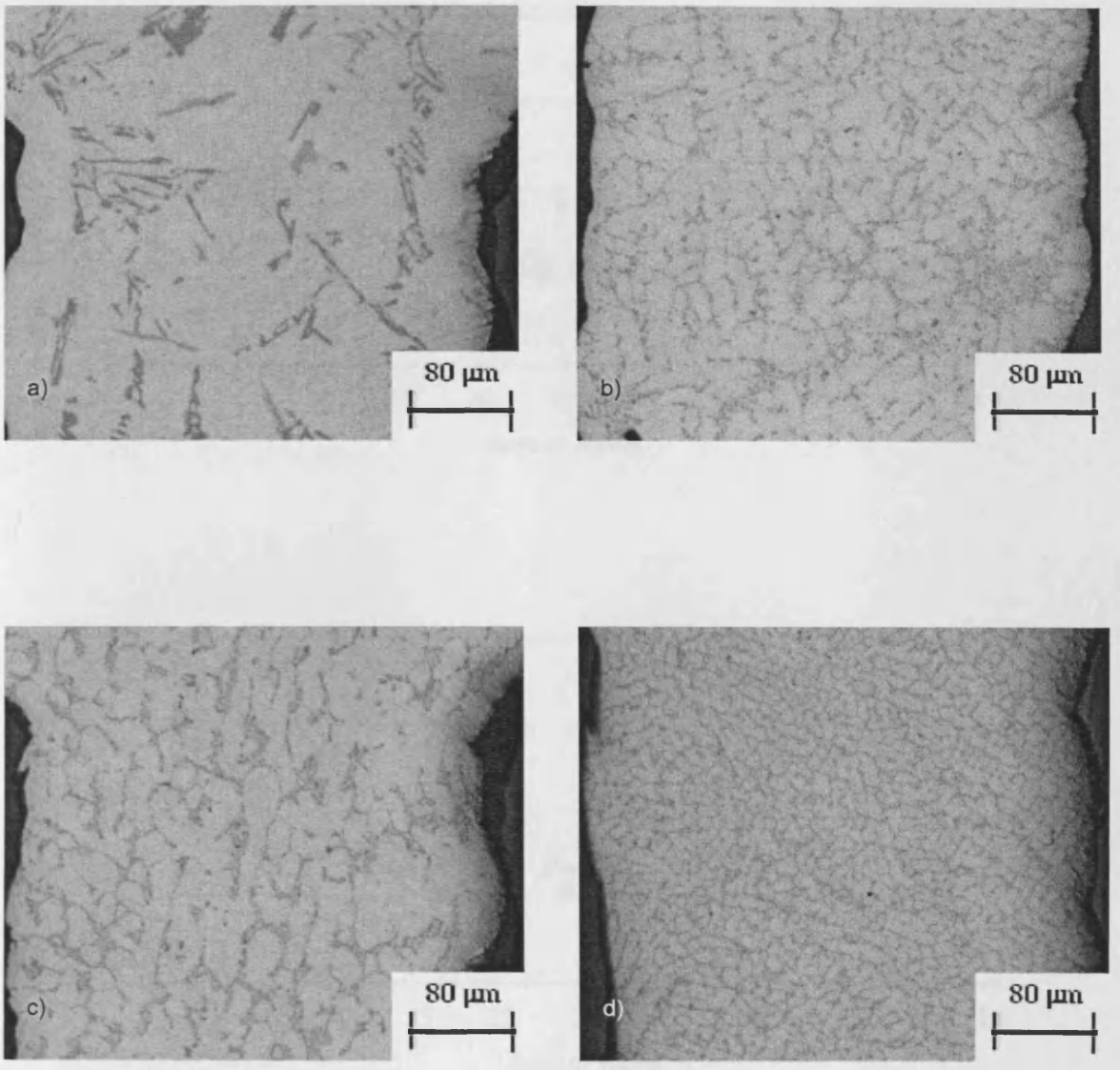

Figure 5.4. Dendritic refinement on a 0.3 mm thick rib:
a) AR 1 T_M 450°C; b) AR 40 T_M 450°C; c) AR 1 T_M 250°C; d) AR 40 T_M 250°C.
(x400 magnification)

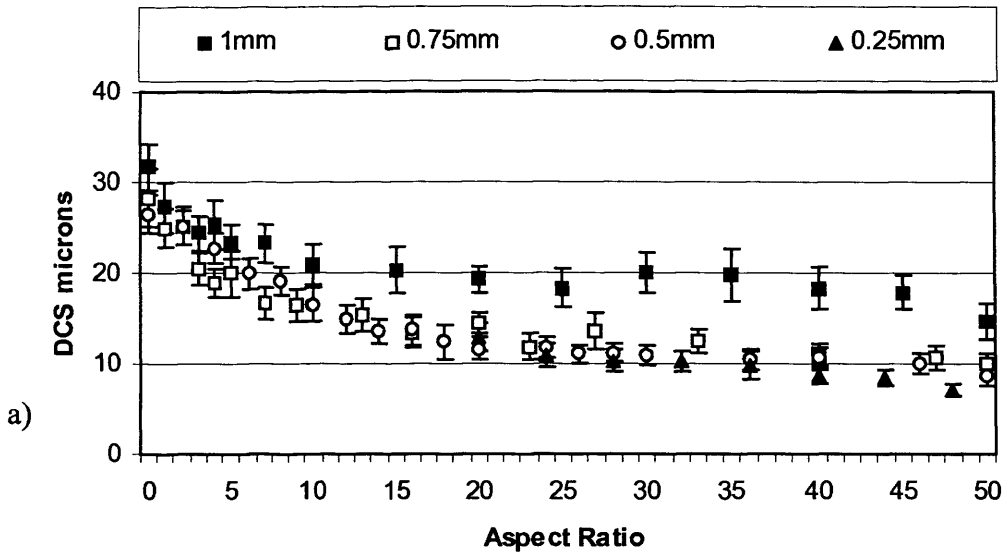

a)

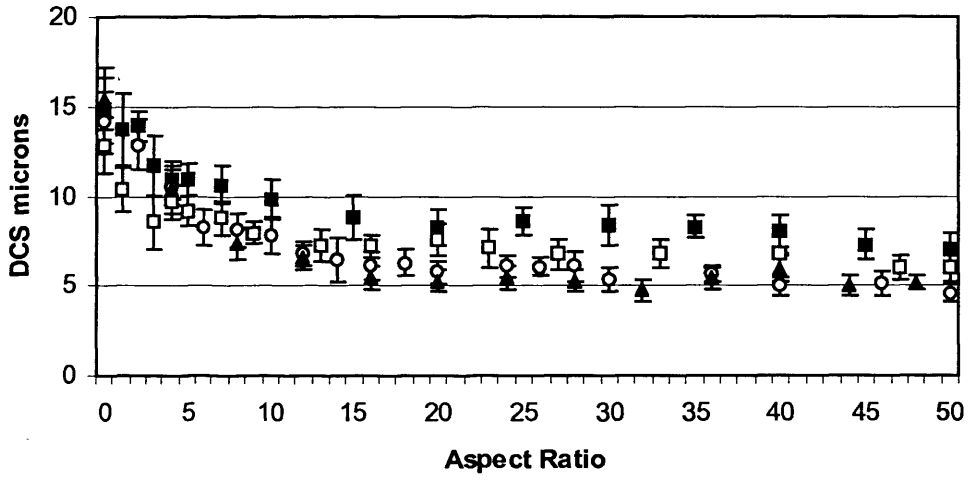

b)

Figure 5.5. Dendritic refinement on the cast ribs with different thicknesses as a function of their AR: a) T_M 450°C; b) T_M 250°C.

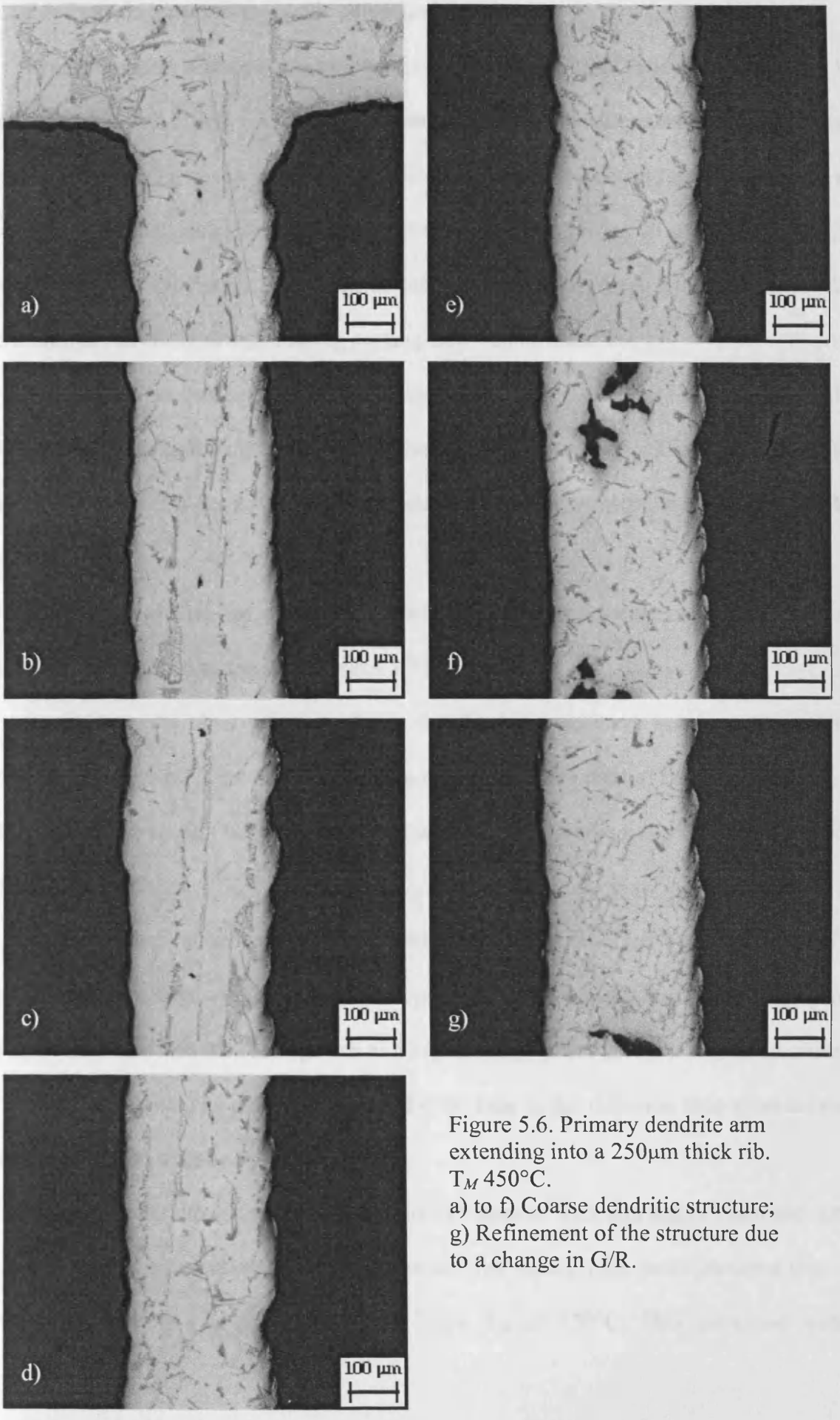

Figure 5.6. Primary dendrite arm extending into a 250µm thick rib. T_M 450°C.
a) to f) Coarse dendritic structure;
g) Refinement of the structure due to a change in G/R.

5.2.2.2. Eutectic Si and intermetallic compounds

In order to give a more complete description of the structural refinement occurring when increasing the AR of cast micro-features, complementary measurements were taken focusing on the morphology of the eutectic Si particles. The importance of this investigation arises from the fact that under normal cooling conditions, Si particles in unmodified alloys are polyhedral and have the form of coarse acicular needles but undergo a morphological change to a fibrous eutectic type under strong cooling-down conditions.

Two parameters were analysed for the Si particles; their maximum Feret's length and their AR, the latter being defined as the ratio of the longest to the shortest Feret. As defined by the software Omnimet, a Feret is the shortest distance between two parallel tangents on each side of a particle.

The average values and respective SD of the measured parameters as a function of the ribs' AR were plotted as shown in figures 5.7 and 5.8.

Resembling the observations made on the dendritic structure but in more reasonable proportions, increasing the ribs' AR led to a structural refinement of the eutectic Si particles (Figure 5.9), here again the consequence of an increasing cooling rate (Brick et al.1965; Ho and Cantor 1995).

This structural refinement of our Si particles was characterized by a reduction of their maximum Feret lengths (Figure 5.7), more pronounced in samples cast at the higher mould temperature. This was the consequence of a higher temperature gradient present in ribs cast at a higher T_M, resulting in a more pronounced difference in the diffusion time allowance of the substitution solid solution Si-Al.

Figure 5.7 also shows that for ribs with thicknesses of 0.25 mm and 0.3 mm and AR<15, the Si particles' size was significantly larger and the values were more scattered than those measured on other ribs produced at the same T_M of 450°C. This correlated with the

development of extended primary dendrites arms observed on those ribs. It has been shown that for unmodified hypoeutectic Al-Si alloys, the eutectic nucleates on the primary dendrites (Makhlouf and Guthy 2001). Therefore, Si particles crystallised in the vicinity of primary dendrites should be expected to be coarser since their nucleation would have started at higher solidification temperatures.

The size of the eutectic Si particles produced at a lower T_M was more consistent. This could be explained by the fact a higher degree of undercooling in the casting would considerably increase the number of nucleation points for the eutectic reaction (Brick 1965), thus resulting in a more homogenous structure both in terms of particle size and repartition.

The typical phase structure of the casting bulk section and ribs is presented in figure 5.9. The phase identification and composition content was studied by EDS (Energy Dispersive X-ray Spectrometry). The analysis was performed on the main structural phases and is presented in figure 5.10.

In contrast to the mould temperature, the ribs' AR did not seem to affect the morphology of the eutectic Si particles. The average AR they exhibited was 2.0 and 1.9 for the mould temperatures of 450°C and 250°C respectively and remained unchanged regardless of the ribs' AR (Figure 5.8). This showed that in the investigated meso/micro long-channel type castings, an increase in the degree of undercooling refined the eutectic structure but did not affect its mode of growth. The fine Si morphology observed at high AR of the ribs differed from that observed at low AR, in the vicinity of the bulk casting body (Figure 5.9). The particles had lost their typical acicular shape and were more rounded, again highlighting the transition from a flake-like eutectic to a more fibrous-like one. A similar observation was made on the intermetallic compounds present in the casting structure, as they also underwent a structural refinement and exhibited more rounded shapes with increasing AR (Figure 5.9).

a)

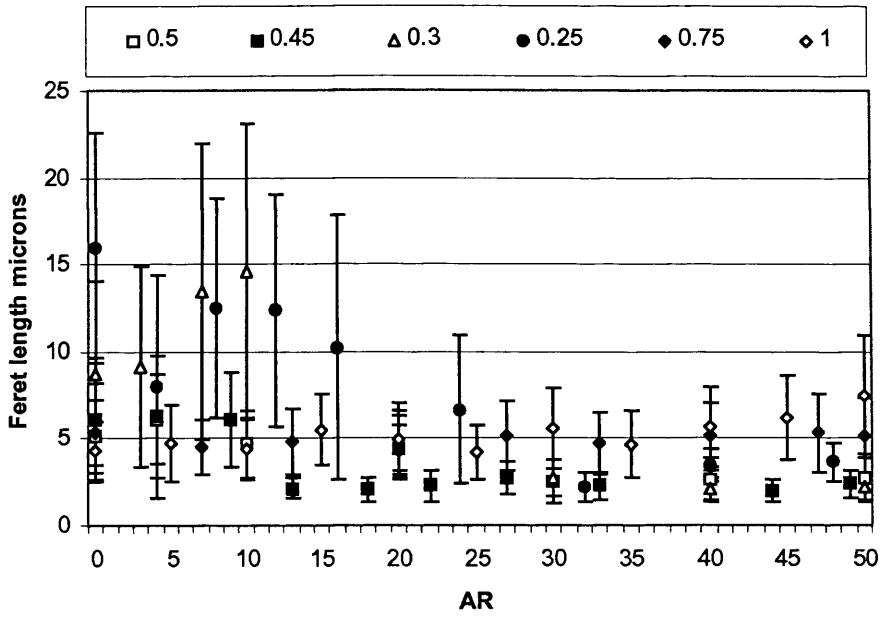

b)

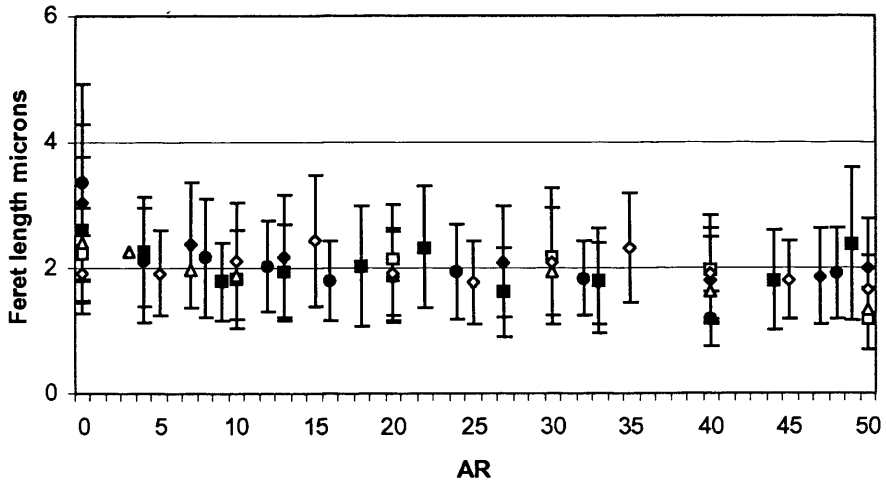

Figure 5.7. Eutectic Si maximum Feret length:
a) T_M 450°C; b) T_M 250°C.

a)

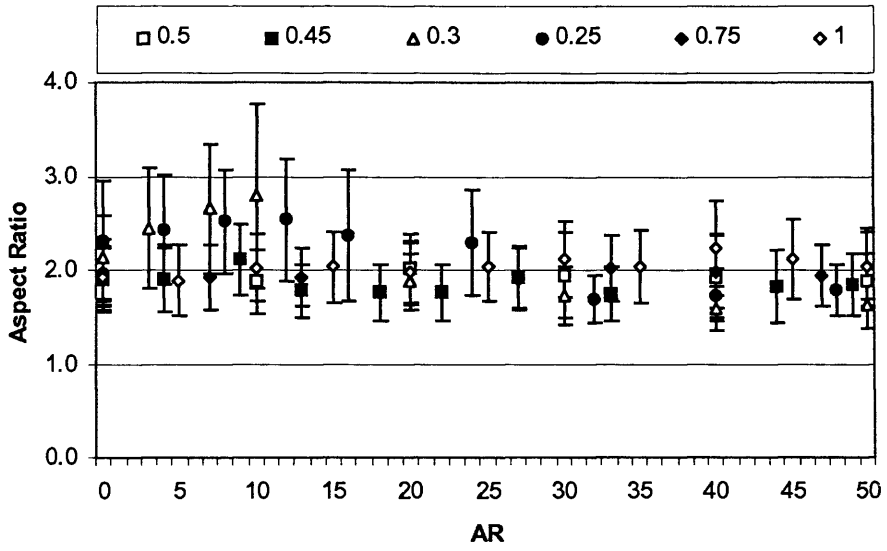

b)

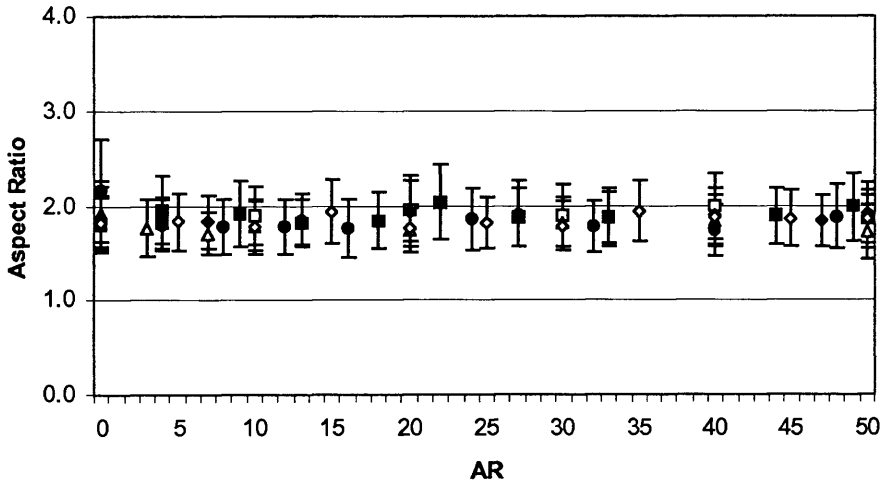

Figure 5.8. AR of eutectic Si particles:
a) T_M 450°C; b) T_M 250°C.

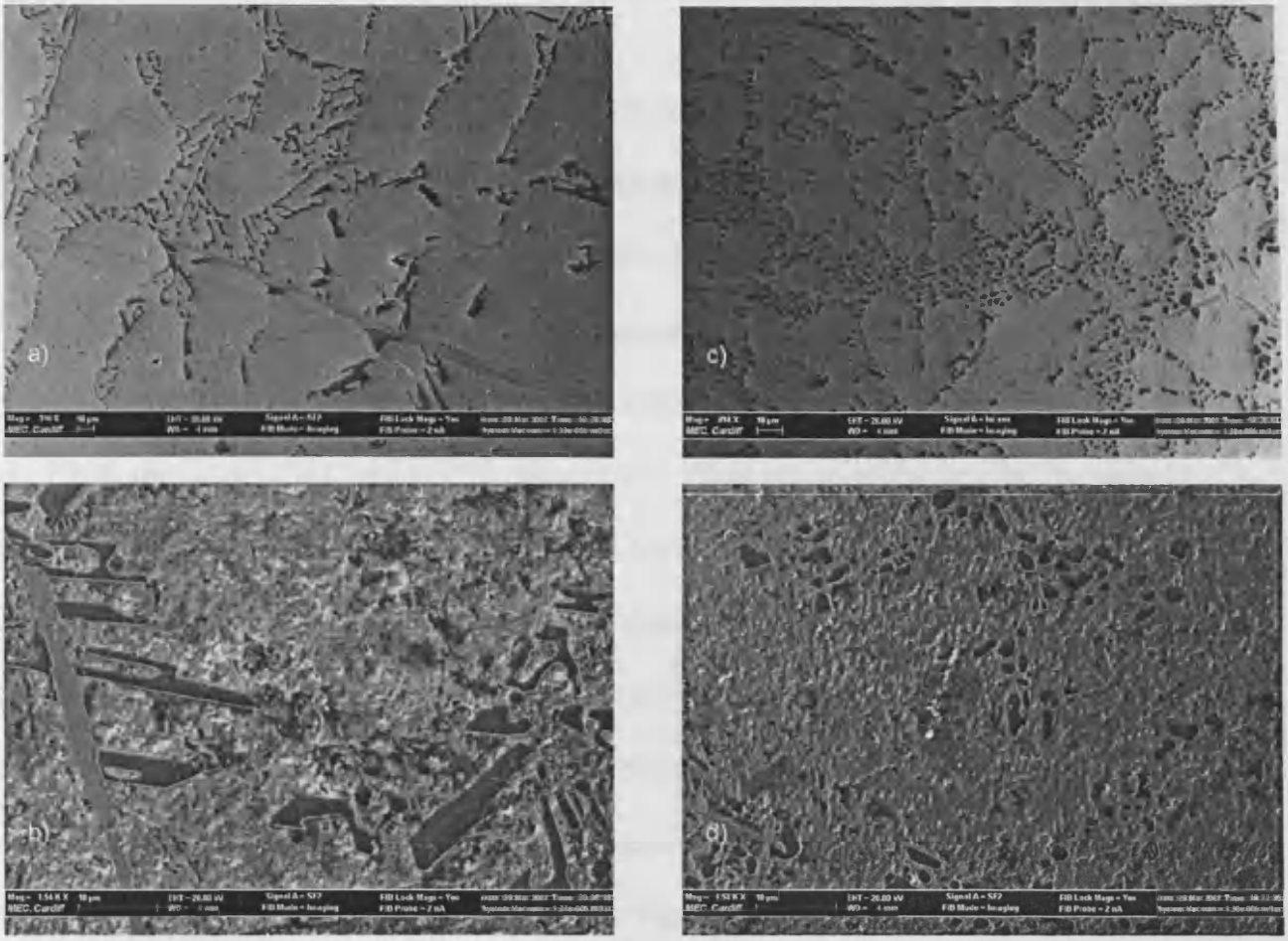

Figure 5.9. FIB images of the eutectic Si particles for different rib's AR at T_M 450°C: a) and b): coarse Si particles at AR1; c) and d): refined Si particles at AR40 (Magnifications: a) and c) x400; b) and d) x1500)

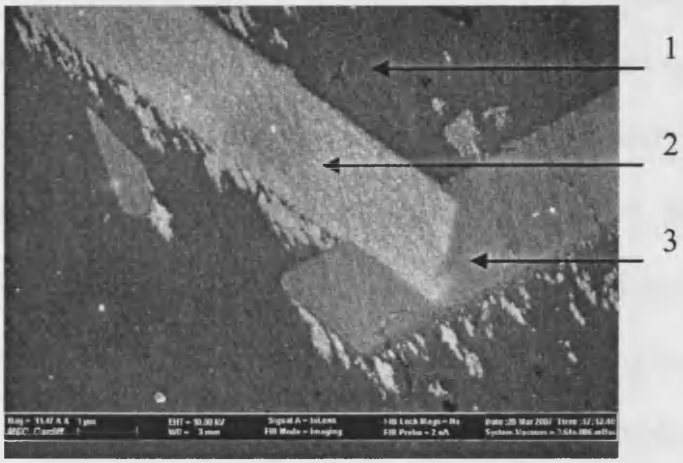

	Location		
Elements	1 (α)	2 (intermetallic)	3 (β)
C	2.02	0.33	2.36
O	0.27	--	--
Al	10.23	6.61	0.84
Si	0.05	0.87	10.24
Mn	--	Traces	--
Fe	--	3.56	--
Cu	--	0.31	--

Figure 5.10. Phases observed in the castings and their composition obtained from x-ray diffraction analysis: 1) α: Solid solution of Si into Al; 2) Intermetallic compound; 3) β: Solid solution of Al into Si. (Magnification x10000)

5.3. Porosity

While performing the metallographic analysis, the level of apparent porosity, defined as the ratio between the pores' area and the total surface area revealed after polishing the samples, was calculated. The measurements were taken both from the ribs and the casting core for each mould temperature. Results are summarised in table 5.1. The level of porosity measured in the castings was greater for samples cast at a higher T_M with percentages of 0.7% and 5.14% for T_M of 250°C and 450°C respectively. When observed on the ribs, the porosity level was also reduced by approximately 80-90% for both processing temperatures. This point was important since it correlated well with the structural refinements observed on the ribs. That is, microstructural refinements characteristic of changing solidification conditions are associated with smaller and more evenly distributed porosities (Spear and Gardner 1963). More precisely, at high solidification rates, the gases present in the melt do not get enough time to merge and coagulate into large porosities. Figure 5.11 illustrates the typical difference in the size of the porosities observed in the ribs produced with the two experimental processing temperatures. It can be seen that T_M has a considerable influence on the size of the micro-porosities formed inside the ribs. If micro-porosities might be negligible from a structural point of view at conventional casting scales, the figure 5.11.a clearly illustrates that a similar assumption cannot be made for micro-castings because of the increasing proportion of the defect relative to the size of the micro-feature. Therefore, it appears essential when casting micro-components to find an optimum compromise between the processing parameters, allowing both a successful mould filling and minimizing at the same time the formation of micro-porosities. Regarding our experiments, and the conclusions drawn from the previous chapters, the appropriate mould temperature should be lowered as much as possible in order to achieve micro-castings with better soundness.

5.4. Empirical Model

In the beginning of this chapter it was shown that the thickness and AR of cast micro-features have a significant effect on their microstructure. The major factor for this occurrence is the severe changes in the solidification conditions of the melt in the thinnest sections of the castings. Therefore, one might expect that models similar to the one proposed by Spear & Gardner could be applied to describe the phenomenon observed in our experiments.

Based on the structural refinement observed with the Rib trials, an attempt was made in this study to propose a model describing the evolution of DCS in the ribs with different thicknesses as a function of their AR. As a first step, an attempt was made to use the typical regression curves available on the Microsoft Excel base pack to fit our data points. Among these functions such as power type, exponential, logarithmic or again polynomial, the power type one best described the data. However, it was still limited in accurately fitting the values of the DCS at high AR. Therefore, it seemed judicious to perform the regression analysis of the DCS data using a more complex model composed of several parameters. A model type named *exponential decay with plateau* was therefore chosen to perform a nonlinear regression analysis of our experimental data. Below is the equation form of the model:

$$DCS = Span \cdot e^{-k \cdot AR} + Plateau \qquad (5.2)$$

The model has three parameters, *Span, k* and *Plateau* (Figure 5.12) that can be associated with different physical aspects of the casting process. In particular, the *Span* describes quantitatively the degree of cells' refinement encountered in each specimen in respect of its overall size and complexity. The parameter *k*, represents the slope of the curve and reflects the sensitivity of the alloy to the degree of under-cooling achieved during solidification. *Plateau* is a threshold value that defines the refinement limit of the alloy for the existing functional dependence between DCS and AR of the features. These parameters are dependent on the thermodynamic characteristics and the freezing range of the casting alloy,

and also on its ability to form dispersive structures under the specific cooling-down conditions for a given investment material.

5.4.1. Best-fit parameters

Each of the twelve sets of DCS data, six ribs' thicknesses per mould temperature, was first independently analyzed using regression analysis software GraphPad Prism 4. The values of the best-fit parameters for each data set calculated through this analysis are summarised in tables 5.2 and 5.3. As may be seen in table 5.2, there were no values reported for the Span, k and coefficients of 'goodness of fit' for the ribs having thicknesses of 0.3 mm and 0.25 mm and produced at a mould temperature of 450°C. This was due to the fact that clearly defined secondary dendrite cells could not be observed in those ribs up to a distance of 5/6 mm away from their base (Figure 5.6) where instead only columnar type primary dendrites were formed. Because of this lack of data, the regression analysis could not be performed for these specific ribs. However, it appeared that the DCS of the microstructure measured above 5/6 mm from these ribs' base were in good agreement with the average values measured on the group of ribs having thicknesses of 0.5-0.45 mm and produced with identical experimental settings. Therefore, it was calculated, independently from the regression analysis, approximated values for the plateau parameter observed for these ribs, assuming that similarly as with the 0.5-0.45 mm, the "Plateau" value was reached for DCS measured above a rib's AR, of approximately 20. The arithmetic mean and SD of the measured DCS for this AR range of 20 to 50 were then used in our study to characterise the Plateau values for the 0.3-0.25 mm thick group of ribs.

Based on the best-fit parameters displayed in the tables 5.2 and 5.3, the evolution of each parameter was plotted as a function of the ribs' thickness for both mould temperatures (Figure 5.13).

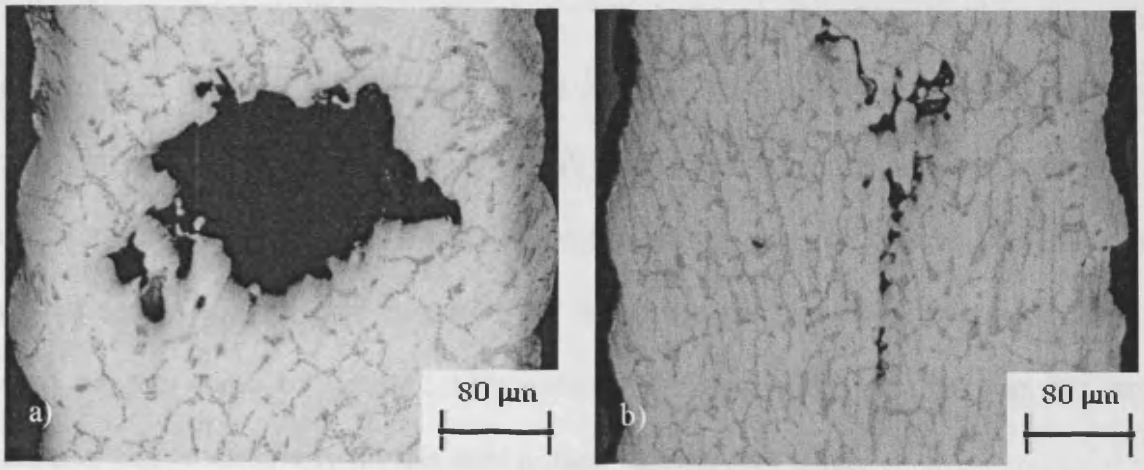

Figure 5.11. Observed porosity in a 0.3 mm thick rib:
a) T_M 450°C; b) T_M 250°C.
(x375 magnification)

	Mould temperatures T_M	
	250°C	450°C
Casting core [%]	0.7	5.14
Ribs [%]	0.084	0.99

Table 5.1. Samples' percentage of apparent porosity for both processing temperatures.

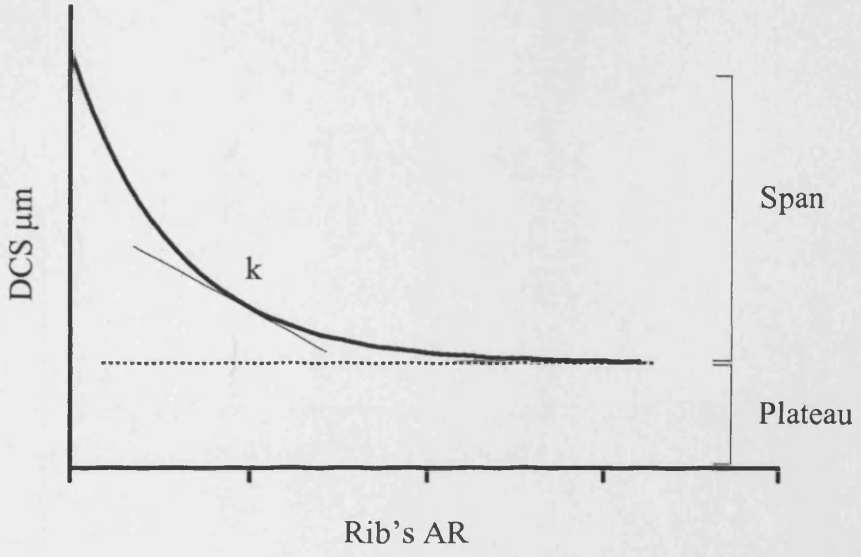

Fig.5.12. Model type: Exponential decay with plateau.

Generally, all three parameters ('Span', k, 'Plateau') were sensitive to T_M. Also, their dependence upon the ribs' thickness was more moderated for the lower mould temperature, especially in case of the 'Span' and 'Plateau' parameters. Regarding the parameter k, it seemed to correlate mainly with T_M and the corresponding degree of under-cooling achieved in the castings. Also, the data scattering of the parameter 'k' characterized by the SD displayed on the graph of figure 5.13.b reduced for thicknesses smaller than 0.5 mm, indicating its higher sensitivity for this thicknesses' dimensional range.

The important point observable from the charts of figure 5.13 is that each parameter remains relatively constant for the range of thicknesses 0.5mm-0.25mm, manifesting the dominating influence of the processing parameters over the dimensions in the solidification conditions of cast micro-range features. Therefore, and since this dimensional range of thicknesses is more representative of a micro-feature than the range 1.0-0.75 mm (Masuzawa 2000), a rib structure refinement model was developed taking the average value among each parameter in the dimensional range 0.5mm-0.25mm. These values are presented in table 5.4.

Parameters	Rib thicknesses for mould 450°C					
	1mm	0.75mm	0.5mm	0.45mm	0.3mm	0.25mm
SPAN	11.5	15.4	18.0	19.4	---	---
K	0.143	0.143	0.092	0.104	---	---
PLATEAU	18.2	11.7	9.5	8.0	**9.4**	**9.1**
Goodness of fit						
R^2	0.89	0.95	0.99	0.99	---	---
Absolute SS	28.91	19.30	6.85	3.33	---	---
Sy.x	1.49	1.22	0.65	0.49	---	---

Table 5.2. Best-fit parameters from nonlinear regression analysis for T_M 450°C.

Parameters	Rib thicknesses for mould 250°C					
	1mm	0.75mm	0.5mm	0.45mm	0.3mm	0.25mm
SPAN	6.8	5.2	9.0	7.9	8.0	10.3
K	0.146	0.161	0.145	0.171	0.154	0.183
PLATEAU	7.9	6.7	5.4	5.1	5.2	5.2
Goodness of fit						
R^2	0.95	0.90	0.97	0.97	0.98	0.99
Absolute SS	3.67	5.04	3.38	2.93	1.51	1.16
Sy.x	0.53	0.62	0.46	0.46	0.34	0.34

Table 5.3. Best-fit parameters from nonlinear regression analysis for T_M 250°C.

	Mould temp. T_M	
Parameters	250°C	450°C
Span	8.81	18.72
k	0.163	0.098
Plateau	5.21	9.0

Table 5.4. Averaged parameters from tables 5.2 and 5.3 considering the ribs' thicknesses of 0.5-0.25mm.

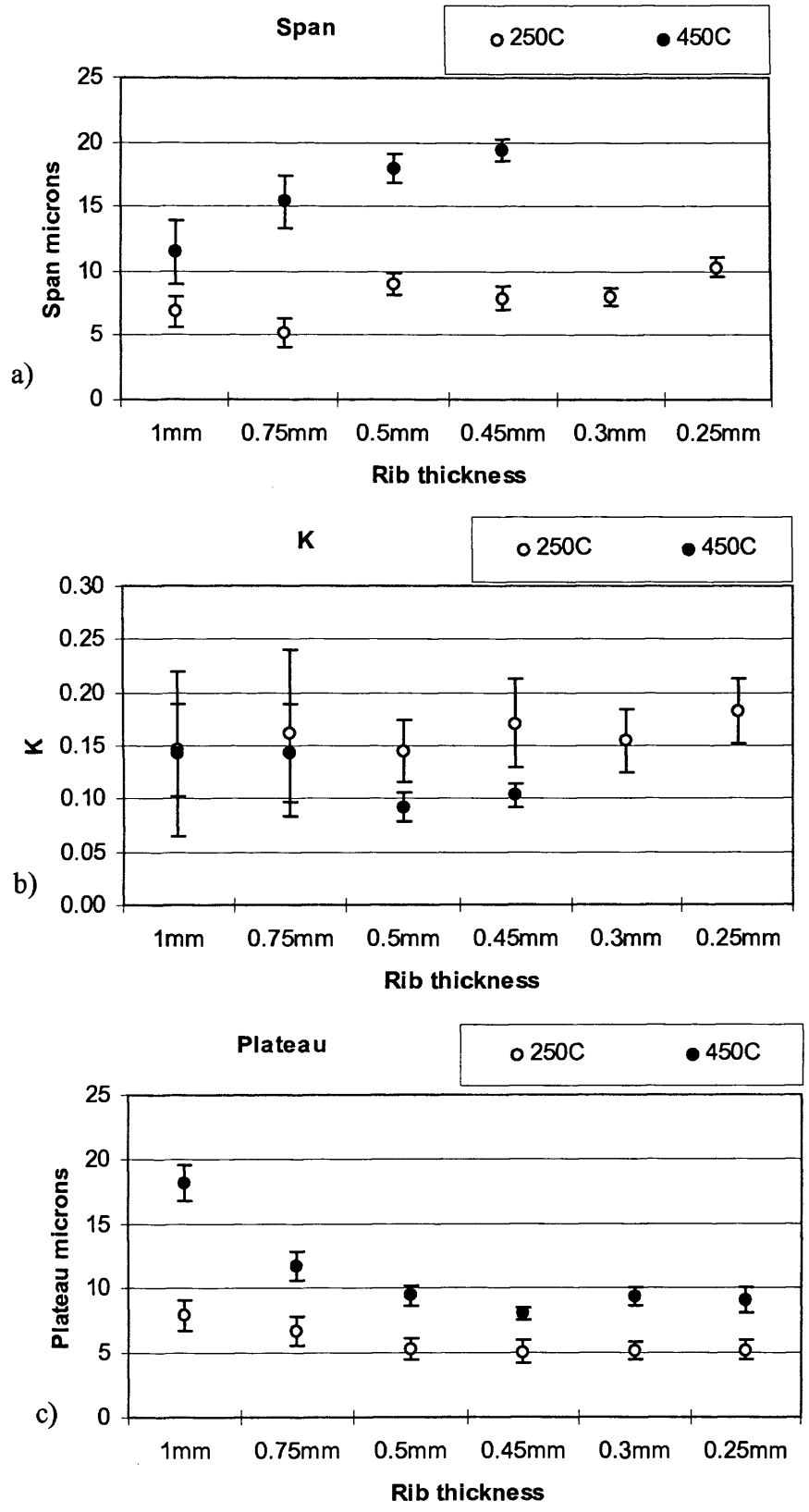

Figure 5.13. Best-fit parameters from the non-linear regression analysis: a) Span; b) k; c) Plateau.

5.4.2. Comparison of the rib structure refinement model with the data points

Using the parameters determined in table 5.4, the experimental data were compared to the rib structure refinement model through a second nonlinear regression analysis performed for both mould temperatures. Figures 5.14 and 5.15 illustrate the curves representative of the calculated preliminary models together with the experimental data. The regression analysis allowed the calculation of two coefficients describing the 'goodness of fit' of the data point with the model. The coefficient of determination R^2 , which describes how well the regression curve fits the data points and the SD of the residuals S_{xy} which quantifies the degree of scatter of the data around the curve, were calculated.

As may be seen from figures 5.14.a and 5.15.a, the calculated empirical model correlated well with the dimensional range 0.5-0.25 mm. This observation was confirmed by the high values of the coefficients of determination R^2 and the low scatter of the data around the regressed curve. Only the 0.3-0.25 mm thick ribs produced at a T_M of 450°C showed lower R^2 values. This was due to the fact that fewer DCS data points were considered for the calculation of R^2 for these ribs.

Figures 5.14.b and 5.15.b, on the other hand, illustrate the departure of the models from the experimental data with the increase of the rib thickness, more pronounced for the higher T_M. The lower values of the R^2 together with the increase of S_{xy} characterized the higher deviation of the model from the experimental data. This observation shows that for thicknesses above 0.5 mm, the solidification conditions dictating the as-cast metallographic microstructure differs from those of micro-scale ribs.

Comparing the values of the parameters obtained at different processing temperatures, it appeared that employing a higher T_M resulted in a significantly higher Span value, characteristic of a greater structural heterogeneity of the cast micro-feature. In addition, the higher value of the parameter k obtained for the lower mould temperature showed that the

metallographic structure was more rapidly refined than with the higher processing temperature. Therefore, the Plateau value was reached at a lower ribs' AR, which resulted in higher structural homogeneity for the ribs. Quantitatively, the Plateau parameter, interdependent of the other two, was reached for AR of approximately 20 and 40 for the processing parameters of 250°C and 450°C respectively. To conclude, when producing cast micro-features with a high AR, one should reduce as much as possible the mould processing temperature in order to achieve higher structural homogeneity for the castings.

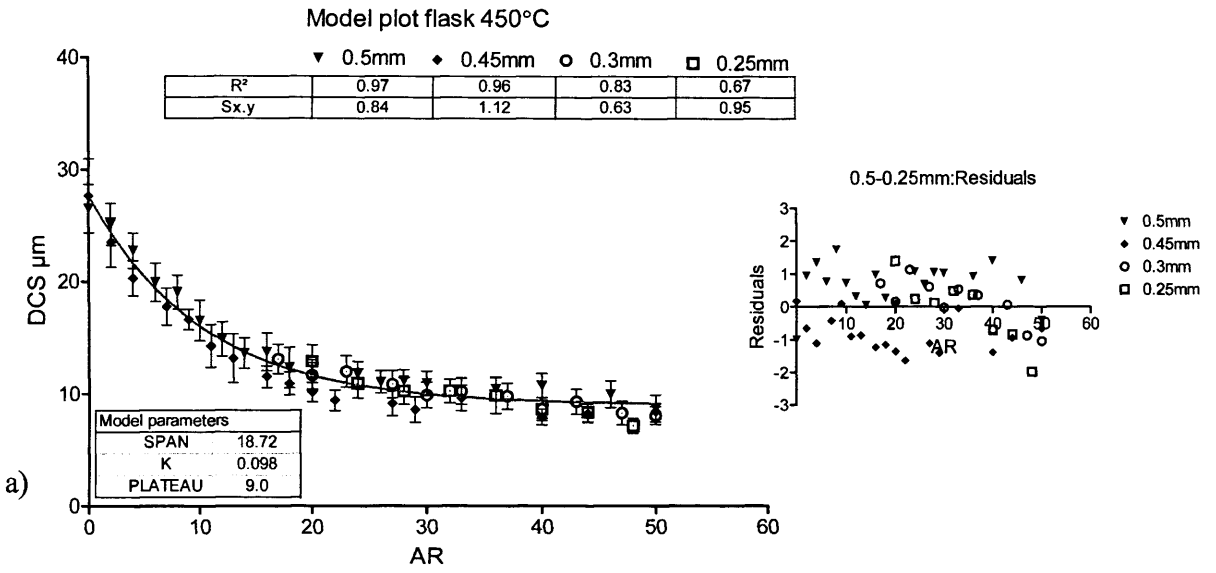

a)

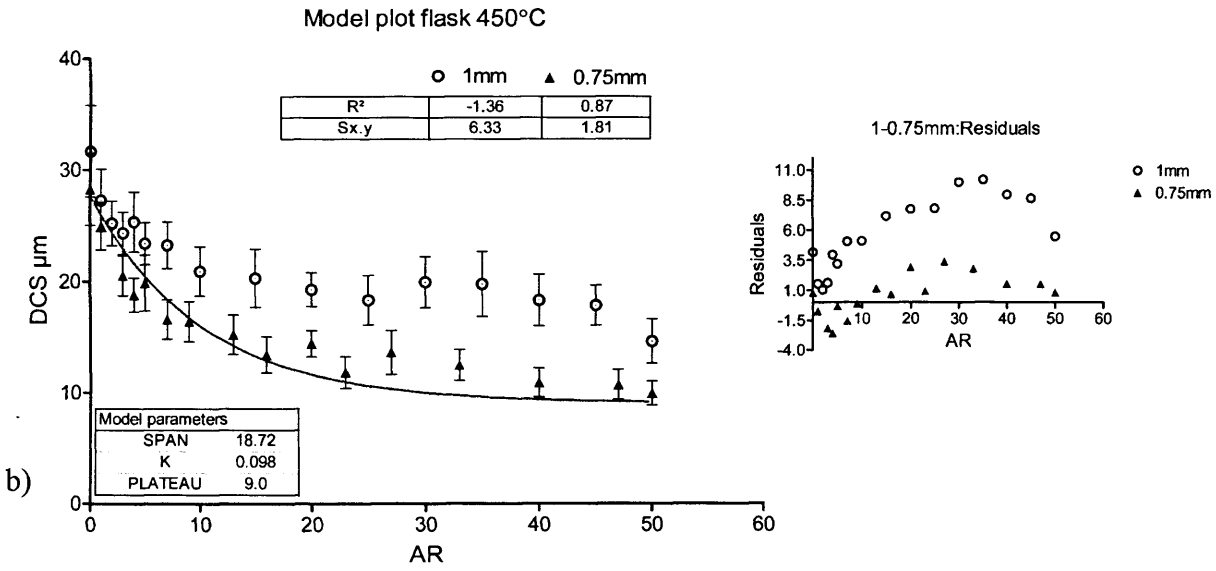

b)

Figure 5.14. Model plot for T_M 450°C.

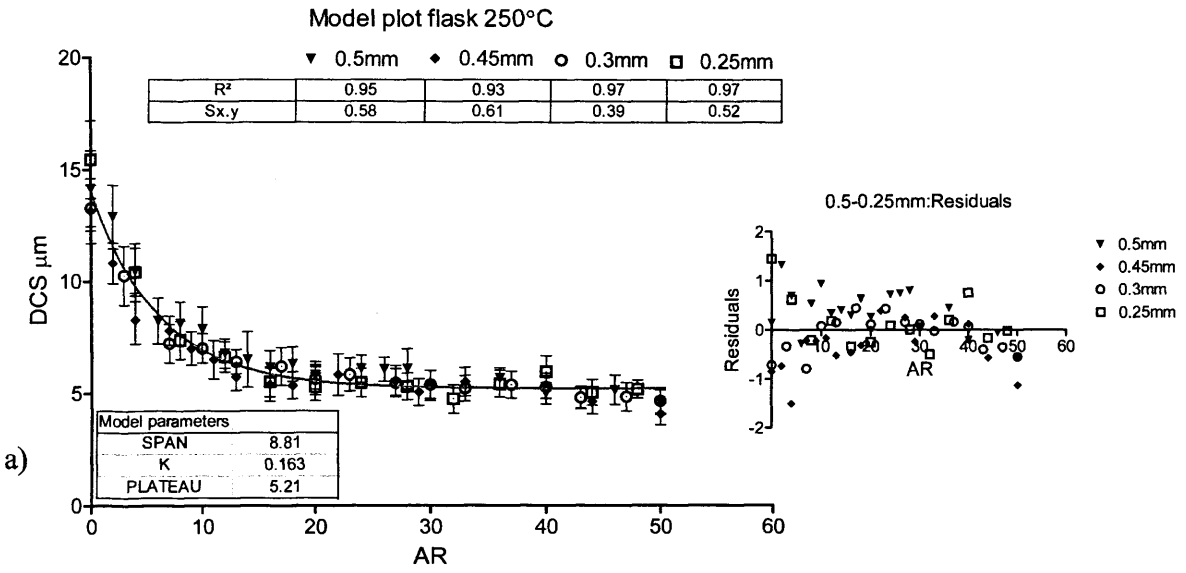

a)

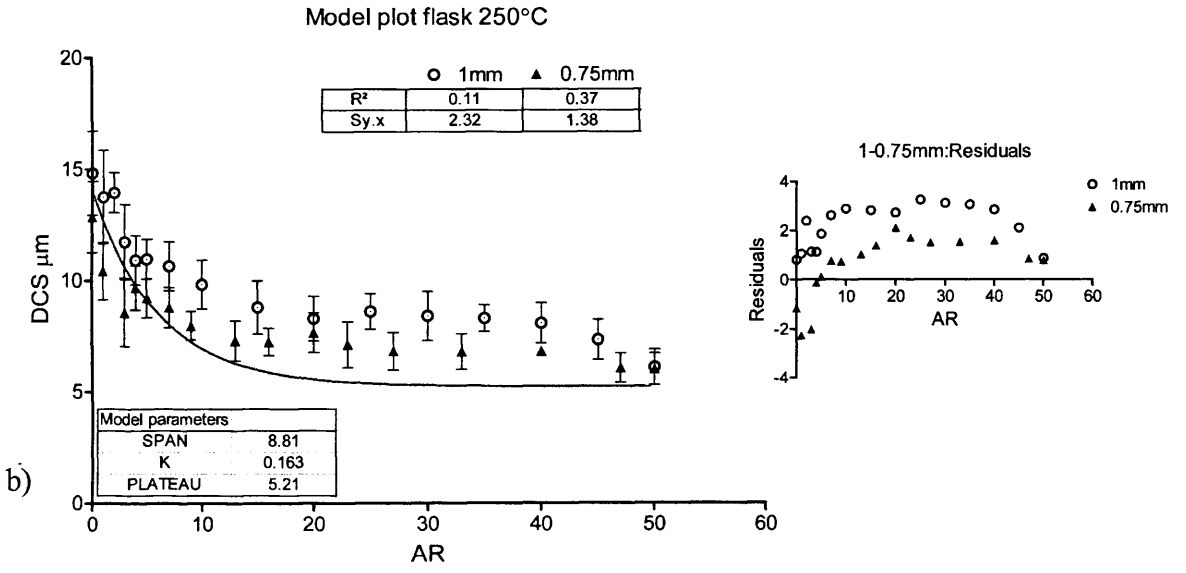

b)

Figure 5.15. Model plot for T_M 250°C.

5.4.3. Model's parameters optimisation

The purpose of this section is to optimize the best-fit parameters previously obtained and to calculate their 95% confidence interval (CI) using a Monte Carlo data simulation (Gentle 1998). Since it was demonstrated earlier that the group of ribs having thicknesses in the range of 0.5-0.25 mm underwent similar solidification conditions regardless of their thicknesses, the calculation of the model's optimized parameters was based on the average DCS values and SD of each of the two 0.5-0.25 mm thick group of ribs (Appendix 5.1). The two sets of data were first analysed using a nonlinear regression similar to that used in §5.5.2 so that new parameters could be calculated (Table 5.5). Using the latter parameters' values, a group of fifty sets of data was generated for each processing temperature with a random scatter equivalent to the average SDs calculated for each group of ribs, respectively 1.53 and 2.60 μm for the mould temperatures of 250°C and 450°C (Appendix 5.1). Doing so, the simulated data would have been similar to what one would have observed if the experiments were repeated 50 times.

Finally, each set of the generated fifty sets of data was analysed individually as in §5.5.2. which provided fifty different values for each respective parameter (Appendix 5.2). These values, which followed a Gaussian distribution (Appendix 5.3), were then used to calculate the 95% CI on the parameters of table 5.6 according to the following equation:

$$95\%CI = 1.96 \times \left(\frac{\sigma}{\sqrt{n}} \right) \qquad (5.3)$$

where σ - SD of the population; n – population.

After calculation of the best-fit parameters, the optimized model was compared to the original DCS data to verify whether or not the goodness of its fitting was improved. The results of this regression analysis together with its associated plots are summarized in figure 5.16 It can be seen that the quality of its fitness to the DCS data slightly improves for the

mould temperature of 450°C as highlighted by both the R^2 and S_{xy} coefficients regarding the 0.3-0.25mm thick ribs (Figure 5.16.a). The lack of DCS data at low AR on these ribs was still responsible for the relatively low value of the R^2 coefficients obtained from the regression analysis. Considering the 250°C mould temperature, no significant changes were observed compared with the regression analysis performed in §5.5.2. Therefore, the parameters calculated in this section were kept for the rest of this study to develop the expression of our general model.

5.4.4. Expression of the general model

The aim of this section is to develop the equation of a general model characterizing the evolution of the DCS of the cast micro-features as a function of the mould temperature. To do so, each parameter (Span, k and Plateau) was expressed as a function of T_M assuming a linear relationship of each parameter between the two processing temperatures. The plots of these parameters as a function of T_M together with their associated linear equations are shown on figure 5.17. Finally, by implementing these equations into equation (5.2), the general expression of our empirical model was generated.

$$DCS = \left(5.E^{-2} \cdot T_M - 3.85\right) \cdot \exp^{-\left(\left(-3.5.E^{-4} \cdot T_M + 0.25\right) AR\right)} + \left(1.7.E^{-2} \cdot T_M + 0.98\right) \qquad (5.4)$$

where T_M - mould temperature; AR- Aspect Ratio

This model has been used to generate several theoretical curves with different mould temperatures of 150, 250, 350, 450 and 550°C (Figure 5.18).

Model Parameters	Mould Temp. T_M	
	250°C	450°C
SPAN	8.65	18.65
K	0.162	0.092
PLATEAU	5.24	8.65

Table 5.5. Model best-fit parameters.

95% CI on Model Parameters	Mould Temp. T_M	
	250°C	450°C
SPAN	0.3203	0.3859
K	0.0111	0.0045
PLATEAU	0.0907	0.2074

Table 5.6. 95% CI on the best-fit parameters of table 5.5.

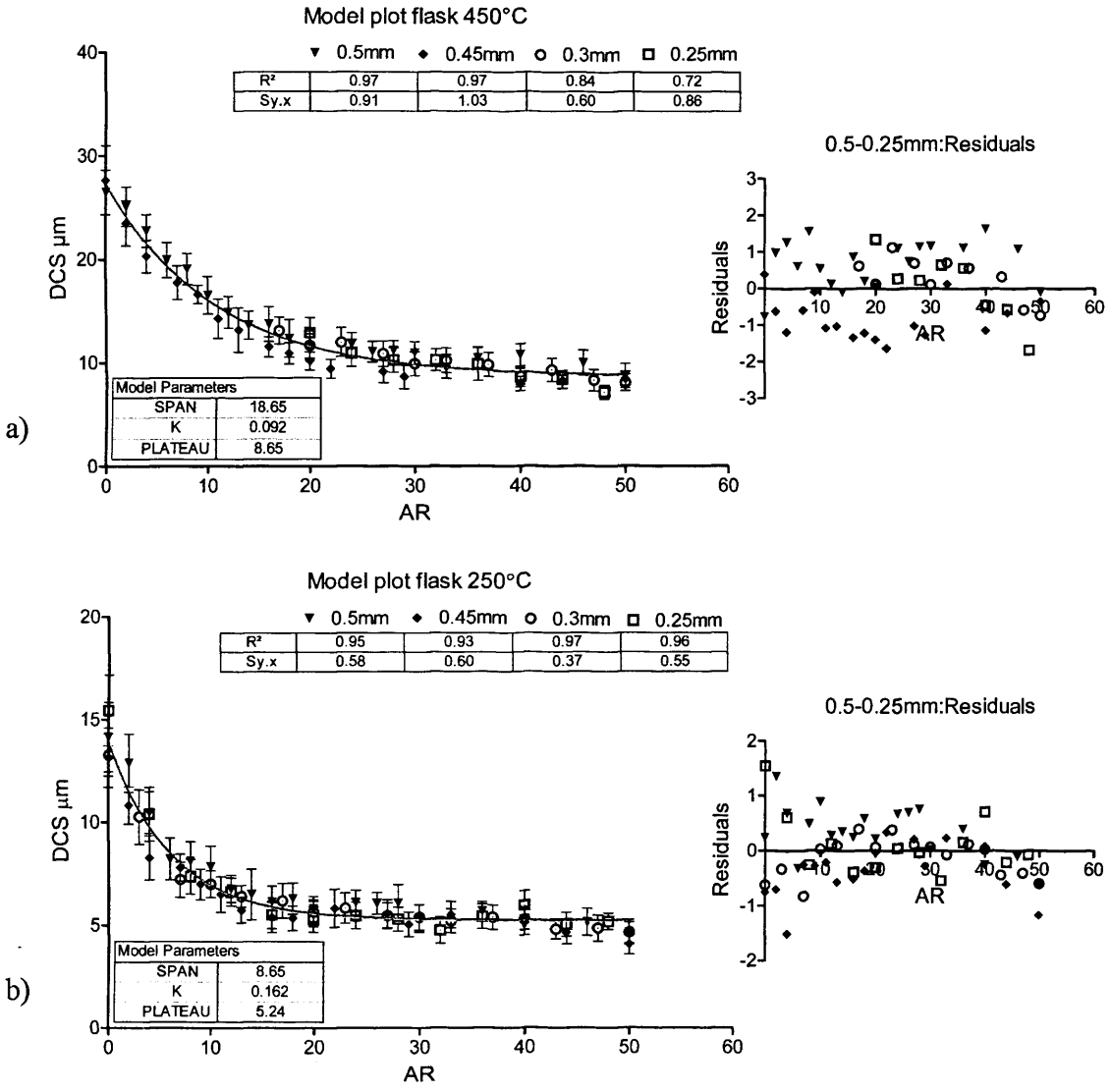

Figure 5.16. Plot of the optimized model together with the measured DCS: a) T_M 450°C; b) T_M 250°C.

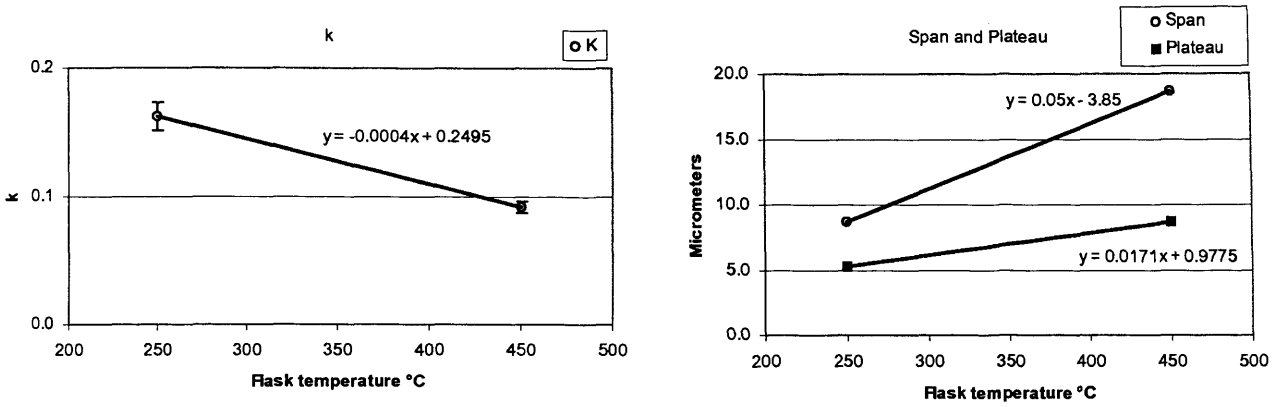

$k = -3.5.E^{-4} + 0.25$ $\quad Span = 5.E^{-2}.T_M - 3.85$ $\quad Plateau = 1.7.E^{-2}.T_M + 0.98$

Figure 5.17. Expression of each optimized parameter as a function of T_M.

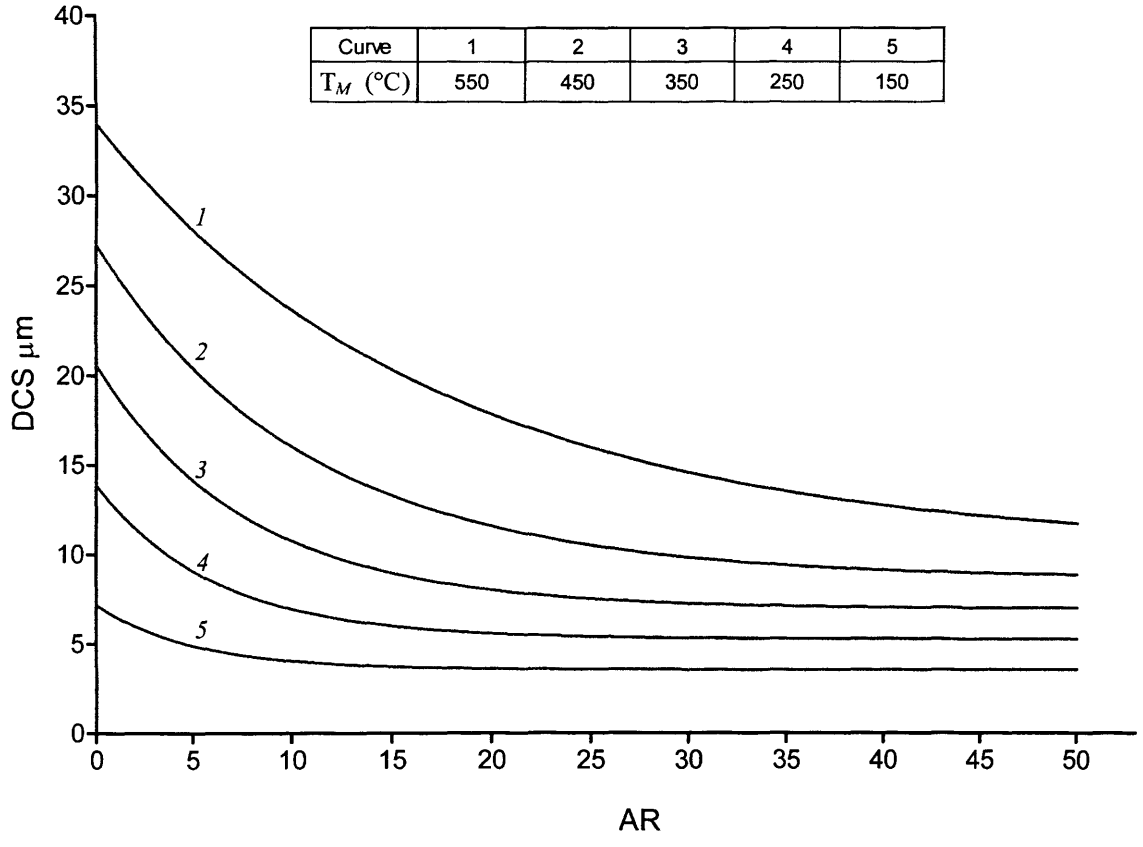

Figure 5.18. Family of theoretical curves generated for different T_M.

5.5. Mechanical properties of the cast micro-features

The microstructure of the casting micro-features directly affects the mechanical properties (hardness, ductility and strength) of the castings and therefore their machinability (e.g. by micro-milling) if additional processing is required to reach the desired functionality of the micro-part. Also, finer microstructures in Al-Si casting alloys lead to superior thermal conductivity properties of these alloys (Vásquez-López et al 2000). Therefore, it is interesting and practically important from an engineering point of view to examine the micro-mechanical properties of the alloy. This data could be of interest for developing various micro-casting demonstrators such as cooling devices, heat exchangers, micro-fluidics channels, micro-gear boxes, delicate jewellery, polymer replication micro-tools etc...

Following the structural refinement observed on the rib samples, the changes in their mechanical properties as a function of the AR could be explored. Micro-hardness (Mott 1956) measurement is one of the favoured methods for such investigation since it is a simple and non-destructive method of assessing the resistance of the material to plastic deformation (William 1997). By choosing an appropriate indentation load, Micro Hardness Vickers (MHV) is suitable for depicting the changes in properties in micro-sample sections of aluminium alloys. It is also one of the most sensitive methods for detecting the influence of even the most delicate structural changes to the mechanical behaviour of the alloy. Other mechanical properties such as yield strength (YS) might be assessed from MHV using different mathematical models (William 1997). An example of such a proportionality relationship, which was not implemented in this study, was presented by (Brusethaug and Langsrud 2000). In this article, the Hardness Vickers (HV) of aluminium casting alloys was linked to their tensile properties using a Ludwig's stress-strain law type, according to the following equation:

$$HV=1/3\ (YS+K*\varepsilon^{n}) \qquad (5.5)$$

Where: ε - true strain caused by the material hardness indentation; n - strain hardening exponent which is constant for a given material (typical values falling between 0.1-0.5); K - strength or stress coefficient which is structure dependent and varies with processing.

Although the use of such a semi-empirical approach for determining the tensile properties of castings is limited, since it does not take into account the presence of structural defects, scale factor and the difference in the stress-strain conditions between tensile test and indentation test, it might provide a fair means of estimating approximate values of the alloy's tensile properties.

Due to the micrometre scale of the rib samples, Micro Hardness Vickers (MHV) were taken on the group of ribs with dimensions 0.5-0.25 mm using a load of 0.05 kg. Results were plotted as a function of their AR as shown in figures 5.19.a and 5.19.b. As may be seen on these graphs, the measured MHV appears to be strongly dependent on the ribs' AR. No significant distinction can be made between MHV measurements taken for the whole range of thicknesses produced under similar cooling down conditions (i.e. similar T_M). Then, in order to compare the results obtained under the two experimental conditions, the arithmetic mean between each set of MHV data was calculated and plotted (Figure 5.19.c).

Generally, the lower the mould temperature and consequently the finer the metallographic structure, the higher the measured MHV, as highlighted by the moving average trend lines displayed in figure 5.19.c. The total increase in MHV was of approximately 10% and 13% for the processing temperatures of 250°C and 450°C respectively. Thus, one might expect a similar increase in the tensile properties of these ribs while increasing their AR. Also, both curves exhibited a similar trend, which was characterized by a linear increase of the MHV up to an AR of approximately 25 before stabilising. The fact that the MHV did not increase further for AR above 25 correlated well with the Plateau threshold observed for the structural refinements of the rib castings.

Therefore, and to conclude this work, an attempt was made to identify a possible Hall-Petch (Petch 1953) relationship between the MHV measurements performed on the ribs with thicknesses in the range of 0.5-0.25 mm and the structural refinement described by the model. To do so, the evolution of the MHV was plotted as a function of the inverse square root of the DCS values provided by the model (5.4) (Figure 5.20). This plot was similar to that of the Hall-Petch equation, which describes the dependence of the metals' yield strength on grain size. Through a linear regression, it appeared that the data correlated by more than 70% as highlighted by the values of the coefficient of determination R^2 of figures 5.20.a and 5.20.b. These observations showed that the evolution of the MHV of an Al-Si-Mg casting alloy could be linked to its structural refinement employing a Hall-Petch equation type such as:

$$MHV = MHV_0 + K_H * (DCS)^{-1/2} \qquad (5.6)$$

where, similar to the Hall-Petch equation, MHV_0 and K_H are constant for a given material and processing parameters.

a)

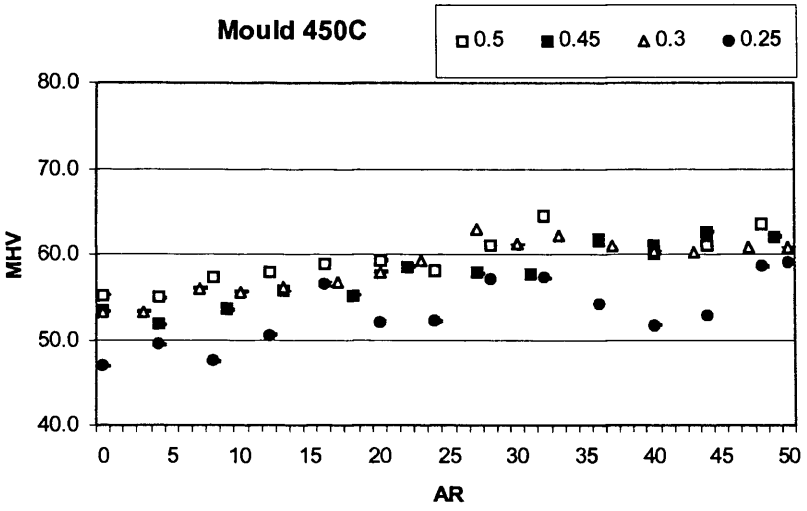

b)

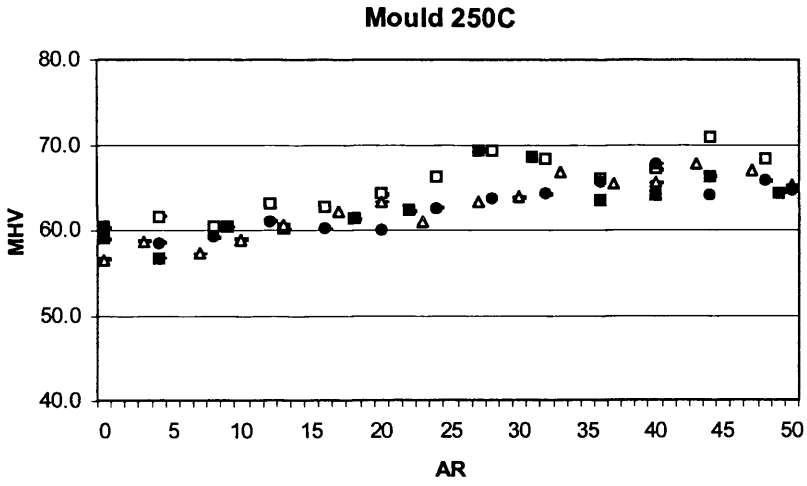

c)

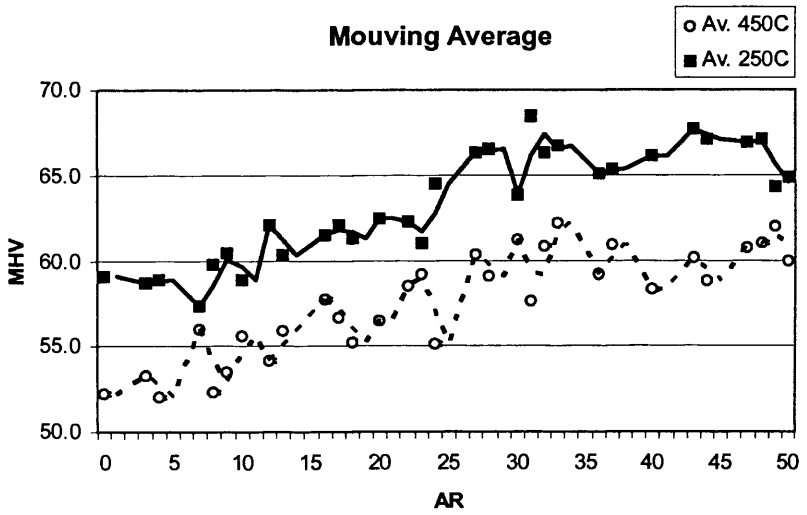

Figure 5.19. Evolution of the MHV as a function of the ribs' AR for the 0.5-0.25 mm thick group of ribs.
a) T_M 450°C; b) T_M 250°C; c) Moving average curves for each T_M.

a)

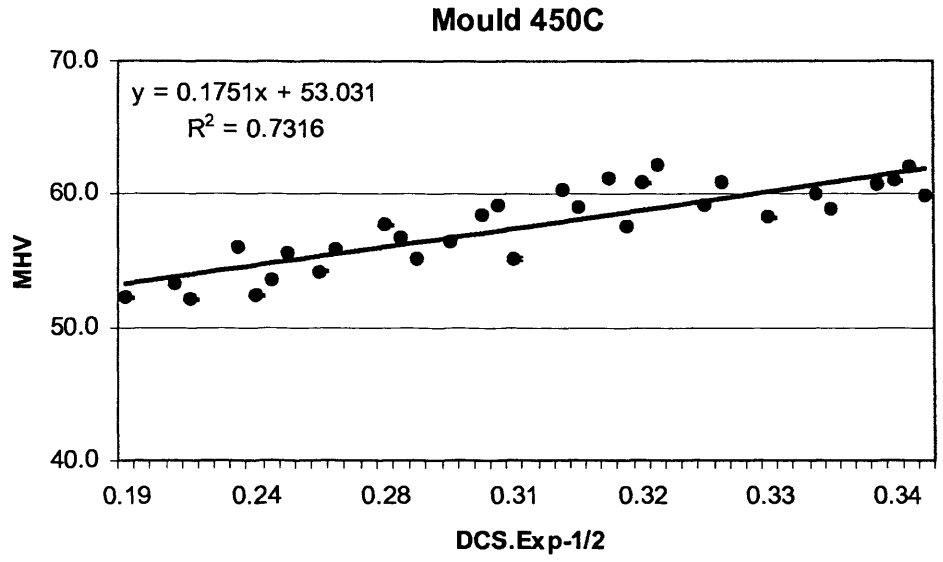

b)

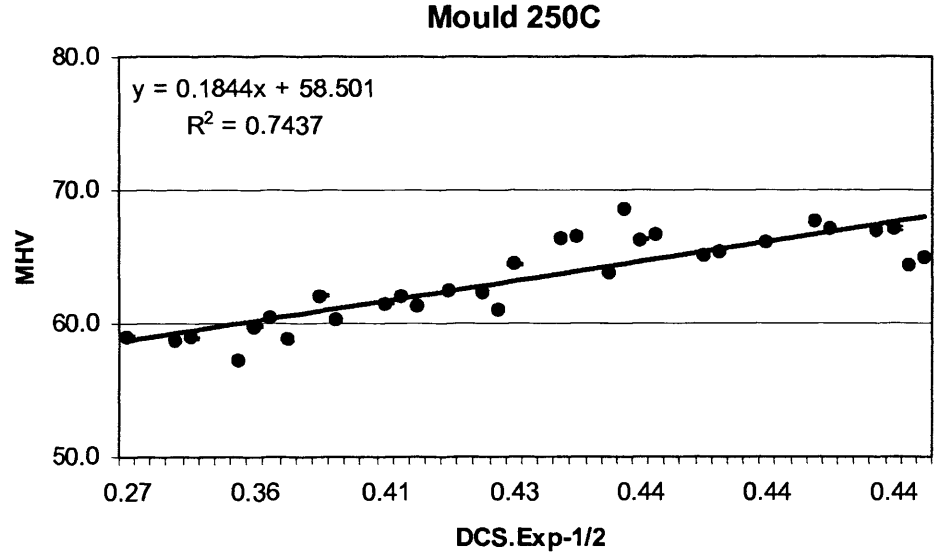

Figure 5.20. Evolution of the MHV as a function of the ribs' AR for the 0.5-0.25 mm thick group of ribs:
a) T_M 450°C; b) T_M 250°C.

5.6. Summary

This chapter presents the results of a metallographic analysis performed on LM25 cast features with AR up to 50 and decreasing thicknesses from the millimetre down to the micrometer range. An empirical model describing the microstructural refinements occurring on cast micro-features as a function of their AR and processing parameters is proposed. It also provides a model describing the interdependence of the DCS upon the MHV of micro-castings. The main conclusions from this study are as follows:

- It was found that the solidification rate of micro-castings and thus their resulting microstructure was AR sensitive, which represents a fundamental difference with the solidification behaviour of conventional macro-castings.
- Important refinements of the as-cast dendritic structure could be observed in cast micro-features with the increase of their AR.
- The eutectic Si particles were also refined by the changing solidification conditions occurring in the cast micro-features, which shifted their typical flake-like morphology towards a more fibrous one.
- The mould temperature should be lowered as much as possible in order to reduce the amount and size of micro-porosities present in the castings.
- The structural refinements observed on all phases and constituents of the castings were more pronounced for castings produced at a higher mould temperature, consequently leading to their greater structural heterogeneity.
- No distinction could be made in the solidification conditions of micro-features with thicknesses smaller than 0.5 mm. Therefore, the thickness of micro-features should not be regarded as a prerequisite for achieving fast cooling rates with a corresponding favourable structure.

- Based on the 0.5-0.25 mm thick group of cast micro-features, an empirical model describing the structural refinements of the as-cast DCS as a function of the mould pouring temperature and features' AR was proposed.
- The DCS refinement observed in the micro-features led to a total increase in hardness of approximately 10% and 13% for the mould processing temperatures of 250°C and 450°C respectively.
- Finally, it was found that the DCS refinement proposed by the model correlated well with the increase of the metal hardness according to a Hall-Petch equation type.

To conclude, it appears that in micro-casting, the mould temperature is still an important parameter, if not even more so, to the achievement of sound castings than at conventional casting scales. Therefore, when producing cast micro-features with high AR, one should reduce as much as possible the mould processing temperature in order to achieve a higher structural homogeneity of the castings and thus enhance both their mechanical and thermal conductivity properties.

CHAPTER 6: Conclusions

6.1. Conclusions and contributions

This thesis has shown that the combination of rapid prototyping and investment casting is a suitable process for the rapid manufacture of sound meso/micro castings incorporating micro-features with AR up to 50 using conventional casting alloys. The capabilities of this manufacturing process have been studied and a comparison between the classical LWP and the recently developed Fcubic direct shell process has been undertaken. Through this analysis, the causes of accuracy loss inherent to these multi-step processes have been identified and the respective advantages of the different manufacturing routes highlighted. It is important to note that some variability between the accuracy and consistency of identical RP machines coming out of a factory's production line will always occur. Therefore, the reader has to keep in mind that the results from the experimental work carried out in this research may vary to some extend if one was to repeat it in a different laboratory. Thus, the conclusions of this research should be seen more as an indicator of performance rather than a final say regarding the capabilities of each of the studied technologies.

Issues regarding the quality of cast micro-features have then been approached from a structural point of view and compared to the general solidification conditions occurring at conventional casting size. The main conclusions of this research are:

- The selection of the RP manufacturing route appears to be one of the dominant factors influencing the final accuracy of the final metallic part due to the decreasing

influence of the metal solidification shrinkage when reducing the castings' sections down to the millimetre and sub-millimetre range;

- All three RP routes suffer from surface finish issues related to their manufacturing process. However, the impact upon the casting soundness varies significantly for the different processes;
- Building inconsistencies of the Fcubic-DSP moulds together with the too coarse powder used for their production considerably affect the micro-replication capabilities of this process;
- The zirconia shells of Fcubic-DSP appear to be suitable for casting high melting point stainless steel alloy. Also, they show a lower reaction with the non-ferrous alloys, thus reducing the amount of micro-porosities present in the vicinity of the mould/metal interface;
- Although still more expensive than conventional LWP, Fcubic-DSP offers a considerable advantage in terms of lead-time;
- The solidification conditions of cast micro-features with thicknesses smaller than 1mm appear to be strongly dependent upon their AR rather than their sections, which is a major difference compared to that of conventional casting size;
- When casting micro-features, the mould pouring temperature is a parameter of even greater importance than at conventional casting size. It should be lowered as much as possible in order to get an optimum compromise between successful mould filling and the structural homogeneity of the casting;

- An empirical model describing the dendritic structural refinements observed in micro-features smaller than 500μm cast in LM25 was proposed as a function of the mould's pouring temperature and micro-features' AR;
- Finally, a relationship between the dendritic structural refinements of cast LM25 micro-features and the corresponding changes in the material hardness was found considering a Hall-Petch type equation form.

6.2. Further research directions

The work carried out in this thesis gave an overview of the potential that RP and IC could provide for the short run manufacture of high grade functional meso/micro metallic parts with complex geometries and high AR. At the same time, it covered different research directions that should be considered in order to further develop micro-casting and position this process as a serious contender in the industrial micro-manufacturing world. Additional work is still required in the following domains:

- By further analyzing the structural refinements of cast micro-features as a function of their AR and processing parameters, using different types of materials, it should be possible to develop models suitable for simulating the solidification conditions of cast micro-features;
- Work should also be done regarding the theory of gating systems so that micro-injected plastic parts could be directly implemented into the process, by conserving their original gating system;

- New investments, combining finer powders and having the possibility of being chemically dissolved need to be further developed;
- Considering the LWP process, issues regarding the flowability of the ceramic slurry onto the patterns have to be considered to prevent the apparition of casting surface defects originating from embedding problems;
- The influence of post-processing treatments on the resulting microstructure and subsequent enhancement of the micro-castings' mechanical properties should be addressed and compared to that of conventional casting size.

APPENDIX

Appendix 3.1
Measurement error of the QV system.

Steps number/Magnification	1 to 2	3 to 7	8 to 10
Magnification used	**x6**	**x2**	**x1**
Measurements	Step 1	Step 5	Step 8
1	0.1721	0.7233	2.4992
2	0.1732	0.7190	2.5031
3	0.1726	0.7237	2.4907
4	0.1739	0.7233	2.5058
5	0.1739	0.7175	2.4990
6	0.1739	0.7222	2.5153
7	0.1752	0.7149	2.4904
8	0.1738	0.7202	2.5066
9	0.1740	0.7186	2.5009
10	0.1737	0.7184	2.5011
Average step dimension	0.1736	0.7201	2.5012
Standard deviation*	0.0008	0.0029	0.0074
Pattern tolerance**	0.009	0.036	0.125
Measurement error (%)	9.74	8.18	5.89

*: characterize the measurement variability
**: arbitrarily taken as 5% of the average step dimension

$$Measurement \cdot Error = \frac{Measurement \cdot Variability}{Pattern \cdot Tolerance} * 100$$

Appendix 3.2

Shapiro-Wilk test for Normality.

Step Nom. (mm)		0.15	0.22	0.34	0.50	0.76	1.14	1.70	2.56	3.83
Shapiro-Wilk		**Steps Linear Dimension ThermoJet**								
LM25	P value	0.6559	0.5730	0.0489	0.6830	0.8216	0.5987	0.2795	0.2157	0.3018
	Sign.	**NO**	**NO**	**YES**	**NO**	**NO**	**NO**	**NO**	**NO**	**NO**
ZA12	P value	0.9628	0.7162	0.1243	0.9122	0.1315	0.7464	0.0948	0.6077	0.7724
	Sign.	**NO**	**NO**	**NO**	**NO**	**NO**	**NO**	**NO**	**NO**	**NO**

Step Nom. (mm)		0.15	0.22	0.34	0.50	0.76	1.14	1.70	2.56	3.83
Shapiro-Wilk		**Steps relative angular deviation ThermoJet**								
LM25	P value	0.2377	0.5259	0.5747	0.7895	0.7099	0.7601	0.9370	0.8632	0.6711
	Sign.	**NO**	**NO**	**NO**	**NO**	**NO**	**NO**	**NO**	**NO**	**NO**
ZA12	P value	0.1195	0.9784	0.2835	0.2340	0.5349	0.9309	0.3957	0.1473	0.3310
	Sign.	**NO**	**NO**	**NO**	**NO**	**NO**	**NO**	**NO**	**NO**	**NO**

Edges		E1 (Tip)	E2	E3	E4	E5	E6	E7	E8	E9	E10 (Base)
Shapiro-Wilk		**Edge Straightness ThermoJet**									
LM25	P value	0.6122	0.1759	0.0147	0.3127	0.5934	0.7499	0.2765	0.6896	0.1419	0.0378
	Sign.	**NO**	**NO**	**YES**	**NO**	**NO**	**NO**	**NO**	**NO**	**NO**	**YES**
ZA12	P value	0.4047	0.5136	0.4678	0.7036	0.0732	0.7835	0.3117	0.3383	0.1263	0.7064
	Sign.	**NO**	**NO**	**NO**	**NO**	**NO**	**NO**	**NO**	**NO**	**NO**	**NO**

Step Nom. (mm)		0.15	0.22	0.34	0.50	0.76	1.14	1.70	2.56	3.83
Shapiro-Wilk		**Steps Linear Dimension PatternMaster**								
LM25	P value	0.9272	0.1718	0.3322	0.2835	0.6674	0.8713	0.1692	0.0305	0.0785
	Sign.	**NO**	**NO**	**NO**	**NO**	**NO**	**NO**	**NO**	**YES**	**NO**
ZA12	P value	0.5721	0.0194	0.0648	0.5897	0.8238	0.2690	0.7110	0.4167	0.0184
	Sign.	**NO**	**YES**	**NO**	**NO**	**NO**	**NO**	**NO**	**NO**	**YES**

Step Nom. (mm)		0.15	0.22	0.34	0.50	0.76	1.14	1.70	2.56	3.83
Shapiro-Wilk		**Steps relative angular deviation PatternMaster**								
LM25	P value	0.9639	0.8667	0.0745	0.4560	0.1945	0.2906	0.3683	0.8930	0.1443
	Sign.	**NO**	**NO**	**NO**	**NO**	**NO**	**NO**	**NO**	**NO**	**NO**
ZA12	P value	0.5070	0.8806	0.9162	0.2597	0.3569	0.3175	0.3742	0.8637	0.5801
	Sign.	**NO**	**NO**	**NO**	**NO**	**NO**	**NO**	**NO**	**NO**	**NO**

Edges		E1	E2	E3	E4	E5	E6	E7	E8	E9	E10
Shapiro-Wilk		**Edge Straightness of PatternMaster samples**									
LM25	P value	0.1752	0.6455	0.5316	0.3807	0.4783	0.2093	0.2265	0.8210	0.1369	0.3801
	Sign.	**NO**	**NO**	**NO**	**NO**	**NO**	**NO**	**NO**	**NO**	**NO**	**NO**
ZA12	P value	0.0161	0.4356	0.8418	0.5088	0.0049	0.6218	0.4617	0.7661	0.2292	0.9516
	Sign.	**YES**	**NO**	**NO**	**NO**	**YES**	**NO**	**NO**	**NO**	**NO**	**NO**

Appendix 3.3

Result of the Paired t-test statistical analysis.

Step Nom. (mm)		0.15	0.22	0.34	0.50	0.76	1.14	1.70	2.56	3.83
Paired t-test		**Steps Linear Dimension ThermoJet**								
LM25	2-tailed p	0.0431	0.2848	0.2405	0.0540	0.0981	0.0474	0.2789	0.0001	0.0001
	Sign.	**YES**	**NO**	**NO**	**NO**	**NO**	**YES**	**NO**	**YES**	**YES**
SD Al	2-tailed p	0.2776	0.1950	0.5700	0.9791	0.7084	0.1158	0.0383	0.0100	0.4887
	Sign.	**NO**	**NO**	**NO**	**NO**	**NO**	**NO**	**YES**	**YES**	**NO**
ZA12	2-tailed p	0.0515	0.1376	0.2931	0.7091	0.1438	0.4697	0.5748	0.0002	0.0003
	Sign.	**NO**	**NO**	**NO**	**NO**	**NO**	**NO**	**NO**	**YES**	**YES**
SD Zn	2-tailed p	0.4648	0.5300	0.4008	0.1822	0.5767	0.0246	0.5648	0.0231	0.5228
	Sign.	**NO**	**NO**	**NO**	**NO**	**NO**	**YES**	**NO**	**YES**	**NO**

Step Nom. (mm)		0.15	0.22	0.34	0.50	0.76	1.14	1.70	2.56	3.83
Paired t-test		**Steps relative angular deviation ThermoJet**								
LM25	2-tailed p	0.6676	0.8853	0.0886	0.5773	0.1562	0.9541	0.6153	0.0893	0.0902
	Sign.	**NO**	**NO**	**NO**	**NO**	**NO**	**NO**	**NO**	**NO**	**NO**
SD Al	2-tailed p	0.9713	0.0538	0.6822	0.7003	0.7830	0.9115	0.0465	0.1279	0.2850
	Sign.	**NO**	**NO**	**NO**	**NO**	**NO**	**NO**	**YES**	**NO**	**NO**
ZA12	2-tailed p	0.6766	0.4928	0.4264	0.9059	0.8283	0.2862	0.051	0.9206	0.8601
	Sign.	**NO**	**NO**	**NO**	**NO**	**NO**	**NO**	**NO**	**NO**	**NO**
SD Zn	2-tailed p	0.0560	0.7828	0.9131	0.8805	0.5190	0.7124	0.0358	0.3304	0.0846
	Sign.	**NO**	**NO**	**NO**	**NO**	**NO**	**NO**	**YES**	**NO**	**NO**

Edges		E1 (Tip)	E2	E3	E4	E5	E6	E7	E8	E9	E10 (Base)
Paired t-test		**Edge Straightness ThermoJet**									
LM25	2-tailed p	0.2979	0.6792	0.6078	0.6807	0.7593	0.7707	0.9257	0.5677	0.1914	0.3569
	Sign.	**NO**	**NO**	**NO**	**NO**	**NO**	**NO**	**NO**	**NO**	**NO**	**NO**
SD Al	2-tailed p	0.1143	0.2313	0.5753	0.3644	0.1983	0.9888	0.9717	0.7437	0.7150	0.9499
	Sign.	**NO**	**NO**	**NO**	**NO**	**NO**	**NO**	**NO**	**NO**	**NO**	**NO**
ZA12	2-tailed p	0.4374	0.7989	0.9271	0.3850	0.6620	0.6202	0.8802	0.3746	0.7510	0.1950
	Sign.	**NO**	**NO**	**NO**	**NO**	**NO**	**NO**	**NO**	**NO**	**NO**	**NO**
SD Zn	2-tailed p	0.6942	0.3910	0.0581	0.6309	0.8153	0.9533	0.5325	0.9815	0.1534	0.1792
	Sign.	**NO**	**NO**	**NO**	**NO**	**NO**	**NO**	**NO**	**NO**	**NO**	**NO**

Appendix A3.3

Result of the Paired t-test statistical analysis.

Step Nom. (mm)		0.15	0.22	0.34	0.50	0.76	1.14	1.70	2.56	3.83
Paired t-test		**Steps Linear Dimension PatternMaster**								
LM25	2-tailed p	0.0373	0.3340	0.1345	0.0576	0.0988	0.0333	0.0947	0.0001	0.0002
	Sign.	**YES**	**NO**	**NO**	**NO**	**NO**	**YES**	**NO**	**YES**	**YES**
SD Al	2-tailed p	0.2468	0.8488	0.9233	0.4565	0.4007	0.4137	0.0804	0.4321	0.3398
	Sign.	**NO**	**NO**	**NO**	**NO**	**NO**	**NO**	**NO**	**NO**	**NO**
ZA12	2-tailed p	0.0412	0.7726	0.6704	0.0516	0.0747	0.043	0.0475	0.0001	0.0001
	Sign.	**YES**	**NO**	**NO**	**NO**	**NO**	**YES**	**YES**	**YES**	**YES**
SD Zn	2-tailed p	0.2256	0.4200	0.4088	0.5588	0.8274	0.9291	0.3969	0.2728	0.9378
	Sign.	**NO**	**NO**	**NO**	**NO**	**NO**	**NO**	**NO**	**NO**	**NO**

Step Nom. (mm)		0.15	0.22	0.34	0.50	0.76	1.14	1.70	2.56	3.83
Paired t-test		**Steps relative angular deviation PatternMaster**								
LM25	2-tailed p	0.4759	0.2207	0.6206	0.5330	0.3723	0.6115	0.9969	0.7502	0.2780
	Sign.	**NO**	**NO**	**NO**	**NO**	**NO**	**NO**	**NO**	**NO**	**NO**
SD Al	2-tailed p	0.7873	0.7241	0.6904	0.0662	0.4500	0.8549	0.6430	0.5522	0.8610
	Sign.	**NO**	**NO**	**NO**	**NO**	**NO**	**NO**	**NO**	**NO**	**NO**
ZA12	2-tailed p	0.3117	0.5004	0.7086	0.6388	0.3676	0.2830	0.8436	0.5352	0.4248
	Sign.	**NO**	**NO**	**NO**	**NO**	**NO**	**NO**	**NO**	**NO**	**NO**
SD Zn	2-tailed p	0.6830	0.6107	0.8748	0.1629	0.7050	0.8809	0.6918	0.4104	0.6074
	Sign.	**NO**	**NO**	**NO**	**NO**	**NO**	**NO**	**NO**	**NO**	**NO**

Edges		E1	E2	E3	E4	E5	E6	E7	E8	E9	E10
Paired t-test		**Edge Straightness PatternMaster**									
LM25	2-tailed p	0.0405	0.3951	0.9032	0.6961	0.5609	0.0233	0.1983	0.0815	0.9526	0.1372
	Sign.	**YES**	**NO**	**NO**	**NO**	**NO**	**YES**	**NO**	**NO**	**NO**	**NO**
SD Al	2-tailed p	0.6985	0.1736	0.6039	0.7442	0.7468	0.4414	0.9074	0.7916	0.7007	0.5151
	Sign.	**NO**	**NO**	**NO**	**NO**	**NO**	**NO**	**NO**	**NO**	**NO**	**NO**
ZA12	2-tailed p	0.1405	0.9367	0.1960	0.9331	0.4242	0.6047	0.9888	0.1269	0.0999	0.5220
	Sign.	**NO**	**NO**	**NO**	**NO**	**NO**	**NO**	**NO**	**NO**	**NO**	**NO**
SD Zn	2-tailed p	0.3641	0.8993	0.6802	0.1751	0.4260	0.6644	0.9774	0.6602	0.3393	0.7209
	Sign.	**NO**	**NO**	**NO**	**NO**	**NO**	**NO**	**NO**	**NO**	**NO**	**NO**

Appendix A4.1.

Tables used for the PI's calculation of the LD.

LD Accuracy		Al ThJ		Zn ThJ		Al DSP		Zn DSP		Al PM		Zn PM	
		Abs Dev.	PI	Abs Dev.	PI	Abs Dev.	PI	Abs Dev.	PI	Abs Dev.	PI	Abs Dev.	PI
Smallest	Steps												
0.014	0.15	0.027	**52**	0.024	**60**	0.037	**39**	0.020	**71**	0.014	**100**	0.017	**82**
0.011	0.22	0.038	**30**	0.012	**96**	0.013	**85**	0.022	**52**	0.015	**75**	0.011	**100**
0.010	0.34	0.020	**53**	0.021	**50**	0.042	**25**	0.035	**30**	0.013	**78**	0.010	**100**
0.010	0.5	0.016	**64**	0.010	**99**	0.027	**38**	0.011	**89**	0.012	**87**	0.010	**100**
0.005	0.76	0.035	**15**	0.020	**27**	0.053	**10**	0.005	**100**	0.016	**33**	0.016	**33**
0.001	1.14	0.015	**10**	0.015	**10**	0.034	**4**	0.001	**100**	0.018	**8**	0.024	**6**
0.016	1.7	0.058	**28**	0.016	**100**	0.062	**26**	0.020	**83**	0.037	**45**	0.031	**53**
0.024	2.56	0.041	**59**	0.054	**44**	0.024	**99**	0.026	**94**	0.024	**100**	0.030	**81**
0.018	3.83	0.040	**46**	0.018	**100**	0.036	**52**	0.101	**18**	0.079	**23**	0.099	**19**

This table shows the calculation of the PI for each technology and alloy based on the average LD value measured on the Pyramids.

LD Consistency		Al ThJ		Zn ThJ		Al DSP		Zn DSP		Al PM		Zn PM	
		Abs Dev.	PI	Abs Dev.	PI	Abs Dev.	PI	Abs Dev.	PI	Abs Dev.	PI	Abs Dev.	PI
Smallest	Steps												
0.006	0.15	0.025	**24**	0.027	**22**	0.051	**12**	0.040	**15**	0.006	**100**	0.013	**45**
0.009	0.22	0.027	**34**	0.024	**37**	0.026	**35**	0.062	**15**	0.009	**99**	0.009	**100**
0.010	0.34	0.027	**37**	0.012	**82**	0.063	**16**	0.041	**24**	0.010	**100**	0.011	**91**
0.008	0.5	0.022	**36**	0.029	**27**	0.035	**22**	0.031	**25**	0.010	**78**	0.008	**100**
0.007	0.76	0.017	**44**	0.019	**39**	0.070	**11**	0.027	**28**	0.007	**100**	0.015	**48**
0.010	1.14	0.021	**46**	0.020	**48**	0.070	**14**	0.037	**26**	0.010	**100**	0.011	**87**
0.008	1.7	0.035	**24**	0.035	**24**	0.056	**15**	0.032	**27**	0.021	**41**	0.008	**100**
0.020	2.56	0.026	**77**	0.024	**82**	0.033	**61**	0.040	**50**	0.020	**100**	0.022	**89**
0.025	3.83	0.025	**100**	0.036	**69**	0.052	**48**	0.050	**50**	0.040	**62**	0.056	**45**

This table shows the calculation of the PI for each technology and alloy based on the SD of the LD measurements performed on the Pyramids.

Targeted dimension (mm)		0.15	0.22	0.34	0.50	0.76	1.14	1.70	2.56	3.83
Sum accuracy	**ThJ**	112	126	103	163	42	19	128	103	146
	DSP	109	138	55	127	110	104	109	193	70
	PM	182	175	178	187	65	14	98	181	42
Sum consistency	**ThJ**	45	71	119	62	83	94	48	159	169
	DSP	26	50	39	47	38	40	42	111	99
	PM	145	199	191	178	148	187	141	189	108

Cumulative PI displayed on the bar charts.

Appendix A4.1.

Tables used for the PI's calculation of the RAD.

RAD		Al ThJ		Zn ThJ		Al DSP		Zn DSP		Al PM		Zn PM	
Accuracy		Av.	PI	Av.	PI	Av.	PI	Av.	PI	Av.	PI	Av.	PI
Smallest	Steps												
0.53	0.15	0.638	**82**	1.132	**46**	3.905	**13**	1.484	**35**	0.61	**87**	0.53	**100**
0.20	0.22	2.094	**9**	0.233	**85**	1.099	**18**	2.739	**7**	0.59	**34**	0.20	**100**
0.05	0.34	0.274	**19**	0.603	**9**	2.464	**2**	0.896	**6**	0.37	**15**	0.05	**100**
0.17	0.5	0.402	**43**	0.175	**100**	1.128	**16**	1.047	**17**	0.18	**96**	0.24	**72**
0.01	0.76	0.211	**3**	0.109	**7**	0.939	**1**	0.218	**3**	0.01	**100**	0.25	**3**
0.05	1.14	0.308	**16**	0.078	**61**	0.713	**7**	0.505	**9**	0.05	**100**	0.34	**14**
0.06	1.7	0.097	**67**	0.239	**27**	1.244	**5**	0.464	**14**	0.06	**100**	0.20	**32**
0.07	2.56	0.259	**27**	0.637	**11**	0.793	**9**	0.355	**19**	0.10	**69**	0.07	**100**
0.70	3.83	0.902	**78**	1.49	**47**	0.705	**100**	1.155	**61**	0.78	**90**	1.18	**60**

This table shows the calculation of the PI for each technology and alloy based on the average RAD measured on the Pyramids.

RAD		Al ThJ		Zn ThJ		Al DSP		Zn DSP		Al PM		Zn PM	
Consistency		Av.	PI	Av.	PI	Av.	PI	Av.	PI	Av.	PI	Av.	PI
Smallest	Steps												
0.75	0.15	1.711	**44**	1.526	**49**	2.267	**33**	1.580	**47**	0.75	**100**	1.22	**61**
0.63	0.22	0.973	**64**	1.683	**37**	3.744	**17**	2.425	**26**	0.63	**100**	0.65	**96**
0.45	0.34	0.814	**55**	0.447	**100**	3.438	**13**	2.808	**16**	0.74	**60**	0.53	**85**
0.39	0.5	0.447	**88**	0.444	**89**	2.458	**16**	1.585	**25**	0.52	**75**	0.39	**100**
0.33	0.76	0.409	**81**	0.452	**73**	1.848	**18**	0.804	**41**	0.35	**95**	0.33	**100**
0.24	1.14	0.266	**89**	0.476	**50**	1.784	**13**	1.312	**18**	0.24	**100**	0.49	**48**
0.25	1.7	0.26	**97**	0.508	**50**	2.001	**13**	1.142	**22**	0.25	**100**	0.25	**99**
0.18	2.56	0.209	**85**	0.458	**39**	2.132	**8**	1.091	**16**	0.18	**100**	0.31	**57**
0.31	3.83	0.314	**100**	1.064	**29**	0.731	**43**	1.473	**21**	0.36	**87**	0.92	**34**

This table shows the calculation of the PI for each technology and alloy based on the SD of the RAD measurements performed on the Pyramids.

Targeted dimension		0.15	0.22	0.34	0.50	0.76	1.14	1.70	2.56	3.83
Sum accuracy	**ThJ**	129	95	28	143	10	77	94	38	125
	DSP	49	25	8	32	4	16	19	28	161
	PM	187	134	115	169	103	114	132	169	149
Sum consistency	**ThJ**	92	102	155	177	153	138	146	124	129
	DSP	80	43	29	41	59	31	35	25	64
	PM	161	196	145	175	195	148	199	157	121

Cumulative PI displayed on the bar charts.

Appendix A4.1.

Tables used for the PI's calculation of the ES.

ES		Al ThJ		Zn ThJ		Al DSP		Zn DSP		Al PM		Zn PM	
Accuracy		Av.	PI	Av.	PI	Av.	PI	Av.	PI	Av.	PI	Av.	PI
Smallest	Edges												
0.015	E1	0.028	**54**	0.026	**60**	0.016	**94**	0.024	**65**	0.015	**100**	0.022	**72**
0.022	E2	0.034	**66**	0.022	**100**	0.031	**72**	0.030	**75**	0.023	**98**	0.026	**84**
0.021	E3	0.035	**62**	0.021	**100**	0.033	**65**	0.025	**86**	0.025	**86**	0.03	**71**
0.025	E4	0.025	**100**	0.028	**90**	0.045	**55**	0.037	**67**	0.034	**73**	0.026	**95**
0.026	E5	0.026	**100**	0.027	**96**	0.046	**57**	0.053	**49**	0.038	**68**	0.033	**78**
0.024	E6	0.033	**73**	0.024	**100**	0.065	**38**	0.047	**52**	0.030	**81**	0.037	**66**
0.028	E7	0.032	**86**	0.028	**100**	0.059	**47**	0.054	**52**	0.030	**92**	0.034	**81**
0.022	E8	0.023	**95**	0.032	**68**	0.064	**34**	0.045	**50**	0.022	**100**	0.025	**87**
0.029	E9	0.035	**81**	0.029	**100**	0.048	**61**	0.058	**50**	0.038	**76**	0.03	**95**
0.046	E10	0.064	**72**	0.046	**100**	0.062	**74**	0.049	**93**	0.095	**48**	0.122	**38**

This table shows the calculation of the PI for each technology and alloy based on the average ES measured on the Pyramids.

ES		Al ThJ		Zn ThJ		Al DSP		Zn DSP		Al PM		Zn PM	
Consistency		Av.	PI	Av.	PI	Av.	PI	Av.	PI	Av.	PI	Av.	PI
Smallest	Edges												
0.005	E1	0.017	**33**	0.014	**38**	0.018	**30**	0.005	**100**	0.006	**92**	0.012	**47**
0.006	E2	0.013	**47**	0.009	**65**	0.013	**45**	0.008	**80**	0.006	**100**	0.012	**52**
0.008	E3	0.020	**39**	0.008	**100**	0.022	**36**	0.013	**60**	0.009	**83**	0.015	**53**
0.008	E4	0.011	**70**	0.008	**100**	0.017	**45**	0.019	**41**	0.018	**43**	0.014	**55**
0.005	E5	0.007	**64**	0.011	**41**	0.014	**33**	0.005	**100**	0.012	**37**	0.017	**27**
0.005	E6	0.024	**21**	0.005	**100**	0.019	**27**	0.013	**37**	0.018	**28**	0.027	**19**
0.010	E7	0.016	**59**	0.010	**100**	0.016	**62**	0.011	**90**	0.015	**63**	0.014	**68**
0.008	E8	0.011	**77**	0.011	**76**	0.025	**33**	0.008	**100**	0.012	**70**	0.009	**95**
0.006	E9	0.012	**50**	0.006	**100**	0.015	**38**	0.022	**27**	0.020	**29**	0.016	**36**
0.016	E10	0.025	**65**	0.016	**100**	0.021	**75**	0.029	**54**	0.058	**28**	0.068	**24**

This table shows the calculation of the PI for each technology and alloy based on the SD of the ES measurements performed on the Pyramids.

Observed Edges		E1 (tip)	E2	E3	E4	E5	E6	E7	E8	E9	E10 (base)
Sum accuracy	**ThJ**	114	166	162	190	196	173	186	164	181	172
	DSP	159	147	151	122	106	89	98	84	110	167
	PM	172	182	157	167	147	147	173	187	172	86
Sum consistency	**ThJ**	71	113	139	170	105	121	159	154	150	165
	DSP	130	125	96	86	133	64	152	133	65	129
	PM	140	152	136	98	64	47	131	166	65	51

Cumulative PI displayed on the bar charts.

Appendix A4.1.

Tables used for the PI's calculation of the Roughness.

Roughness Accuracy		Al ThJ		Zn ThJ		Al DSP		Zn DSP		Al PM		Zn PM	
		Ra											
Smallest	Dir.	Av.	PI	Av.	PI	Av.	PI	Av.	PI	Av.	PI	Av.	PI
2.50	Z	2.7	**93**	2.5	**100**	5.4	**46**	6.2	**40**	4.5	**56**	5.3	**47**
1.94	X and Y	2.0	**96**	1.9	**100**	6.2	**31**	5.3	**36**	2.5	**77**	2.7	**71**
0.76	Top	1.0	**77**	2.0	**38**	4.7	**16**	5.5	**14**	0.8	**100**	1.2	**64**
		Rz											
Smallest	Dir.	Av.	PI	Av.	PI	Av.	PI	Av.	PI	Av.	PI	Av.	PI
12.45	Z	13.4	**93**	12.5	**100**	24.4	**51**	29.4	**42**	23.3	**53**	26.6	**47**
9.74	X and Y	9.9	**98**	9.7	**100**	28.0	**35**	25.9	**38**	14.4	**68**	14.5	**67**
5.05	Top	6.1	**83**	12.3	**41**	23.4	**22**	26.5	**19**	5.1	**100**	7.9	**64**

This table shows the calculation of the PI for each technology and alloy based on the average roughness measured on the Pyramids.

Roughness Consistency		Al ThJ		Zn ThJ		Al DSP		Zn DSP		Al PM		Zn PM	
		Ra											
Smallest	Dir.	Av.	PI	Av.	PI	Av.	PI	Av.	PI	Av.	PI	Av.	PI
0.55	Z	0.8	**65**	0.5	**100**	1.3	**43**	0.9	**61**	0.9	**59**	1.7	**33**
0.44	X and Y	0.4	**100**	0.7	**63**	0.6	**74**	0.8	**57**	0.9	**47**	1.0	**45**
0.12	Top	0.2	**51**	0.6	**19**	1.0	**13**	2.0	**6**	0.1	**100**	0.2	**75**
		Rz											
Smallest	Dir.	Av.	PI	Av.	PI	Av.	PI	Av.	PI	Av.	PI	Av.	PI
1.97	Z	3.3	**60**	2.0	**100**	5.2	**38**	2.4	**82**	3.8	**51**	6.4	**31**
3.09	X and Y	3.2	**98**	3.1	**100**	3.4	**91**	3.2	**96**	3.8	**81**	4.2	**74**
1.03	Top	1.9	**55**	3.1	**33**	3.7	**28**	7.3	**14**	1.0	**100**	1.1	**94**

This table shows the calculation of the PI for each technology and alloy based on the SD of the roughness measurements performed on the Pyramids.

Measurement direction		Z	X and Y	Top	Z	X and Y	Top
Roughness (µm)			Ra			Rz	
Sum accuracy	**ThJ**	193	196	115	193	198	124
	DSP	86	68	30	93	72	41
	PM	103	148	164	100	135	164
Sum consistency	**ThJ**	165	163	70	160	198	87
	DSP	104	131	19	120	187	42
	PM	91	91	175	82	155	194

Cumulative PI displayed on the bar charts.

Appendix 5.1

Calculation of the average DCS and SD of the ribs' dimensional group 0.5-0.25mm used for the Monte Carlo data simulation based on the average DCS values and respective SD of each group of rib's thicknesses cast with a mould temperature of 450°C.

	Mould 450°C												Dimensional group 0.5-0.25mm	
Rib	1mm		0.75mm		0.5mm		0.45mm		0.3mm		0.25mm			
	DCS	SD	DCS	SD	DCS	SD	DCS	SD	DCS	SD	DCS	SD	DCS	Ave. SD
AR														
0	31.7	5.3	28.3	6.5	26.5	4.3	27.7	6.7					27.1	2.60
1	27.3	5.6	25.0	4.3										
2	25.2	4.0			25.1	3.8	23.5	4.4					24.3	
3	24.3	3.9	20.5	3.6										
4	25.4	5.5	18.8		22.8	3.1	20.3	3.2					21.5	
5	23.4	3.8	19.9											
6					19.9	3.4							19.9	
7	23.3	4.3	16.6	3.6			17.8	3.3					17.8	
8					19.1	3.0							19.1	
9			16.4	3.6			16.6	1.8					16.6	
10	20.9	4.4			16.5	3.6							16.5	
11							14.3	3.8					14.3	
12					14.9	3.1							14.9	
13			15.2	3.6			13.2	4.3					13.2	
14					13.6	2.7							13.6	
15	20.3	5.3												
16			13.4	3.3	13.7	3.4	11.5	1.9					12.6	
17									13.1	2.6			13.1	
18					12.3	3.6	10.9	2.0					11.6	
19														
20	19.3	2.9	14.4	2.4	11.6	2.4	10.2	1.7	11.7	2.8	12.9	2.9	11.6	
21														
22							9.4	1.8					9.4	
23			11.8	2.9					12.0	2.8			12.0	
24					11.8	2.2					10.9	2.6	11.3	
25	18.3	4.3												
26					11.1	2.0							11.1	
27			13.6	4.0			9.1	2.2	10.9	2.5			10.0	
28					11.2	1.9					10.3	2.4	10.7	
29							8.6	2.3					8.6	
30	19.9	4.5			11.0	2.1			9.9	2.3			10.4	
31														
32											10.3	2.1	10.3	
33			12.5	2.8			9.6	2.3	10.2	2.4			9.9	
34														
35	19.8	5.8												
36					10.4	2.0					9.9	3.2	10.2	
37									9.8	2.3			9.8	
38														
39														
40	18.3	4.7	10.9	2.6	10.7	2.1	8.0	1.4	8.7	2.0	8.6	1.6	9.0	
41														
42														
43									9.3	2.2			9.3	
44							8.3	1.7			8.4	1.7	8.3	
45	17.9	3.7												
46					10.0	2.4							10.0	
47			10.7	2.7					8.3	2.1			8.3	
48											7.2	1.3	7.2	
49														
50	14.6	4.1	9.9	2.1	8.7	2.4	8.5	1.4	8.1	1.6			8.4	

Appendix 5.1

Calculation of the average DCS and SD of the ribs' dimensional group 0.5-0.25mm used for the Monte Carlo data simulation based on the average DCS values and respective SD of each group of rib's thicknesses cast with a mould temperature of 250°C.

	Mould 250°C												Dimensional group 0.5-0.25mm	
Rib	1mm		0.75mm		0.5mm		0.45mm		0.3mm		0.25mm			
	DCS	SD	DCS	SD	DCS	SD	DCS	SD	DCS	SD	DCS	SD	DCS	Ave. SD
AR														
0	14.8	3.7	12.9	3.2	14.2	3.4	13.2	2.9	13.3	2.1	15.5	3.5	14.0	1.53
1	13.7	4.1	10.4	2.6										
2	13.9	1.7			12.9	2.8	10.8	1.8					11.9	
3	11.7	3.3	8.6	3.1					10.3	2.7			10.3	
4	10.9	2.2	9.7	2.0	10.5	2.0	8.3	2.1			10.4	2.6	9.7	
5	11.0	1.9	9.2	1.7										
6					8.2	2.0							8.2	
7	10.6	2.1	8.8	1.8			7.8	1.3	7.2	1.7			7.5	
8					8.1	1.9					7.4	1.7	7.8	
9			8.0	1.3			7.0	1.5					7.0	
10	9.8	2.3			7.9	2.0			7.0	1.3			7.4	
11							6.5	1.7					6.5	
12					6.8	1.3					6.6	1.3	6.7	
13			7.3	1.8			5.7	1.2	6.4	1.1			6.1	
14					6.5	2.5							6.5	
15	8.8	2.5												
16			7.2	1.2	6.2	1.5	5.4	1.5			5.5	1.3	5.7	
17									6.2	1.7			6.2	
18					6.3	1.5	5.4	1.2					5.8	
19														
20	8.3	2.1	7.7	1.8	5.8	1.2	5.6	1.2	5.7	1.2	5.3	1.2	5.6	
21														
22							5.8	1.9					5.8	
23			7.1	2.1					5.8	1.5			5.8	
24					6.1	1.2					5.5	1.3	5.8	
25	8.6	1.6												
26					6.1	1.1							6.1	
27			6.8	1.7			5.6	1.3	5.5	1.2			5.5	
28					6.1	1.8					5.3	1.2	5.7	
29							5.0	1.2					5.0	
30	8.4	2.2			5.3	1.3			5.4	1.2			5.4	
31														
32											4.8	1.3	4.8	
33			6.8	1.6			5.5	1.3	5.2	1.2			5.4	
34														
35	8.3	1.3												
36					5.7	0.9					5.4	1.2	5.5	
37									5.4	1.2			5.4	
38														
39														
40	8.1	1.7	6.8	1.5	5.0	1.0	5.3	1.1	5.3	1.0	6.0	1.4	5.4	
41														
42														
43									4.8	1.0			4.8	
44							4.6	1.1			5.0	1.2	4.8	
45	7.3	1.7												
46					5.1	1.3							5.1	
47			6.1	1.3					4.8	1.3			4.8	
48											5.2	0.8	5.2	
49														
50	7.1	1.6	6.0	1.4	4.6	1.0	4.1	1.0	4.7	1.2			4.5	

Appendix 5.2

Set of data generated with random scatter using the best fit parameters calculated from the regression analysis performed on the average DCS exhibited by the rib dimensional group 0.5-0.25mm and produced at $T_M = 250°C$. The random scatter was obtained by imputing a SD of 1.53 microns.

Mould 250°C					
SPAN	K	PLATEAU	SPAN	K	PLATEAU
10.51	0.176	4.909	7.601	0.1736	5.668
8.445	0.1586	4.929	9.539	0.1708	5.257
8.588	0.1568	5.348	8.116	0.1304	5.123
8.968	0.1387	4.558	9.866	0.1814	4.988
6.692	0.1121	4.968	10.2	0.1939	4.933
9.068	0.1311	4.585	9.618	0.1954	5.485
9.597	0.1494	4.951	6.265	0.1108	5.036
8.118	0.1279	5.452	8.426	0.1962	5.061
8.093	0.12	5.253	9.337	0.158	5.157
8.249	0.1476	4.815	9.817	0.1537	5.404
9.44	0.151	4.77	9.091	0.1273	5.243
8.206	0.1547	5.469	11.68	0.2619	5.301
8.543	0.1666	5.171	10.41	0.2415	5.695
8.87	0.1788	5.581	7.992	0.1514	5.408
8.233	0.2078	5.6	8.805	0.1587	5.474
7.899	0.2102	5.514	10.55	0.1454	5.054
8.421	0.1114	4.45	10.8	0.2415	5.752
8.441	0.2174	5.476	6.78	0.103	5.193
9.077	0.1191	4.657	9.519	0.2519	5.37
10.51	0.1568	4.956	8.938	0.1366	5.046
8.588	0.21	5.636	7.955	0.1682	4.907
7.107	0.1439	5.042	10.16	0.1868	4.909
9.772	0.1305	4.637	9.327	0.1313	4.746
8.318	0.1563	5.273	7.284	0.157	4.817
10.35	0.158	5.146	10.37	0.2611	5.462

	SPAN	K	PLATEAU
α	0.05	0.05	0.05
SD	1.156	0.040	0.327
n	50	50	50
95% CI	**0.3203**	**0.0111**	**0.0907**

Appendix 5.2

Set of data generated with random scatter using the best fit parameters calculated from the regression analysis performed on the average DCS exhibited by the rib dimensional group 0.5-0.25mm and produced at $T_M = 450°C$. The random scatter was obtained by imputing a SD of 2.6 microns.

Mould 450°C					
SPAN	K	PLATEAU	SPAN	K	PLATEAU
19.03	0.1096	9.706	19.03	0.07841	7.659
19.98	0.07676	6.781	15.98	0.07944	8.308
16.14	0.0908	9.212	17.49	0.08614	8.843
18.22	0.07418	8.002	18.75	0.08581	8.605
18.2	0.1085	8.994	19.29	0.08244	8.102
19.8	0.05553	5.773	20.35	0.1006	8.477
19.05	0.09894	8.873	18.25	0.1026	8.554
17.54	0.08249	8.499	17.13	0.09676	9.267
19.35	0.09558	8.621	17.23	0.07796	8.372
19.75	0.08994	8.187	18.12	0.07714	7.506
16.18	0.07888	8.871	20.65	0.1091	8.99
19.63	0.08376	7.575	18.87	0.07045	7.591
19.27	0.05961	7.043	18.9	0.09121	8.622
17.76	0.07829	7.907	17.2	0.08594	8.829
19.42	0.103	8.727	18.62	0.09962	8.69
18.53	0.07664	8.627	20.67	0.1149	9.344
19.27	0.07293	7.568	21.59	0.09941	8.742
19.4	0.08877	8.408	18.87	0.09737	9.015
18.8	0.1297	9.268	19.45	0.1009	8.191
20.25	0.08664	8.043	19.78	0.1117	8.819
18.25	0.09608	8.934	19.19	0.0993	8.587
20.35	0.09664	8.617	21.59	0.1087	8.621
22.71	0.1095	8.989	18.92	0.1406	9.588
19.32	0.07713	7.132	19.86	0.09317	8.391
17.13	0.08649	8.714	20.98	0.08322	7.549

	SPAN	K	PLATEAU
α	0.05	0.05	0.05
SD	1.392	0.016	0.748
n	50	50	50
95% CI	**0.3859**	**0.0045**	**0.2074**

Appendix 5.3

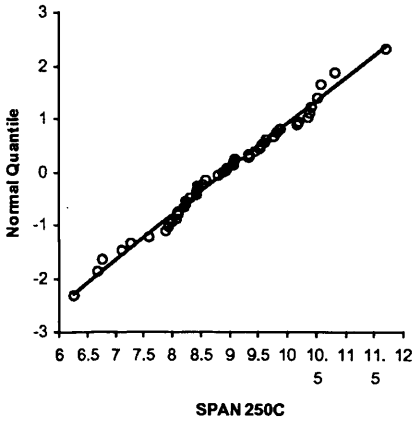

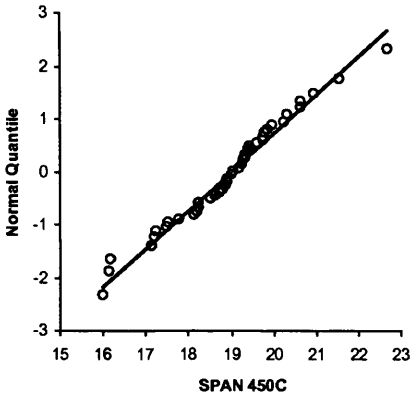

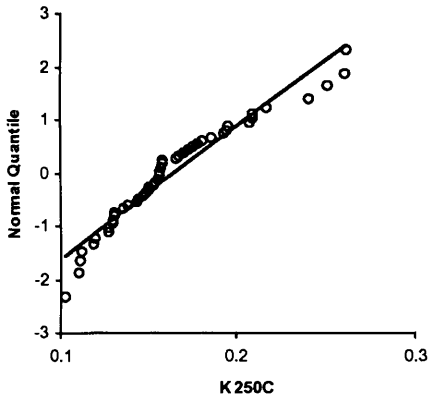

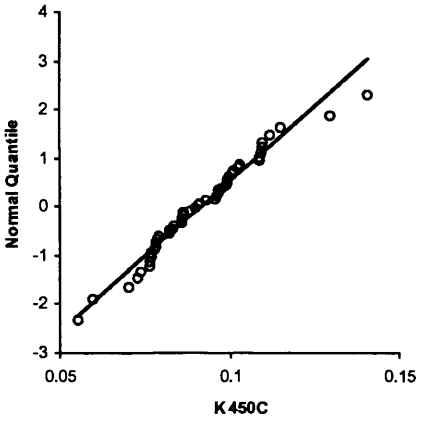

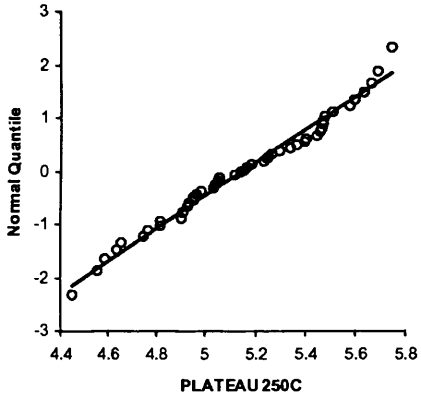

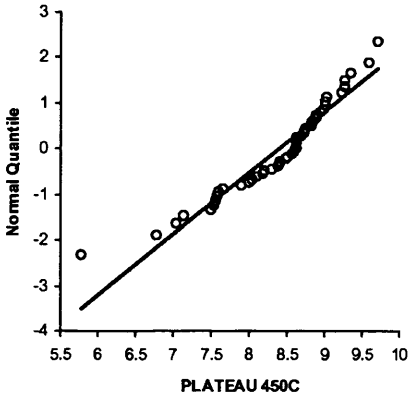

P-values	Span	K	Plateau
250°C	0.8653	0.0069	0.4934
450°C	0.5886	0.250	0.0037

P-values from the Shapiro-Wilk test performed on the model parameters. (α=0.05)

REFERENCES

Alting, L.,Kimura, F.,Hansen, H. N.,Bissacco, G. 2003. Micro Engineering. *Micro Engineering* 40(6), pp. 1-23.

Apelian, D., Shivkumar, S., Sigworth, G. K. 1990. Fundamental Aspects of Heat Treatment of Cast Al-Si-Mg Alloys. *AFS Transactions* 97, pp. 727-742.

Ashley, S. 1995. Rapid prototyping is coming of age. *Mechanical Engineering* 117(7), pp. 62-68.

Bassoli, E., Gatto, A., Luliano, L., Violante, M. G. 2007. 3D printing technique applied to rapid casting *Rapid Prototyping Journal* 13(3), pp. 148-155.

Baumeister, G., Ruprecht, R. 2002. Production of metallic high aspect ratio microstructures by microcasting. *Microsystem Technologies* 8, pp. 105-108.

Baumeister, G., Ruprecht, R., Hausselt, J. 2004, a. Microcasting of parts made of metal alloys. *Microsystem Technologies* 10, pp. 261-264.

Baumeister, G., Ruprecht, R., Hausselt, J. 2004, b. Replication of LIGA structures using microcasting. *Microsystem Technologies* 10, pp. 484-488.

Beeley, P. R. 1972. *Foundry technology*. London: Butterworths.

Bernard, A., Delplace, J.-C., Perry, N., Gabriel, S. 2003. Integration of CAD and rapid manufacturing for sand casting optimisation *Rapid Prototyping Journal* 9(5), pp. 327-333.

Berry, J. T. 1970. Effect of Solidification Conditions on Mechanical Behavior of Al Cast Alloys. *AFS Transactions* 78, pp. 421-428.

Brick, R. M., Gordon, R. B., Arthur, P. 1965. *Structure and properties of alloys : the application of phase diagrams to the interpretation and control of industrial alloy structures*. 3rd ed. New York: McGraw-Hill.

Brusethaug, S., Langsrud, Y. 2000. Aluminium properties, a model for calculating mechanical properties in AlSiMgFe-foundry alloys. *Metallurgical Science and Technology* 18(1), pp. 3-7.

Cáceres, C. H., Davidson, C.J. 1999. The Effect of Mg on the Microstructure and Mechanical Behavior of Al-Si-Mg Casting Alloys. *Metallurgical and Materials Transactions A* 30, pp. 2611-2618.

Cáceres, C. H., Griffiths, J. R. 1996. Damage by the cracking of silicon particles in an Al-7Si-0.4Mg casting alloy. *Acta Materialia* 44(1), pp. 25-33.

Cáceres, C. H., Griffiths, J. R., Reiner, P. 1996. The influence of microstructure on the Bauschinger effect in an Al---Si---Mg casting alloy. *Acta Materialia* 44(1), pp. 15-23.

Cáceres, C. H., Svensson, I. L., Taylor, J. A. 2002. Microstructural Factors and the Mechanical

Performance of Al-Si-Mg and Al-Si-Cu-Mg casting Alloys. *Proceedings from the 2nd International Aluminium Casting Technology Symposium, Columbus, OH, ASM International*, pp. 49-57.

Cáceres, C. H.,Wang, Q. G. 1996. Dendrite cell size and ductility of Al-Si-Mg casting alloys: Spear and Gardner revisited. *International Journal of Cast Metals Research* 9, pp. 157-162.

Cavazos, J. L., Colás, R. 2003. Quench sensitivity of a heat treatable aluminum alloy. *Materials Science and Engineering: A* 363, pp. 171-178.

Charmeux, J-F., Minev, R., Dimov, S. 2005, a. Capability Study of the Fcubic Direct Shell Process for Casting Micro-components. *Proceedings of the 1st International Conference on Multi-Materials Micro Manufacture, Karslruhe, Germany.* pp. 227-230.

Charmeux, J-F., Minev, R., Dimov, S. 2006. A Comparative Study of Three Technologies for Producing Castings with Micro/Meso-scale Features. *Proceedings of the 2nd International Conference on Multi-Materials Micro Manufacture, Grenoble, France.* pp. 327-330.

Charmeux, J-F., Minev, R., Dimov, S., Brousseau, E., Minev, E., Harrysson, U. 2007. Benchmarking of Three Processes for Producing Castings Incorporating Micro/Meso-scale Features with High Aspect Ratio. *Journal Proceedings of the Institution of Mechanical Engineers, Part B: Journal of Engineering Manufacture* 221, pp. 577-589.

Charmeux, J-F., Minev, R., Dimov, S., Minev, E., Su, S., Harrysson, U. 2005, b. Capability Study of the Vacuum Investment Casting for Rapid Prototyping and Micro-Manufacturing. *Proceedings, of the AMTECH Conference, Rousse University*, pp. 138-143.

Charmeux, J-F., Minev, R., Dimov, S., Minev, E., Su, S., Harrysson, U. 2005, c. Capability Study of the Vacuum Investment Casting for Rapid Prototyping and Micro-Manufacturing. *Journal of Materials Processing Technology* pp. 138-143. (in press)

Cheah, C. M., Chua, C. K., Lee, C. W., Feng, C., Totong, K. 2005. Rapid prototyping and tooling techniques: a review of applications for rapid investment casting *The International Journal of Advanced Manufacturing Technology* Volume 25(Numbers 3-4), pp. 308-320.

Childs, T. H. C., Juster, N. P. 1994. Linear accuracies from layer manufacturing. *Annals of the CIRP* 43(1), pp. 163-167.

Choi, D.-S., Lee, S. H., Shin, B. S., Whang, K. H., Song, Y. A., Park, S. H., Jee, H. S. 2001. Development of a direct metal freeform fabrication technique using CO2 laser welding and milling technology. *Journal of Materials Processing Technology* 113(1-3), pp. 273-279.

Chua, C. K., Feng, C., Lee, C. W., Ang, G. Q. 2005. Rapid investment casting: direct and indirect approaches via model maker II *The International Journal of Advanced Manufacturing Technology* Volume 25 (Numbers 1-2), pp. 26-32.

Chua, C. K., Leong, K. F., Lim, C. S. 2003. *Rapid prototyping : principles and applications*. 2nd ed. River Edge, NJ: World Scientific. ISBN: 9812381201.

Corcione, C. E.,Montagna, F.,Greco, A.,Licciulli, A.,Maffezzoli, A. 2006. Free form fabrication of silica moulds for aluminium casting by stereolithography *Rapid Prototyping Journal* 12(4), pp. 184-188.

Dash, M., Makhlouf, M. 2001. Effect of key alloying elements on the feeding characteristics of aluminum-silicon casting alloys. *Journal of Light Metals* 1(4), pp. 251-265.

Dickens, P. M., Stangroom, R., Greul, M., Holmer, B., Hon, K. K. B., Hovtun, R., Neumann, R., Noeken, S., Wimpenny, D. 1995. Conversion of RP models to investment castings. *Rapid Prototyping Journal* 1, pp. 4-11.

Dimitrov, D., Wijck, W.V., Schreve, K., Beer, N.D. 2006. Investigating the achievable accuracy of three dimensional printing. *Rapid Prototyping Journal* 12, pp. 42-52.

Dimov, S.S., Bramley, A.N., Eberhardt, W., Engel, U., Fillon, B., Johander P., Jung, E., Kirby, P.B., Matthews, C.W., Mattsson, L., Richter, M., Ritzhaupt-Kleissl, H-J., Schoth, A., Velten, T., Wenzel, C. 2007. 4M Network of excellence, Progress Report 2004-2006. *Proceedings of the 3rd International Conference on Multi-Materials Micro Manufacture, Borovets, Bulgaria*. pp. xvii-xxxi.

Diwan, R., Talic, Y., Omar, N., Sadig, W. 1997. Pattern waxes and inaccuracies in fixed and removable partial denture castings. *The Journal of Prosthetic Dentistry* 77(5), pp. 553-555.

Doreau, F., Chaput, C., Chartier, T. 2000. Stereolithography for Manufacturing Ceramic Parts. *Advanced Engineering Materials* 2(8), pp. 493 - 496.

Dotchev, K. D., Dimov, S. S., Pham, D. T., Ivanov, A. I. 2007. Accuracy issues in rapid manufacturing CastForm™ patterns *Journal Proceedings of the Institution of Mechanical Engineers, Part B: Journal of Engineering Manufacture* 221(1), pp. 53-67

Earnshaw, R., Morey, E. F. 1992. The fit of gold-alloy full-crown castings made with ceramic casting ring liners. *Journal of Dental Research* 71, pp. 1865-1870.

Ehmann, K.F., A synopsis of U.S. micro-manufacturing research and development activities and trends. 2007. *Proceedings of the 3rd International Conference on Multi-Materials Micro Manufacture, Borovets, Bulgaria*. pp 7-13.

Ehrfeld, W., Ehrfeld, U. 2001. Progress and profit through micro technologies: Commercial applications of MEMS/MOEMS. *Proceedings of SPIE. Micromachining and Microfabrication Process Technology VII* 4557. Ehrfeld Mikrotechnik, Germany. pp. 1-10

Fabian, T., Holman, F., Kang, S., Liu, H-C., Matsunaga, M., Prinz, F. B., Tsuru, H. 2004. Miniature gas turbine engine with unitary rotor shaft for power generation. United States Patent

6866478.

Flemings, M. C. 1974. *Solidification processing*. New York ; London: McGraw-Hill.

Flemings, M. C., Kattamis, T. Z., Bardes, B. P. 1991. Dendrite arm spacing in Aluminum Alloys. *Transactions of American Foundrymen Society* 99, pp. 501-506.

Gandarias, E. 2007. *MICROM: a revolutionary monitoring system to detect tool breakage & collision, enhance machine cycles and introduce a new probing concept in micromilling*. PhD thesis, Mondragon Unibertsitatea.

Gentle, J. E. 1998. *Random number generation and Monte Carlo methods*. New York: Springer. ISBN: 0387985220.

Ghany, K. A., Moustafa, S. F. 2006. Comparison between the products of four RPM systems for metals. *Rapid Prototyping Journal* 12, pp. 86-94.

Groover, M. P. 2005. *Fundamentals of Modern Manufacturing: Materials, Processes, and Systems*. USA, John Wiley & Sons. ISBN: 0471744859.

Hafiz, M. F., Kobayashi, T. 1994. A Study on the Microstructure-Fracture Behavior Relations in Al-Si Casting Alloys. *Scripta Metallurgica and Materialia* 30, pp. 475-480.

Hague, R.J., Dickens, P.M. 2001. Improvements in Investment Casting with Stereolithography Patterns. *Proceedings of the Institution of Mechanical Engineers, Part B: Journal of Engineering Manufacture,* 215(1), pp. 1-11, ISSN 09544054.

Hall, E. O. 1970. *Yield point phenomena in metals and alloys*. London: Macmillan.

Hanumaiah, N., Ravi, B. 2007. Rapid tooling form accuracy estimation using region elimination adaptive search based sampling technique *Rapid Prototyping Journal* 13(3), pp. 182-190.

Heiberg, G., Arnberg, L. 2001. Investigation of the microstructure of the Al-Si eutectic in binary aluminium-7 wt% silicon alloys by electron backscatter diffraction (EBSD). *Journal of Light Metals* 1(1), pp. 43-49.

Hesselbach, J., Raatz, A., Wreg, J., Herrman, H., Illenseer, S., Weule, H., Fleischer, J., Buchholz, C.. 2004. International State of the Art of Micro Production Technology. *Production Engineering* 11(1), pp. 29-36.

Hilton, P. D., Jacobs, P. F. 2000. *Rapid tooling: technologies and industrial applications*. Marcel Dekker Ltd. ISBN: 0824787889.

Ho, C. R., Cantor, B. 1995. Heterogeneous nucleation of Si solidification in Al-Si and Al-Si-P alloys. *Acta Metallurgica Et Materialia A*. 43, pp. 3231-3246.

Hopkinson, N., Dickens, P. 2001. Rapid prototyping for direct manufacture. *Rapid Prototyping Journal* 7, pp. 197-202.

Hopkinson, N., Dickens, P. 2003. Analysis of rapid manufacturing-using layer manufacturing processes for production. *Proceedings of the I MECH E Part C Journal of Mechanical Engineering Science* 217, pp. 31-39.

Imgrund, P., Rota, A., Petzoldt, F., Simchi, A. 2007. Manufacturing of multi-functional micro parts by two-component metal injection moulding *International Journal of Advanced Manufacturing Technology* 33(1-2), pp. 176-186.

Ippolito, R., Luliano, L., Gatto, A. 1995. Benchmarking of rapid prototyping techniques in terms of dimentional accuracy and surface finish. *Annals of the CIRP* 44(1), pp. 157-160.

Jacobs, P. 1996. Stereolithography and Other RP&M Techniques. *ASME Press, New York.* ISBN: 0872634671.

Jakka, R., Wilson, C.G. Next alchemy: nanoparticle exothermic alloying chemistry for producing tall on-chip cast metal microstructures. *Micro Electro Mechanical Systems, 2005. MEMS 2005.* 18th IEEE International Conference. pp. 528 – 531. DOI:10.1109/MEMSYS.2005.1453983

Jie, W., Chen, Z., Reif, W., Müller, K. 2003. Superheat of Al-7Si-0.55Mg Melt and its Influences on the Solidification Structures and the Mechanical properties. *Metallurgical and Materials Transactions A* 34, pp. 799-806.

Karapatis, N. P., Van Griethuysen, J-P. S., Glardon, R. 1998. Direct rapid tooling: a review of current research *Rapid Prototyping Journal* 4(2), pp. 77-89.

Kaufman, J. G., Rooy, E. L. 2004. *Aluminum Alloy Castings: Properties, Processes, and Applications.* ASM International. ISBN: 0871708035.

Khaing, M. W., Fuh, J. Y. H., Lu, L. 2001. Direct metal laser sintering for rapid tooling: processing and characterisation of EOS parts. *Journal of Materials Processing Technology* 113(1-3), pp. 269-272.

Klocke, F., Celiker, T., Song, Y. A. 1995. Rapid metal tooling. *Rapid Prototyping Journal* 1, pp. 32-42.

Kochan, D., Kai, C. C., Zhaohui, D. 1999. Rapid prototyping issues in the 21st century. *Computers in Industry* 39(1), pp. 3-10.

Kruth, J. P. 1991. Material ingress manufacturing by rapid prototyping technologies. *Annals of the CIRP* 40(2), pp. 603-614.

Kunieda, M.,Lauwers, B.,Schumacher, B. M.,Rajurkar, K. P. 2005. Advancing EDM through

Fundamental Insight into the Process. *Annals of the CIRP* 54(2), pp. 599-622.

Lee, C. W., Chua, C. K., Cheah, C. M., Tan, L. H., Feng, C. 2004. Rapid investment casting: direct and indirect approaches via fused deposition modelling *The International Journal of Advanced Manufacturing Technology* Volume 23(Numbers 1-2), pp. 93-101.

Lewis, G. K.,Schlienger, E. 2000. Practical considerations and capabilities for laser assisted direct metal deposition. *Materials & Design* 21(4), pp. 417-423.

Liu, Q., Leu, M. C., Richards, V. L., Schmitt, S. M. 2004. Dimensional accuracy and surface roughness of rapid freeze prototyping ice patterns and investment casting metal parts. *The International Journal of Advanced Manufacturing Technology* Volume 24(Numbers 7-8), pp. 485-495.

Liu, Q.,Sui, G.,Leu, M. C. 2002 a. Experimental study on the ice pattern fabrication for the investment casting by rapid freeze prototyping (RFP). *Computers in Industry* 48(3), pp. 181-197.

Liu, Z. Y., Loh, N. H., Tor, S. B., Khor, K. A., Murakoshi, Y., Maeda, R., Shimizu, T. 2002 b. Micro-powder injection molding. *Journal of Materials Processing Technology* 127(2), pp. 165-168.

Low, D., Mori, T. 1999. Titanium full crown casting: thermal expansion of investments and crown accuracy. *Dental Materials* 15(3), pp. 185-190.

Makhlouf, M. M., Guthy, H. V. 2001. The aluminum-silicon eutectic reaction: mechanisms and crystallography. *Journal of Light Metals* 1(4), pp. 199-218.

Markley, M. R. 1953. Compensation by thermal expansion. *The Journal of Prosthetic Dentistry* 3(3), pp. 419-422.

Masuzawa, T. 2000. State of the Art of Micromachining. *Annals of the CIRP* 49(2), pp. 473-488.

Mendoza, R., Alkemper, J., Voorhees, P. W. 2003. The morphological Evolution of Dendritic Microstructures during Coarsening. *Metallurgical and Materials Transactions A* 34A, pp. 481-489.

Minev, R.M., 2003. Rapid Prototyping with Vacuum Investment Casting, 'Development in Rapid Casting * Case Studies'. *Professional Engineering Publishing Ltd. (IMechE)*, pp 92-104.

Montgomery, D. C. 2005. *Introduction to statistical quality control.* 5th ed. Hoboken, N.J.: John Wiley. ISBN: 0471661228.

Montgomery, D. C., Runger, G. C. 1994. *Applied statistics and probability for engineers*. New York: Wiley. ISBN: 0471540412.

Morey, E. F., Earnshaw, R. 1995. The effect of potential investment expansion and hot strength

on the fit of full-crown castings made with a gypsum-bonded investment. *Dental Materials* 11(5-6), pp. 311-316.

Mott, B. W. 1956. *Micro-indentation hardness testing*. Butterworth's Scientific Publications. London.

Mounier, E. 2007. Micronews. *The Yole Développement magazine.* MEMS, Bio & Microfluidic Chips and Optics, 56. pp 6-8.

Mueller, T. 2007. Additive Fabrication Creates New Markets for Invetsment Casting. www.moldmakingtechnology.com.

Okhuysen, V., Padmanaban, K., Voigt, R. C. 1998. Tooling Allowances Practices in the Investment Casting Industry. *Investment Casting Institute: 46th Annual Technical Meeting, Orlando, Florida.* pp.1-17.

Osorio, W. R., Garcia, A. 2002. Modeling dendritic structure and mechanical properties of Zn-Al alloys as a function of solidification conditions. *Materials Science and Engineering A* 325(1-2), pp. 103-111.

Osorio, W. R., Goulart, P. R., Santos, G. A., Neto, C. M., Garcia, A. 2006. Effect of Dendritic Arm Spacing on Mechanical Properties and Corrosion Resistance of Al 9 Wt Pct Si and Zn 27 Wt Pct Al Alloys. *Metallurgical and Materials Transactions A* 37, pp. 2525-2538.

Oswalt, K. J., Misra, M. S. 1981. Dendrite arm spacing (DAS): a nondestructive test to evaluate tensile properties of premium quality aluminum alloy (Al–Si–Mg) castings. *AFS Transactions* 88, pp. 845-861.

Petch, N. J. 1953. The Cleavage Strength of Polycrystals. *Journal of the Iron and Steel institute* 174, pp. 25-28.

Peters, F.E., Velaga, R., Voigt, R.C., Assessing Dimensional Repeatability of Metalcasting Processes. *AFS Transactions*, 1996 a, pp. 181-190.

Peters, F.E., Voigt, R.C. How to determine Measurement Variability in the Pattern Shop. *Modern Casting*, 1996 b, pp. 58-60

Pfleging, W., Hanemann, T., Torge, M., Bernauer, W. 2003. Rapid fabrication and replication of metal, ceramic and plastic mould inserts for application in microsystem technologies. *Proceedings of the I MECH E Part C Journal of Mechanical Engineering Science* 217, pp. 53-63.

Pham, D. T., Dimov, S. S. 2001. Rapid manufacturing: the technologies and applications of rapid prototyping and rapid tooling. London; New York: Springer. ISBN: 185233360X.

Pham, D. T., Dimov, S. S. 2003. Rapid prototyping and rapid tooling-the key enablers for rapid

manufacturing. *Proceedings of the I MECH E Part C Journal of Mechanical Engineering Science* 217, pp. 1-23.

Pham, D. T., Gault, R. S. 1998. A comparison of rapid prototyping technologies. *International Journal of Machine Tools and Manufacture* 38(10-11), pp. 1257-1287.

Piotter, V., Guber, A., Heckele, M., Gerlach, A. 2004. Micro Moulding of Medical Device Components. *Business Briefing: Medical device manufacturing & technology*, pp. 1-7. www.touchbriefings.com

Piotter, V., Hanemann, T., Ruprecht, R., Haubelt, J. 1997. Injection molding and related techniques for fabrication of microstructures. *Microsystem Technologies* 3 (3), pp. 129-133.

Piwonka, T. S., Wiest, J. M. 1998. Factors Affecting Investment Casting Pattern Die Dimensions. *Incast* 11(6), pp. 8-13.

Rahmati, S., Akbari, J., Barati, E. 2007. Dimensional accuracy analysis of wax patterns created by RTV silicone rubber molding using the Taguchi approach *Rapid Prototyping Journal* 13(2), pp. 115-122.

Rajurkar, K. P., Levy, G., Malshe, A., Sundaram, M. M., McGeough, J., Hu, X., Resnick, R., DeSilva, A. 2006. Micro and Nano Machining by Electro-Physical and Chemical Processes. *CIRP Annals - Manufacturing Technology* 55(2), pp. 643-666.

Rath, S., Baumeister , G., Hausselt , J. 2006. Investments for casting micro parts with base alloys. *Microsystem Technologies* 12(3), pp. 258-266.

Ravi, M., Pillai, U. T. S., Pai, B. C., Damodaran, A. D., Dwarakadasa, E. S. 1998. Mechanical properties of cast Al-7Si-0.3Mg (LM 25/356) alloy. *International Journal of Cast Metals Research* 11, pp. 113-125.

Rosenthal, H. H. 1979. Shrink Allowance for Pattern Dies in Investment Casting. *Proceedings of the 27th Annual Meeting of the Investment Casting Institute.* Paper no. 2, pp. 1-11.

Ruprecht, R., Benzler, T., Hanemann, T., Müller, K., Konys, J., Piotter, V., Schanz, G., Schmidt, L., Thies, A., Wöllmer, H., Haußelt, J.1997. Various replication techniques for manufacturing three-dimensionnal metal microstructures. *Microsystem Technologies* 4, pp. 28-31.

Sabau, A. S. 2006. Alloy Shrinkage Factors for the Investment Casting Process. *Metallurgical and Materials Transactions B* 37, pp. 131-140.

Sabau, A. S., Viswanathan, S. 2002. Prediction of Wax Pattern Dimensions in Investment Casting. *AFS Transactions* 103(2), pp. 1-14.

Sabau, A. S., Viswanathan, S. 2003. Material properties for predicting wax pattern dimensions in investment casting. *Materials Science and Engineering A* 362, pp. 125-134.

Sachs, E., Cima, M., Cornie, J. 1991. Three Dimensioanl Printing: Ceramic Shells and Cores for Casting and Other Applications. *Proceedings from the 2nd International Conference on Rapid Prototyping*, Dayton, OH. pp. 39-44.

Santos, E. C.,Shiomi, M.,Osakada, K.,Laoui, T. 2006. Rapid manufacturing of metal components by laser forming. *International Journal of Machine Tools and Manufacture* 46(12-13), pp. 1459-1468.

Sarkis, B. E., Kennerknecht, S. C. G. 1994. Rapid Prototyping Casting (RPC): The fundamentals of producing functional metal parts from rapid prototype models using investment casting. *Proceedings of the 5th International conference on Rapid Prototyping, Dayton, OH.* pp. 291-300.

Spear, R. E., Gardner, G.R. 1963. Dendrite Cell Size. *Transactions of American Foundrymen Society* 71, pp. 209-215.

Srinivasan, A., Pillai, U. T. S., Pai, B. C. 2006. Effect of pouring temperature on the microstructure and the mechanical properties of low pressure sand cast LM25 (Al-7Si-0.3Mg) alloy. *International Journal of Microstructure and Materials Properties* 1(2), pp. 139-148.

Steen, H. A. H., Hellawell, A. 1972. Structure and Properties of Aluminium-Silicon Eutectic alloys. *Acta Metallurgica* 20, pp. 363-370.

Tang, Y., Fuh, J. Y. H., Loh, H. T., Wong, Y. S.,Lu, L. 2003. Direct laser sintering of a silica sand. *Materials & Design* 24(8), pp. 623-629.

Taylor, P.R. 1983. An Illustrated history of lost wax casting. *Proceedings of the 17th Annual BICTA Conference, British Investment Casting Association.*

Thian, S.C.H., Tang, Y., Fuh, J.Y.H., Wong, Y.S., Lu, L., Loh, H.T. 2006. Micro-rapid-prototyping via multi-layered photo-lithography. *The International Journal of Advanced Manufacturing Technology* 29 (9-10), pp.1026-1032.

Twarog, D.L. 1993. *Handbook on the investment casting process. American Foundrymen's Society Inc.* ISBN 0874331560.

Vázquez-López, C., Calderón, A., Rodriguez, M. E., Velasco, E., Cano, S., Colás, R., Valtierra, S. 2000. Influence of dendrite arm spacing on the thermal conductivity of an aluminum-silicon casting alloy *Journal of Materials Research* 15(1), pp. 85-91.

Vollertsen, F., Hu, Z., Niehoff, H. S., Theiler, C. 2004. State of the art in micro forming and investigations into micro deep drawing. *Journal of Materials Processing Technology* 151(1-3), pp. 70-79.

Wang, Q. G., Apelian, D., Lados, D. A. 2001. Fatigue behavior of A356/357 aluminum cast

alloys. Part II - Effect of microstructural constituents. *Journal of Light Metals* 1(1), pp. 85-97.

Wang, Q. G., Cáceres, C. H. 1998. The fracture mode in Al-Si-Mg casting alloys. *Materials Science and Engineering: A* 241, pp. 72-82.

Wang, Q. G., Cáceres, C. H., Griffiths, J. R. 1998. Cracking of Fe-Rich Intermetallic and Eutectic Si Particles in an Al-7Si-0.7Mg Casting Alloy. *AFS Transactions* 106, pp. 131-136.

Wechsung, R., Unal, N., Eloy, J., Wicht, H. 1998. "Market Analysis For Microsystems" an interim report from the NEXUS TASK FORCE. pp. 275-281.

Wicht, H., Bouchaud, J. 2005. NEXUS Market Analysis for MEMS and Microsystems III 2005-2009. From mstnews "International newsletter on micro-nano integration". No 5/05. October 2005. pp 31-34.

William, D. C. 1997. *Materials science and engineering: an introduction*. 4th ed. New York ; Chichester: Wiley. ISBN: 0471134597.

Xu, G., Zhao, W., Tang, Y., Lu, B. 2006. Novel stereolithography system for small size objects. *Rapid Prototyping Journal* 12, pp. 12-17.

Yao, W. L., Leu, M. C. 1991. Analysis of shell cracking in investment casting with laser stereolithography patterns. *Rapid Prototyping Journal* 5, pp. 12-20.

Yodice, D. B. 1991. Investment casting process.United States Patent. Patent number: 5.072.770.

Zhang, S. H., Wang, Z. R., Wang, Z. T., Xu, Y., Chen, K. B. 2004. Some new features in the development of metal forming technology. *Journal of Materials Processing Technology* 151(1-3), pp. 39-47.

Zhang, S. J., Raja, V. H., Fernandes, K. J., Ryall, C., Wimpenny, D. 2003. Rapid prototyping models and their quality evaluation using reverse engineering. *Proceedings of the I MECH E Part C Journal of Mechanical Engineering Science* 217 part C, pp. 81-96.

Zhang, Z., Tamaki, Y., Hotta, Y., Miyazaki, T. 2006. Novel method for titanium crown casting using a combination of wax patterns fabricated by a CAD/CAM system and a non-expanded investment. *Dental Materials* 22(7), pp. 681-687.